Dipartimento di Ingegneria Meccanica e Industriale

UNIVERSITÀ
DEGLI STUDI
DI BRESCIA

Dottorato di ricerca in Ingegneria Meccanica e Industriale

Tema di ricerca: analisi di dati da sensori e rivelatori di particelle

Settore scientifico disciplinare: FIS/01

Ciclo XXXVI

Measurement of Earth's gravitational acceleration on anti-hydrogen with the ALPHA experiment at CERN

Supervisore:
Prof. Germano Bonomi

Dottoranda:
Marta Urioni

Co-supervisore:
Dott. Simone Stracka – INFN di Pisa

Contents

Sinossi **5**

Abstract **6**

Introduction **7**

1 Matter-antimatter asymmetry, CPT symmetry and weak equivalence principle **9**
1.1 Matter-antimatter asymmetry problem 10
1.1.1 CPT symmetry and its violation 12
1.2 Weak equivalence principle and gravity 15
1.2.1 History of the gravitational acceleration on antimatter 15
1.2.2 Anti-hydrogen and gravity 18

2 The ALPHA experiment **20**
2.1 The AD and ELENA 20
2.1.1 The AD 20
2.1.2 ELENA 21
2.2 The ALPHA experiment 23
2.3 The catching trap 24
2.4 The positron accumulator 27
2.5 The Beamline 28
2.6 The ALPHA2 apparatus 29
2.6.1 Overall setup 29
2.6.2 The ALPHA2 atom trap 29
2.6.3 The detector 29
2.7 The ALPHAg apparatus 31
2.7.1 Motivation 31
2.7.2 Overall setup 31
2.7.3 The ALPHAg measurement strategy 32
2.7.4 Electrodes 33
2.7.5 Magnets 33
2.7.6 The detectors 39

3 Anti-hydrogen formation and gravity measurement procedure 45
3.1 Penning traps and plasma manipulations 45
3.1.1 Plasma Cooling and Manipulation 48
3.2 Trapping of anti-hydrogen 54
3.3 Anti-hydrogen production procedure 56
3.3.1 Antiproton preparation 56
3.3.2 Positron preparation 58
3.3.3 Plasma mixing 58
3.4 ALPHAg 2022 gravity experiment 59
3.4.1 The measurement procedure 60
3.5 Simulation of the anti-hydrogen release 62

4 Data analysis for the measurement of gravitational acceleration on anti-hydrogen 65
4.1 Data sample 67
4.2 Tracks reconstruction and selection 69
4.2.1 Background rejection 69
4.2.2 Vertex position (z) selection 71
4.2.3 Vertex time (t) selection studies 71
4.3 Model definition 76
4.4 Calibration of the model 77
4.4.1 Signal and background models 77
4.4.2 Extraction of the efficiency asymmetry from long- octupole data 79
4.5 Regression of the acceleration parameter 80

5 Systematic uncertainties on the anti-hydrogen gravitational acceleration 85
5.1 Systematic uncertainty due to the analysis procedure 85
5.1.1 Calibration and background samples size 85
5.1.2 Calibration sample purity assumption 86
5.1.3 Uncertainty on the detection efficiency asymmetry . . 86
5.1.4 Calibration/physics sample discrepancies 86
5.1.5 Simulation sample size 86
5.1.6 Effect of the choice of the range of magnetic biases . . 87
5.1.7 Simulation interpolation 87
5.2 Systematic uncertainties due to the $\bar{H}$ simulation 88
5.2.1 Energy distribution of the anti-hydrogen (S-curve slope) 88
5.2.2 On-axis magnetic field 89
5.2.3 Off-axis magnetic field 90

6 Results and cross checks **93**
6.1 Significance 93
6.2 Cross-Checks 95
6.2.1 Validation of the fit to the *calibration samples* 95
6.2.2 Validation of the fit to the *physics samples* 95
6.2.3 GPR fitting tests 97

7 Conclusions **100**

A Derivation of gravity measurement model parametrization **104**

Bibliography **108**

Acknowledgements **123**

Nomenclature

$\bar{H}$	Anti-hydrogen atom(s)
$\bar{p}$	Antiproton(s)
e^+	Positron(s)
AD	Antiproton Decelerator
ADC	Analog to digital converter
ALPHA	Anti-hydrogen Laser PHysics Apparatus
ALPHA2	Apparatus for measuring the laser-induced transitions between principal energy levels of the anti-hydrogen atom
ALPHAg	Apparatus for measuring the Earth's gravitational acceleration on anti-hydrogen
BV	Barrel Veto: ALPHAg scintillator bars detector for background rejection
CT	ALPHA Catching Trap: capture, cool and accumulate the antiprotons from ELENA
ECR	Electron Cyclotron Resonance method for measuring the magnetic fields inside a magnetic trap
ELENA	Extra Low ENergy Antiproton decelerator
GPR	Gaussian Process Regression
LOc	Long Octupole coil
MAGB	Mirror A and G coils
PDF	Probability Density Function
rTPC	radial Time Projection Chamber: ALPHAg's tracking detector
TDC	Time-to-digital converter
WEP	Weak Equivalence Principle

Sinossi

Sebbene l'interazione gravitazionale tra materia e antimateria sia stata oggetto di speculazione teorica sin dalla scoperta di quest'ultima nel 1928, solo recentemente, per la prima volta, l'esperimento ALPHA al CERN (*Anti-hydrogen Laser physics Apparatus*) è stato in grado di osservare gli effetti della gravità sugli atomi di antimateria, in particolare sull'anti-idrogeno. Questa misura è un test del principio di equivalenza debole (WEP), un principio fondamentale della teoria della relatività generale di Einstein, che afferma che tutte le masse reagiscono in modo identico alla gravità, indipendentemente dalla loro struttura interna.
Per misurare l'accelerazione gravitazionale sull'anti-idrogeno, gli anti-atomi sono stati confinati magneticamente nell'apparato sperimentale di ALPHA e rilasciati sotto un effetto combinato di forze gravitazionali e magnetiche. L'analisi dei dati acquisiti si basa sulla costruzione di una *likelihood* delle posizioni dei vertici di annichilazione prodotti quando i campi magnetici per il confinamento vengono ridotti e gli atomi di anti-idrogeno escono dalla trappola. Il parametro rilevante di questa *likelihood* è l'asimmetria tra il numero di anti-atomi rilasciati verso l'alto e il numero di anti-atomi rilasciati verso il basso rispetto al centro della trappola elettromagnetica. Successivamente il parametro dell'accelerazione gravitazionale è ottenuto da una regressione sui dati eseguita utilizzando un modello ricavato dalla simulazione numerica del moto degli anti-atomi nell'esperimento. Questo lavoro comprende la stima delle incertezze statistiche e il trattamento delle incertezze sistematiche.
I risultati dell'analisi rivelano che gli atomi di anti-idrogeno si comportano in modo compatibile con l'attrazione gravitazionale tra anti-idrogeno e Terra. Questo esperimento apre la strada a ulteriori ricerche sull'accelerazione gravitazionale terrestre su anti-atomi per effettuare test più precisi del principio di equivalenza debole.

Abstract

Although the gravitational interaction between matter and antimatter has been the subject of theoretical speculation since the discovery of the latter in 1928, only recently, for the first time, the ALPHA experiment at CERN (*Anti-hydrogen Laser PHysics Apparatus*) was able to observe the effects of gravity on antimatter atoms, namely on anti-hydrogen. This measurement is a test of the weak equivalence principle (WEP), a fundamental principle of Einstein's general theory of relativity, stating that all masses react identically to gravity, independent of their internal structure.
In order to measure the gravitational acceleration on anti-hydrogen, anti-hydrogen atoms were magnetically confined in the ALPHA apparatus and released under a combined effect of gravitational and magnetic forces. The analysis of the acquired data is based on the construction of a likelihood of the annihilation vertex positions produced when the confining magnetic fields are lowered and the anti-hydrogen atoms are released. The relevant parameter of this likelihood is the asymmetry between the number of anti-atoms escaping upwards and the number of anti-atoms escaping downwards with respect to the center of the electromagnetic trap. The gravitational acceleration parameter is obtained from a regression on the data using a model obtained from a simulation of the anti-hydrogen motion in the experiment. This work includes the estimation of the statistical uncertainties and the treatment of the systematic uncertainty sources.
The analysis results reveal that anti-hydrogen atoms behave in a way that is consistent with gravitational attraction between anti-hydrogen and the Earth. This experiment sets the path for further research on the gravitational acceleration between anti-atoms and the Earth for WEP testing.

Introduction

The universe is almost entirely composed of matter, while we see only rare traces of antimatter. Antimatter's properties have intrigued physicists for decades since its discovery in 1928. Among these properties, the study of the anti-hydrogen energy levels and its response to gravity could play an important role in explaining the universe's scarcity of antimatter.

The ALPHA experiment at CERN (*Anti-hydrogen Laser PHysics Apparatus*) creates and traps anti-hydrogen to study it [1]. Anti-hydrogen is the antimatter counterpart of hydrogen in regular matter and is made up of an antiproton with a positron orbiting around it. ALPHA has made several measurements of the properties of anti-hydrogen: different measurements about spectroscopy of anti-hydrogen energy levels for CPT (*Charge conjugation, Parity, Time reversal*) symmetry testing [2, 3, 4] and the limit on the charge of anti-hydrogen [5].

In 2018 the ALPHAg apparatus was constructed for the measurement of the Earth's gravitational acceleration on anti-hydrogen, the measurement on which this thesis is focused. In particular the main topic of this thesis is the analysis performed on the data collected during the data acquisition of 2022; details of this measurement and of its results are published in [6]. By investigating the gravitational behaviour of anti-hydrogen, the ALPHA experiment performs the first experimental test of the weak equivalence principle (WEP) on a neutral anti-atom [6].

This thesis is organised into five different chapters. In Chapter 1 the matter-antimatter asymmetry problem is presented and the theoretical background of the principles tested by the ALPHA experiment is exposed. Chapter 1, in particular, focuses on the CPT symmetry and its violation in the context of antimatter, moreover the WEP and the concept of anti-gravity are exposed. In Chapter 2 the Antiproton Decelerator (AD) and the ELENA ring (Extra Low ENergy Antiproton) used for decelerating the antiprotons produced by a proton beam-target interaction are described. Afterwards, Chapter 2 presents the ALPHA apparatus, focusing on the ALPHAg apparatus, the experimental setup used to measure the gravitational acceleration on anti-hydrogen. It describes the ALPHAg atom trap (a Penning-Malmberg trap

embedded in an Ioffe-Pritchard trap) and the physics behind anti-hydrogen confinement in magnetic traps.
Chapter 3 outlines the technologies and techniques employed in the manipulation of the charged plasmas used for anti-hydrogen synthesis and their physical working mechanisms. Furthermore, it provides a description of the measurement procedures followed during the 2022 data acquisition.
Chapter 4 is dedicated to the description of the analysis of the data collected during the 2022 data taking. The cuts applied to the data are described, together with the model used for constructing the likelihood of the data, the estimation of the detector efficiency, the regression on the data using a simulation-derived model for the estimation of the gravitational acceleration on anti-hydrogen and, finally, the treatment of statistical and systematic uncertainties.
The results of this work show that the anti-hydrogen atom's gravitational behaviour is consistent with the gravitational attraction between anti-hydrogen and the Earth. Moreover, the presence of repulsive gravity between anti-hydrogen and the Earth is ruled out.

Concerning my personal contribution inside the ALPHA collaboration for the measurement of the gravitational acceleration of anti-hydrogen in the Earth field, I've spent about 7 months during my PhD working in the ALPHA experimental area at CERN taking part in the shifts for the commissioning of the experimental apparatus and for the ALPHA data acquisition. Moreover, I focused on the data analysis for the estimation of the gravitational acceleration of anti-hydrogen. The Physics Analysis Group was composed of 6 people: 3 from Berkeley (Prof. Joel Fajans, Dr. Danielle Louise Hodgkinson, Prof. Jonathan Wurtele) and 3 from Italy (Prof. Germano Bonomi, Dr. Simone Stracka and me). The two groups conducted the analysis independently. My contribution focused on the likelihood construction, the detector efficiency estimation, the data regression for estimating the gravitational acceleration on anti-hydrogen, and the treatment of statistical and systematic uncertainties. Some systematic uncertainties sources were estimated by other researchers, and their role will be specified in chapter 4.

Chapter 1

Matter-antimatter asymmetry, CPT symmetry and weak equivalence principle

One of the greatest mysteries of cosmology is the matter-antimatter asymmetry problem, which corresponds to the overabundance of matter with respect to antimatter in the universe. The universe was created in the "Big Bang" according to the the standard model of cosmology [7], and it is generally assumed that the Big Bang produced an equal amount of particles and antiparticles. However cosmological observations show that the universe is dominated by matter, implying the existence of an asymmetry between matter and antimatter in nature. Even if the observed matter asymmetry could be in principle explained by the three Sakharov conditions [8] (C and CP violation, Baryon-number violation, and interactions out of thermal equilibrium) the size of the CP violation contained in the Standard Model appears not sufficient to provide a convincing explanation. For this reason the ALPHA2 experiment aims to study the energy levels of anti-hydrogen in order to search for symmetry violations that suggest the reason of the matter-antimatter asymmetry in the universe.
Furthermore, in recent years, some authors have postulated alternative cosmological theories [9, 10] in which antimatter's gravitational acceleration differs from that of conventional matter. These models try to explain the dominance of matter over antimatter in our universe while also providing a new perspective on the cosmological issues raised by the supposed existence of dark matter [11] and dark energy [12, 13]. These models, however, are incompatible with the Weak Equivalence Principle (WEP), a fundamental principle of the theory of general relativity. The ALPHAg experiment aims to test the Weak Equivalence Principle (WEP) on anti-hydrogen.

1.1 Matter-antimatter asymmetry problem

The standard cosmological model [14] assumes that the universe was generated in the "Big Bang" and it is today made up of around 5% ordinary matter, 27% dark matter, and 68% dark energy [15]. Furthermore, it is widely assumed that the Big Bang produced an equal amount of particles and antiparticles. This leads to the matter-antimatter asymmetry problem, because the universe is now thought to be almost exclusively made up of matter rather than antimatter and at the moment there is no acceptable solution to this problem. For understanding the asymmetry problem, both knowledge of the physical nature of the Big Bang and a precise definition of matter within the Standard Model are needed. The Standard Model (SM) [16] assumes that the elementary matter particles are leptons and quarks (together with the vector bosons), implying that electrons, neutrons, and protons, which account for 5% of the universe's ordinary matter constitute almost all the matter present in the universe.
The big bang theory emerged in response to the theoretical prediction [17, 18] and observational evidence of cosmic expansion [19] and cosmic microwave background [20]. According to the big bang theory, the universe was hot in its early phases [21], and when the pair production and annihilation reactions were in thermal equilibrium, antimatter was present. When the particle energies in the cooling plasma fell too low for pair production, practically all particles and antiparticles were annihilated, with only a small amount of matter remaining, by definition. This is a necessary phenomenon as the universe nowadays appears to be almost entirely made up of hydrogen and helium atoms instead of anti-hydrogen and anti-helium atoms. Within the context of the Standard Model, the matter-antimatter asymmetry problem is commonly seen to be related to the baryon asymmetry problem, i.e. the imbalance of baryonic and antibaryonic matter in the observable universe.
The universe's baryon asymmetry can be defined as the difference in the number of baryons N_B and antibaryons $N_{\overline{B}}$ divided by their sum right before antiprotons vanished from the primordial plasma. Because the end products of annihilation processes are predominantly photons and there are no antibaryons in the universe today, the baryon to photon ratio η can be used to determine baryon asymmetry.

$$\eta = \left.\frac{N_B}{N_\gamma}\right|_{T=3K} = \left.\frac{N_B - N_{\overline{B}}}{N_\gamma}\right|_{T=3K} \sim \left.\frac{N_B - N_{\overline{B}}}{N_B + N_{\overline{B}}}\right|_{T\gtrsim 1GeV} \tag{1.1}$$

η is connected to the residual density of baryons Ω_B by the relation $\Omega_B \simeq \eta/(2.739 \times 10^{-8} h^2)$, where h parameterizes the Hubble rate $H_0 = 100h$ ($\mathrm{kms}^{-1}\mathrm{Mpc}^{-1}$) [22]. It can be calculated in two different ways: from the abundances of light elements in the intergalactic medium [23] and from the

power spectrum of temperature changes in the Cosmic Microwave Background [24]. Both provide consistent values around $\sim 10^{-10}$.
Thus, today's matter-antimatter asymmetry is massive, yet it was once negligible. The experimental evidence of small violations of P [25] and CP invariance [26] (and hence C invariance) revealed suggestions that this asymmetry may have been produced dynamically via baryogenesis from a matter-antimatter symmetric beginning state.
Within the context of the Standard Model, Sakharov proposed in 1967 [8] a set of three required conditions that a physical process must satisfy in order to produce baryons and antibaryons at distinct production rates:

- violation of the baryon number;
- both charge conjugation symmetry, C, and charge conjugation-parity symmetry, CP, must be violated;
- the process must not be in thermal equilibrium.

A violation of the baryon number is necessary to produce an excess of baryons over antibaryons, in the meanwhile a violation of C symmetry ensures the absence of processes that produce an equivalent excess of antibaryons over baryons. Similarly, a violation of CP symmetry is required such that equal numbers of left - handed baryons and right - handed antibaryons, as well as equal numbers of right-handed baryons and left - handed antibaryons, are not created. Finally, the process must not be in thermal equilibrium so that CPT symmetry does not assure compensation between processes increasing and reducing the baryon number [27].
The first Sakharov condition, violation of baryon number, would be met if antiprotons or protons disintegrated into lighter subatomic particles such as a neutral pion and an electron or positron, respectively. However, there is no experimental evidence that such "direct" violation of baryon number occur at the moment. Thus, researchers focused on indirect violations of the baryon number, which are concerned with Sakharov's second criterion: CP violation, which implies the possibility that some physical processes may distinguish between matter and antimatter. The electromagnetic and strong interactions are both symmetric under C and P, and so also under the product CP. This is not true for the weak interaction, which violates both C and P symmetries, this was established with the discovery in 1964 of the decay of the long-lived K^0 meson [26] to two charged pions. The violation of CP in weak interactions means that weak interactions may result in an indirect violation of baryon number, implying that matter creation is preferred over antimatter creation.
Charged current (CC) weak interactions that modify the charge and flavor of quarks cause CP violation in the Standard Model. Three up-like quarks with electric charge $Q = +2/3$ are known: up (u), charm (c), and top (t);

while three down-like quarks with electric charge $Q = -1/3$ are known: down (d), strange (s), and bottom (b). Each up-like quark is converted into a down-like quark via the charged current weak interactions, and vice versa. The Cabibbo-Kobayashi-Maskawa (CKM) [28, 29] matrix elements provide the transition amplitudes for the nine possible transition combinations.
Cabibbo in 1963 introduced some of the matrix elements of the CKM matrix prior to the quark model of Gell-Mann [30] and Zweig [31]. In 1973, Kobayashi and Maskawa [29] showed that the CC weak interactions may violate CP in the case of three quarks generations. However, the Kobayashi-Maskawa CP violation was found to be minor, owing to the small size of the relevant matrix elements.
As a result, any physical process that produces more matter than antimatter would be ineffectual. Although the matter-antimatter surplus is typically thought to have been only one part in a billion, the influence of the Kobayashi-Maskawa to the CP violation process is far smaller than even this very small amount by many orders of magnitude. Indeed, the baryon excess created by the Kobayashi-Maskawa CP violation process is believed to be barely enough to provide the baryons of just one galaxy in the universe, the universe instead contains billions of galaxies [32].
The third Sakharov criterion, departure from thermal equilibrium, is widely thought to occur within the Standard Model's electroweak sector during the electroweak phase transition [33, 34].
Finally, the SM does provide physical processes that satisfy all three of Sakharov's required conditions. However, the proposed physical processes do not appear to be able to explain the matter-antimatter asymmetry. The prevailing conclusion is that this requires some physical processes beyond the Standard Model.
Beyond-standard-model theories introduce Baryon number or Lepton number violation via the decay of heavy gauge bosons or Higgs fields in grand unified theories or the decay of Right-handed neutrinos. Both are theoretically motivated ideas, with sterile neutrinos with heavy Majorana masses acting as a natural' mechanism to generate the light neutrino masses. Modifications to the Standard Model can also make the electroweak phase transition first-order, leading to the electroweak baryogenesis mechanism. Within the standard cosmological model, there are numerous related Beyond Standard Model scenarios of baryogenesis or leptogenesis (e.g. [35, 36, 37]) that can give origin to the observed matter-antimatter asymmetry.

1.1.1 CPT symmetry and its violation

CPT invariance is the observed discrete spacetime symmetry at the level of known fundamental physics, where CPT denotes the coupled transformation of charge conjugation C, parity inversion P, and time reversal T. Lorentz and CPT symmetry are found to be closely linked, which has important

implications for experimental tests of spacetime symmetries. Approximately, C can be thought of as exchanging all particles with antiparticles in the system, P as reflecting all the three spatial coordinates ($\vec{r} \to -\vec{r}$) and T as reversing the time coordinate ($t \to -t$).
The exact CPT symmetry requirement was used in the formulation of the Sakharov conditions mentioned in the preceding section. Otherwise, it is feasible to create a matter-antimatter asymmetry in thermal equilibrium if the CPT is allowed to be violated [38]. In other words, the CPT violation can take the place of the third Sakharov criterion. Even allowing CPT violation, the first two Sakharov requirements (satisfying C and CP violations) must still be met for a Beyond-Standard-Model theory that includes Baryon or Lepton number violating interactions.
A hypothetical leptogenesis model can be studied within the Standard Model Extension (SME) [39, 40], which is an effective field theory that incorporates the Standard Model, General Relativity, and all symmetry-breaking spacetime operators. As a result, it is the most general theoretical framework compatible with the known fundamental physics while allowing for any potential CPT and WEP violations.
To give an idea of a possible leptogenesis model meeting the CPT violation requirement, one can consider (following the review [41]) the following term for the light neutrinos in the Standard SME that is minimally Lorentz and CPT violating, initially limited to one flavour for simplicity:

$$L = a_{\mu}^{(3)} \overline{\nu}_L \gamma^{\mu} \nu_L \tag{1.2}$$

this term (L) is C violating, CP odd, and CPT odd. The coupling $a_0^{(3)}$ operates as a chemical potential because an interaction of this type changes the energy-momentum dispersion relation differently for neutrinos and antineutrinos, and this modifies the associated particle distributions at non-zero temperature.
This effective chemical potential $\mu = a_0^{(3)}$ gives different equilibrium number densities for neutrinos and antineutrinos in the high temperature environment of the early Universe, resulting in a net lepton number density $\eta_l \sim \mu T_D^2$.
With the universe cooling, the rate of these interactions decreases until it falls below the rate of expansion, as defined by the Hubble parameter [42], at some decoupling temperature T_D. Thermal equilibrium is no longer maintained at this stage, and the lepton number density freezes at the value $\eta_l \sim \mu T_D^2$. Given that the photon density varies with temperature according to $\eta_\gamma \sim T^3$, the resulting lepton-to-photon ratio is then frozen at a value $\eta_l \equiv \eta_l/\eta_\gamma \sim a_0^{(3)}/T_D$. If T_D is greater than the electroweak scale, this lepton number asymmetry can be converted to a baryon number asymmetry via sphaleron interactions (interactions near the energy saddle points), resulting in a final baryon-to-photon ratio η that is diminished by a factor of around

10^2 with respect to η_l. Extending to the three neutrino flavours: $L = (a_\mu^{(3)})_{ij}\overline{\nu}_L^i\gamma^\mu\nu_L^j$.
The mechanism described above is essentially the same as the one of "spontaneous leptogenesis", where the role of the coupling a_μ is played by a time-dependent VEV (vacuum expectation value) of a scalar field.
At this stage, one can determine if this process is plausible in light of the experimental limits on the relevant minimal SME parameters. This assumes that these couplings are kept constant throughout the Universe's evolution. This is not trivial, because if they are treated as VEVs of some time-dependent fields, their values would change and may be way larger at the time of lepto(baryo)genesis than they are now. Constraints on the relevant neutrino coefficients of $(a_0^{(3)})_{ij} \lesssim 10^{-20}$ GeV are obtained from the SME data tables [43]. When T_D exceeds 100 GeV, the corresponding value of $\eta_l \sim a_0^{(3)}/T_D$ is many orders of magnitude too small. Under these assumptions, constraints on $(a_0^{(3)})_{ij}$ in the quark sector would also rule out the direct baryogenesis scenario.
However, in [44], where this type of CPT violating model was initially examined, the potential of higher-dimension operators in the SME effective Lagrangian to yield the observed value of the asymmetry was discussed. For example considering the leading-order electron coupling of this type, that contains extra derivatives in the operator ($L_a^{(5)} = -a_{\mu\rho\sigma}^{(5)}\overline{\psi}\gamma^\mu\partial^\rho\partial^\sigma\psi$), the same calculation would give a corresponding lepton asymmetry of the order $|a_{0\rho\sigma}^{(5)}|T_D$.
To extract a result from this operator, one can use a non-relativistic expansion, which leads to the coupling a_{200}^{NR}, which enters the transition frequency for the 1S-2S transition of Hydrogen and anti-Hydrogen, or an ultra-relativistic expansion [45], which leads to the relevant parameter $a^{UR(5)}$. The couplings a_{200}^{NR} and $a^{UR(5)}$ are related but not identical, and very different constraints for the electron are reported in the SME data files [44]. Measuring a non-vanishing a_{200}^{NR} coefficient in the well-known scenario of 1S-2S anti-hydrogen spectroscopy would provide a tremendous push to CPT violation-based models of leptogenesis and baryogenesis.
To recap, in contrast to CPT conserving theories, a baryon or lepton asymmetry can be formed in thermal equilibrium with CPT violation by a mechanism comparable to spontaneous baryo(lepto)genesis. However, these models still require novel BSM physics using yet unknown particles. The limits on the SME parameters appear to rule out models limited to the minimal SME. Non-minimal SME couplings, on the other hand, are less constrained in general, and the different dependence on decoupling temperature in models involving them offers the potential to achieve the required asymmetry, as long as the couplings are not too suppressed by the high-energy scale underlying the SME effective Lagrangian.

1.2 Weak equivalence principle and gravity

The weak equivalence principle (WEP) is the most widely accepted principle in modern physics. Its origins can be traced back to Galileo's discovery of the "universality of free fall" on Earth. Newton added a greater knowledge on WEP when he explained "universality of free fall" as a result of the equivalence of inertial mass m_I and gravitational mass m_G. Unlike many other principles, the WEP has grown in importance over time and is now the foundation of Einstein's General Theory of Relativity and current Cosmology.
Over the last century, the general theory of relativity has passed a number of stringent experimental tests [46]. Among its core tenets, still experimentally unchallenged, is the Einstein equivalence principle (EEP). The EEP, in its modern form [47], consists of three parts: the universality of free fall, also known as the weak equivalence principle (WEP), the local Lorentz invariance (LLI) and the local position invariance (LPI). The WEP implies that all objects fall at the same rate, regardless of their internal composition or structure. In other words, the WEP asserts that at the non-quantum level, the gravitational masses of particles and antiparticles are equal and it predicts the same behaviour for particles and antiparticles when subject to gravitational fields. This is because the local effects of motion in a curved space-time (gravitation) are indistinguishable from those of an accelerated observer in flat spacetime, without exception.
There are two different types of speculation on suspected violations of the WEP. The first (and older) set comprises of various theoretical scenarios for minimal WEP violation. The universality of gravitational attraction is not questioned (hence no room for antigravity), yet gravitational and inertial mass can be slightly different in some cases, the references on this topic can be found in [48]. The second group of hypotheses, which emerged in the last decade of the twentieth century, lead to the gravitational repulsion between matter and antimatter, i.e. antigravity, and implies the most significant violation of the WEP.

1.2.1 History of the gravitational acceleration on antimatter

The contemporary concept of "antigravity" arose from the two physics revolutions of the twentieth century that are quantum mechanics and general relativity. From the standpoint of particle physics, general relativity is a gravity theory in which the force is mediated by a tensor, a spin-two particle with a mass-energy charge [49]. As a result, the gravitational force is always attractive. Classical and quantum electromagnetism, on the other hand, require two charges, positive and negative. A vector (spin-one) field mediates the forces, producing an attractive force between opposite charges and a repulsive force between charges of the same sign. Many physicists from

the 1930s and 1940s asserted that charge-forces mediated by even-integer spin bosons are always attractive, whereas forces mediated by odd-integer spin bosons can be both attractive and repulsive, depending on whether the charges are of the opposite sign or of the same sign, but the fundamental reason of this was not understood. The first publication in which this statement was pointed out is [50].

The earliest indication of the existence of antimatter came from the solutions with negative energy of the Dirac equation. The positron was the first in a long series of antiparticles discovered later on.

Afterwards, the idea appeared that matter and antimatter could gravitationally repel each other due to a tensor gravitational interaction with the sign of Newton's constant reversed. This hypothetical phenomenon is called "antigravity" (or tensor-antigravity). Einstein included the possibility of a cosmological term when he first developed his general theory of relativity. This was due to the fact that he could not think of any other way for the seemingly static universe to be stable against gravitational collapse. However, the Hubble expansion of the universe was discovered later, which eliminated the requirement for the cosmological term. This gave rise to the Big-Bang theory of the universe, which states that the Hubble expansion is the product of a primordial explosion, now estimated to have occurred 20 billion years ago.

In this context, Bondi and Gold [51], as well as Hoyle [52], separately presented the Steady-State Theory of the Universe. This hypothesis proposed that as the universe expanded, matter was constantly created, so that the average density of the universe remained constant over long periods of time. According to this theory, the universe at vast distances had to appear to have the same age as in our local region, and the Hubble expansion law had to be of a precise form. Instead, later on, the universe was determined to be substantially different at big distances, with quasars existing, and the 3K black body radiation was discovered.

In the steady-state universe, only a minimal amount of matter was required to be generated. Even at the time, the estimate was one hydrogen atom per liter per 10^{12} years [51]. However, this implied a minor violation of energy conservation. As a result, the existence of "antigravity" was questioned, in particular Bondi questioned if there were valid negative-mass solutions in general relativity [53]. In a historical investigation, however, Gold collaborated with Morrison to discuss the interaction of gravity and antimatter. This research culminated in the Gravity Research Foundation's 1957 prize-winning essay. Morrison developed this idea in his Richtmyer Lecture in 1958 [54]. This paper included the first of three classic arguments against "antigravity".

The classic arguments against "antigravity" in particular do not exclude a difference in the gravitational acceleration of antimatter and matter towards the earth, just a difference attributable to "antigravity".

The arguments against antigravity

According to the Morrison argument, if antigravity existed, a matter - antimatter pair on the earth's surface could be lifted adiabatically to a height h with no energy loss. The energy of the photons produced by the pair's annihilation would then be blue-shifted when going back to the earth's surface, so that when the energy is reconverted into the pair, the pair would have acquired kinetic energy, implying the violation of energy conservation. Soon after, Schiff examined antigravity from the perspectives of the principle of equivalence and quantum field theory [55]. He wondered if the contribution of antigravity from positrons in atomic vacuum polarization diagrams would have been seen in the Eötvös experiment [56]. He concluded that the effect would have been so big that it should have been detected in this kind of experiment, for this reason antigravity could be ruled out. Some other authors came to a similar conclusion in the perspective of modern field theories [57, 58].
Another argument was provided by Good [59] in a predictive paper published prior to the discovery of the CP violation. Good noticed that if antigravity existed, the K_L^0, which is a linear combination of the K_0 and the $\overline{K}_0$, would regenerate into the K_S^0. This is due to the fact that the K_0 and $\overline{K}_0$ would experience different phase shifts from the antigravity gravitational potential. Even from a current perspective, this argument can rule out some hypotheses, it does not, however, rule out all recent hypotheses.

The arguments in favour of antigravity

According to Nieto and Goldman [48], the arguments presented in the previous paragraph, do not directly transfer over to the standpoint of modern field theories. Furthermore, the existence of two types (of cancelling) new contributions predicted by modern theories implies that new anomalous contributions could be disguised in matter experiments. When these facts are considered, even recent principle-of-equivalence experiments cannot rule out an observable anomaly in antimatter's gravitational acceleration.
Moreover there are a few arguments that are presented by Hadjukovic in favour of antigravity.
The first one is the hypothesis that the observed CP violation in the decay of the neutral Kaon (K_0) [60] could be explained by a repulsive gravitational interaction between the earth and antiparticles, as proposed in [61].
The second one is the antimatter isodual theory [62, 63].
The third one is the evidence of the acceleration (rather than deceleration) of the universe's expansion [64, 65]. Antigravity could be a possible explanation for the universe's accelerating expansion [66, 67].
Moreover this lead to the creation of alternative cosmological theories in which antimatter's gravitational acceleration differs from that of regular

matter [9, 10].

1.2.2 Anti-hydrogen and gravity

In the context of the ALPHA experiment, following Scott Menary's article [68], we have to consider that the proton, as well as the antiproton, is a composite system. In these systems the masses of the valence quarks ((uud) for p or ($\overline{\text{uud}}$) for $\bar{p}$) contribute just around 1% to the (anti)proton mass.
In the case of the proton, from lattice QCD calculations [69] the following contributions to the proton mass were found: quark condensate ($\sim 9\%$), quark kinetic energy ($\sim 32\%$), gluonic field strength ($\sim 37\%$), and anomalous gluonic contribution ($\sim 23\%$).
Moreover the experimental measurements of the proton's gravitational form factors based on the J/ψ photoproduction [70, 71] agree with what expected from lattice QCD [72, 73].

In order to extract the antimatter fraction of the antiproton mass one has to consider that, assuming that CPT symmetry holds, all the contributions to the proton mass listed before have the same numerical value for the proton and the antiproton. But, some of them have to be considered as matter under the gravitational interaction and the others as antimatter. In particular, the gluonic field strength and the anomalous gluonic contributions are considered as matter. This is supported by torsion-balance [74] experimental results and by the recent MICROSCOPE experiment results [75]. Also the quark condensate contribution (given by the "sea" quarks or the virtual $q\bar{q}$ pairs) is the same for proton and antiproton and behaves as matter under gravity. So the antimatter contribution to the antiproton mass should be given by the antiquark kinetic energy ($\sim 32\%$) and the antiquark masses ($\sim 1\%$).
Scott Menary in his article [68] attributes to the antimatter fraction of the antiproton mass the uncertainty of 30% on the lower bound, in this way the antimatter contribution is estimated to be $(33^{+6}_{-10})\%$.
This result can be coupled to the Villata theoretical proposal for the description of anti-gravity based on the application of the CPT invariance to the geodesic equation of GR, without modifying the GR theory or introducing new interactions. In this way he finds a generalised Newton law with a minus sign for matter-matter and a plus sign for matter-antimatter interactions:

$$F(r) = -G\frac{(\pm m)(\pm M)}{r^2} = \mp G\frac{mM}{r^2}. \tag{1.3}$$

By using equation 1.3, in [68] the gravitational force and the gravitational acceleration of anti-hydrogen ($a_{\bar{H}}$) in the Earth gravitational field (assuming antigravity) are calculated:

$$F = -G\frac{M_E M_{\bar{H}}(1-2\bar{f}_{\bar{H}})}{R_E^2} \;\rightarrow\; a_{\bar{H}} = (1-2\bar{f}_{\bar{H}})g \tag{1.4}$$

where $\bar{f}_{\bar{H}} \simeq 0.33^{+0.06}_{-0.10}$ is the fraction of the anti-hydrogen mass composed by antimatter (considering the contribution of the e^+ to be negligible). So in the antigravity scenario, the gravitational acceleration of $\bar{H}$ would be $a_{\bar{H}} = (0.33^{+0.10}_{-0.06})g$.

In conclusion even if the Villata anti-gravity scenario would be valid, the ALPHAg experiment wouldn't expect to observe anti-hydrogen "falling up", but just a deviation from the normal gravity g would be expected. In particular anti-gravity could be ruled out if ALPHAg could reach a precision of at least 5% in the determination of the gravitational acceleration of anti-hydrogen.

Chapter 2

The ALPHA experiment

The ALPHA experimental setup is hosted inside the so called Antimatter Factory at CERN. It makes use of the antiprotons delivered by the AD (*Antiproton Decelerator*) and ELENA (*Extra Low ENergy Antiproton*) decelerator complex. In this chapter the the AD and ELENA will be briefly described and subsequently the ALPHA experimental apparatus is presented.

2.1 The AD and ELENA

Antiprotons are created at CERN by the collision of a beam of high-energy protons with a solid iridium target [76]. The produced antiprotons are selected into a beam that is directed toward the the Antiproton Decelerator (AD) and the Extra Low ENergy Antiproton Ring (ELENA) where they are decelerated prior to being sent to the experiments at CERN's Antimatter Factory.
A sketch of the AD and the ELENA ring together with the Antimatter factory experiments is shown in figure 2.1.
To get the protons to the appropriate energy, they are first accelerated using a linear accelerator (LINAC4), then they are transferred to the Booster and finally to the Proton Synchrotron (PS), where they reach an energy of 26 GeV. Then this proton beam collides with an iridium target and $\sim 5 \times 10^7$ antiprotons are produced with energies of some GeV.

2.1.1 The AD

The Antiproton Decelerator [77, 78, 79] started its nominal operations in 2000. It is a circular decelerator that cools and decelerates antiprotons produced after the proton-Iridium target collision to a final energy of 5.3 MeV. A radio frequency cavity is used for bunch rotation in order to decrease the $\Delta p/p$ value of the $\overline{p}$. After this process, stochastic cooling and deceleration are applied, and finally when antiprotons reach an energy of $\sim$ 300MeV

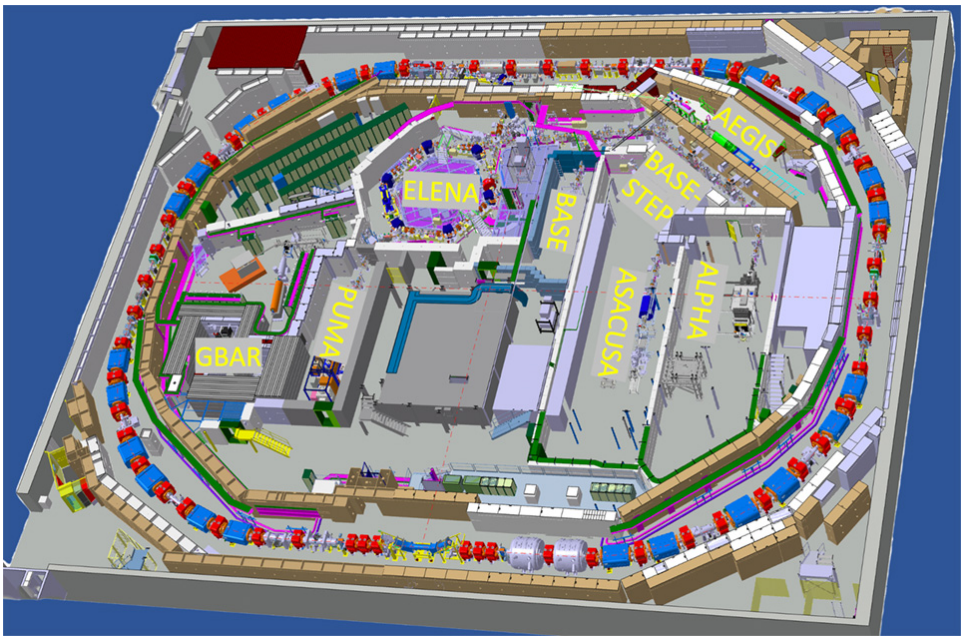

Figure 2.1: The Antiproton Decelerator (AD) and the Extra Low ENergy Antiproton Ring (ELENA) together with the Antimatter factory experiments

they are merged with an electron beam for cooling. On average, the AD receives more than 5×10^7 antiprotons but, because some are lost during the deceleration and cooling phase, only 3×10^7 are available after reaching the 5.3 MeV energy. The cooling cycle lasts about 100 seconds. Before LS2, when ELENA was constructed, the AD sent antiprotons directly to the experiments and it could only provide antiprotons for one experiment at a time.

2.1.2 ELENA

ELENA [80, 81, 82] is a synchrotron with a circumference of 30 m that is used to further decelerate anti-protons coming from the Antiproton Decelerator (AD). This synchrotron was built to reduce emittances in all three planes, allowing existing AD experiments to significantly improve their antiproton capture efficiency and allow the construction of new experiments that need very low anti-proton energies. It employs radio frequency and electron cooling to decelerate and cool antiproton beams from 5.3 MeV to 100 keV in roughly 20 seconds. During the procedure, around 40% of the antiprotons are lost. The remaining 1.8×10^7 antiprotons are divided into four groups of around 7.5×10^6, each of which can be directed to the different antimatter experiments at the same time.

The Antiproton Decelerator and ELENA currently deliver low energy antiprotons to various experiments that explore antimatter and its properties, that is: ALPHA, AEGIS, ASACUSA, BASE, GBAR and PUMA.
Antiprotons from ELENA are being used by AEGIS [83] to create a pulsed beam of anti-hydrogen atoms. The anti-hydrogen beam will then be passed through a Moire deflectometer coupled to a position-sensitive detector in order to determine the value of the gravitational interaction between earth and anti-hydrogen to an expected precision of a few percent.
The goal of ASACUSA [84] is to measure with high precision the hyperfine structure of anti-hydrogen and compare it to the precisely-known value for hydrogen. Because this quantity is particularly sensitive to magnetic fields, ASACUSA's goal is to construct a beam of anti-hydrogen atoms that can be delivered to a region with no interfering fields.
BASE [85] is looking for discrepancies between matter and antimatter properties by measuring the magnetic moments of protons and antiprotons. Using two Penning traps the experiments aims to measure the antiproton magnetic moment to a previously unattainable precision of a part-per-billion.
GBAR [86] intends to measure anti-hydrogen's gravitational acceleration. GBAR first combines the antiprotons with two positrons to generate positively charged anti-hydrogen ions. These ions, even if they are more harder to make than simpler anti-atoms, can be manipulated in an easier way as they are charged. These ions will be brought to temperatures of the order of μK using laser cooling techniques before being deprived of the extra positron, changing them into anti-hydrogen atoms. These anti-hydrogen atoms are then dropped from a height of 20 cm, and their annihilation at the bottom of the drop is detected.
PUMA [87] is intended to transport antiprotons to the ISOLDE experiment for investigation into rare nuclear-physics events. The experiment includes an antiproton trap divided into two zones and a detector. The first trap stores antiprotons. The second combines antiprotons and unstable atomic nuclei that are created at ISOLDE and decay too quickly to be transferred anywhere else. In the second trap, the detector detects the products of antiproton-nucleus annihilations.
Older experiments such as ATHENA, ATRAP and ACE were using AD, but they are now completed.

2.2 The ALPHA experiment

The main components of the ALPHA experimental apparatus, shown in figure 2.2, are the catching trap (described in section 2.3), the positron accumulator (described in section 2.4) and the ALPHA2 and ALPHAg apparatus described in section 2.6 and 2.7, respectively.
The ALPHA2 and the ALPHAg atom traps are connected to the catching trap and to the positron accumulator via the beamline and the interconnect (2.5). In the catching trap the antiprotons from the AD and ELENA are trapped and cooled, while in the positron accumulator the positrons emitted by a ^{22}Na source are trapped and accumulated. Afterwards the antiprotons and positrons plasmas are sent to the ALPHA2 or the ALPHAg atom traps in order to be mixed to form anti-hydrogen atoms.
The ALPHA2 experiment has the goal of measuring the laser-induced transitions between principal energy levels of the anti-hydrogen atom for CPT testing. The ALPHAg experiment has the goal of measuring the Earth's gravitational acceleration on anti-hydrogen for WEP testing.

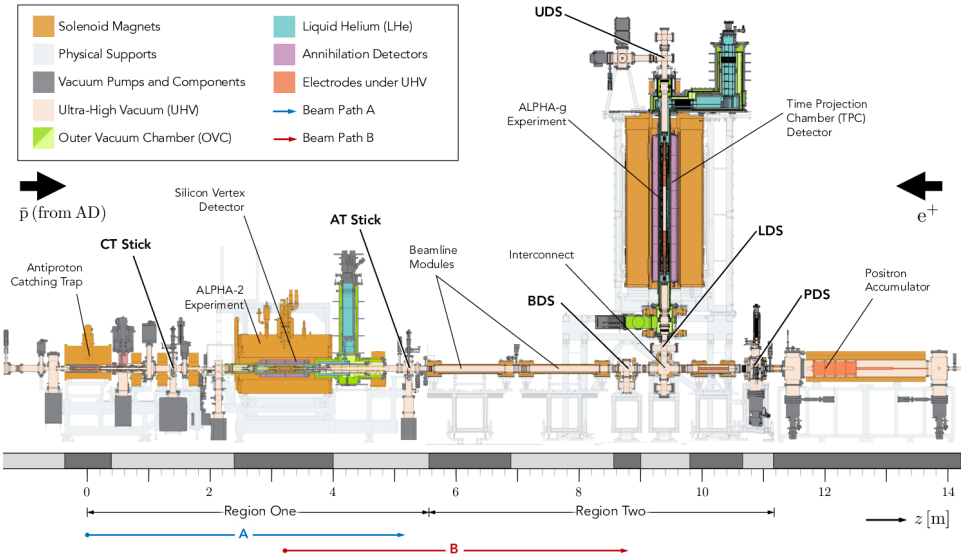

Figure 2.2: The ALPHA experiment including the catching trap, the ALPHA2 experiment, the beamline, the positron accumulator and the Na^{22} source, and the ALPHAg apparatus. Figure taken from [88].

2.3 The catching trap

The ALPHA catching trap (CT) is a Penning trap (particularly, a Penning-Malmberg trap) designed to capture, cool, and finally accumulate the antiprotons ($\bar{p}$) delivered by AD and ELENA decelerators.
The Penning trap electrodes of the CT are shown in the scheme in figure 2.3. The ALPHA CT's magnet is a superconducting solenoid that can generate a maximum magnetic field of 5T. Nonetheless, the CT's regular procedures use a magnetic field of 3T.

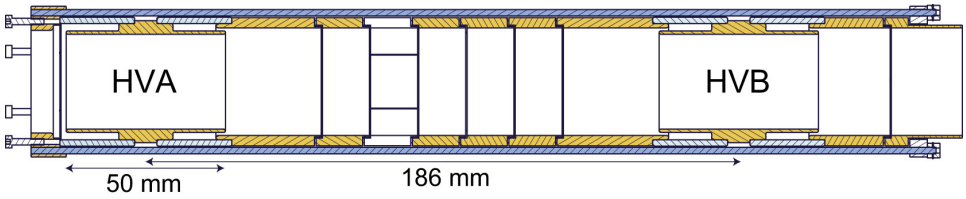

Figure 2.3: Scheme of the CT electrodes. The antiprotons enter from the left. Once inside the trap, the high voltage electrodes HVA and HVB ramp up to trap the antiprotons, which cool sympathetically with the electrons loaded in the trap previously. (Figure from [89])

A helium gas compressor is used to cool the CT environment down to cryogenic temperatures. The vacuum pumps are capable of lowering the pressure to as low as ~ 10 mbar. The CT can stack many antiproton bunches and can function independently of the rest of the ALPHA apparatus, so that it can be used as a $\bar{p}$ accumulator.
The $\bar{p}$ provided by ELENA have too much energy to allow the creation of $\bar{H}$, thus the $\bar{p}$ are further slowed down by a succession of thin foils of different materials known as the degrading foils. In particular, the bunch collides with a 0.2 mm beryllium and aluminum degrading foil. Approximately 0.1% of the antiprotons survive the collision and become trappable. When the $\bar{p}$ annihilate on the degrading foils, the reaction $\bar{p} + N \rightarrow n\pi^+ + m\pi^- + k\pi^0$ happens, where N is a nucleon, and $\pi^{\pm}$ are pions. Two pairs of plastic scintillators are placed at the sides of the CT to detect these pions produced in the interaction between $\bar{p}$ and the degrader. Each signal from the scintillators is processed by a NIM discriminator, and each pair is put in coincidence (AND) to reduce electronic noise. The pair's signal is then fed into a OR coincidence, which is then fed into a VME scaler module to record the counts. These detectors are highly useful for determining the quality of the AD beam as well as the efficiency of electron cooling in the CT.
The portion of the trap between the electrodes, labelled "HVA" and "HVB" in figure 2.3, is loaded with electrons before ELENA ejects the antiprotons to the ALPHA CT. Because of the cyclotron fast motion in the xy plane (discussed in chapter 3), electrons in a magnetic field release radiation, in

this case called cyclotron radiation. The time it takes for this motion to reach thermal equilibrium is [90] $\tau = \frac{3\pi\epsilon_0 c^3 m^3}{e^4 B^2}$ (derived also in equation 3.9 of chapter 3), where ϵ_0 is the vacuum permeability, c is the speed of light, m is the particle's mass, e is the elementary charge. The e^- cool down in ~ 0.3s, the $\bar{p}$ would cool down in $\sim 2.3 \times 10^9$s in the 3T magnetic field of the CT. For this reason the $\bar{p}$ are confined with the e^- and are indirectly cooled by Coulomb collisions with them. The efficiency of the electron cooling is determined by e^- density and the degree of overlap between the e^- plasma and the $\bar{p}$.

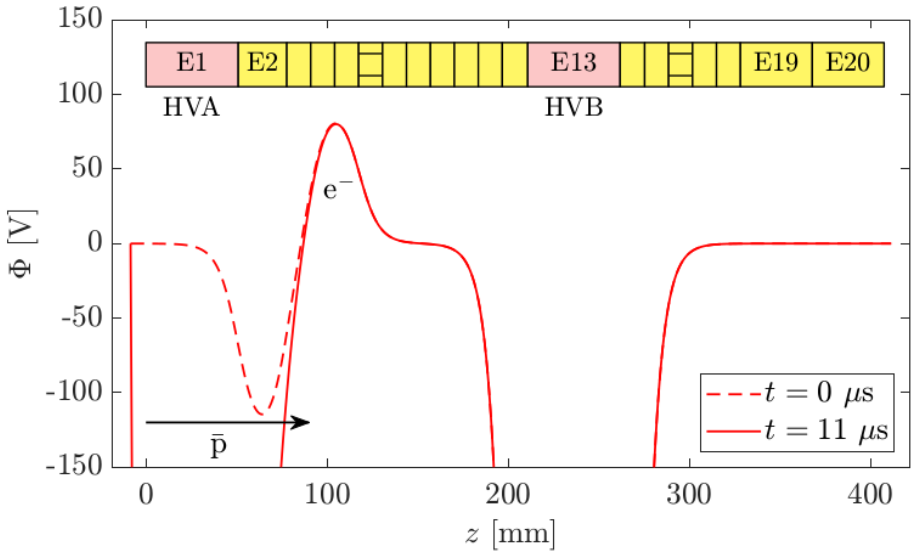

Figure 2.4: The electrodes and the axial trapping potential in the catching trap. The antiprotons enter from the left, once inside the trap, the high voltage electrode E1/HVA ramps up to trap the antiprotons, which cool sympathetically with the electrons loaded previously. Figure taken from [91].

In the context of $\bar{p}$ catching, the electrodes labelled HVA and HVB (high-voltage "A" and "B") in figure 2.3 play a critical role. The HVB is biased at roughly 5kV after the CT has been loaded with electrons, so that the CT is able to trap antiprotons with energies lower than 5keV. HVA is then raised to 5kV a few hundred nanoseconds after the AD has expelled the beam allowing the antiprotons to sympathetically cool with the electrons (figure 2.4). Then, the HVA and HVB voltages are lowered in order to create a shallower well after a variable time of several tens of seconds, allowing the most energetic antiprotons (the ones not cooled) to escape and annihilate with the trap wall, this is the so-called "hot dump".
Moreover, a small antiproton plasma size facilitates transmission to the AL-

PHA2 or the ALPHAg atom trap. For this reason, a segmented electrode known as rotating wall (RW, the segmented electrode in figure 2.3) is employed to compress the antiproton plasma (see section 3.1.1 for further details). The torque imparted by the RW also creates a significant quantity of heat, which the electron rapidly loses through cyclotron radiation (section 3.1.1). Because pure antiproton plasmas do not reduce in size when the rotating wall is applied, due to their low density, compression is performed with the help of the electron plasma, and the mixed plasma system is observed to reach an equilibrium in which the antiprotons radial distribution follows that of the electrons. This equilibrium additionally also gives the required re-cooling of the antiproton plasma.
Before transfer, the electrons are eliminated from the plasma by applying the e-kicks. More than one e-kick is required to remove all of the electrons, after each of these, the electron-antiproton plasma is compressed with the RW (section 3.1.1).
The scintillators are not the only diagnostics in the ALPHA CT. The CT stick inserted at the far end of the Catching trap, facilitates the alignment of various devices with the electrode stack. The most important for the CT are a micro-channel plate (example of MCP in figure 2.5) with a phosphor screen for diagnostic reasons [92], an electron source filament, which provides electrons created by thermionic emission and is required for antiproton cooling, and a "pass-through" cylinder to allow antiproton transfer to the atom traps.

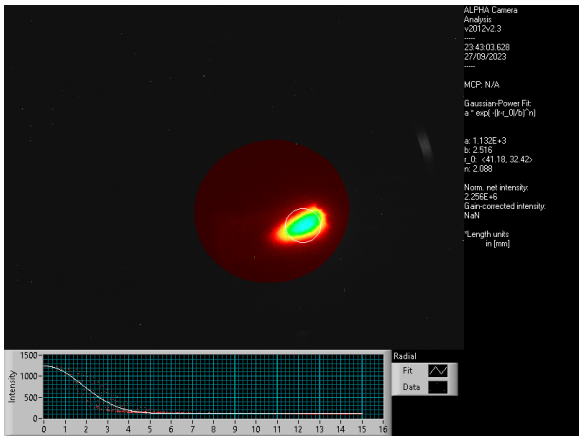

Figure 2.5: Example of an MCP image of the $\overline{p}$ plasma visualized after having applied the plasma manipulations for its preparation in the CT.

2.4 The positron accumulator

Positrons in the ALPHA experiment are produced through the radioactive decay of a ^{22}Na source:

$$^{22}_{11}\mathrm{Na} \rightarrow ^{22}_{10}\mathrm{Ne} + e^{+} + \nu_e \tag{2.1}$$

Because ^{22}Na has a half-life of 2.6 years, it produces an approximately constant amount of positrons on a daily basis. Emitted positrons typically have energies on the order of hundreds of keV and must therefore be cooled before they are captured. This is performed at ALPHA by using a multi-stage apparatus known as the positron accumulator, a schematic of this apparatus is illustrated in figure 2.6.

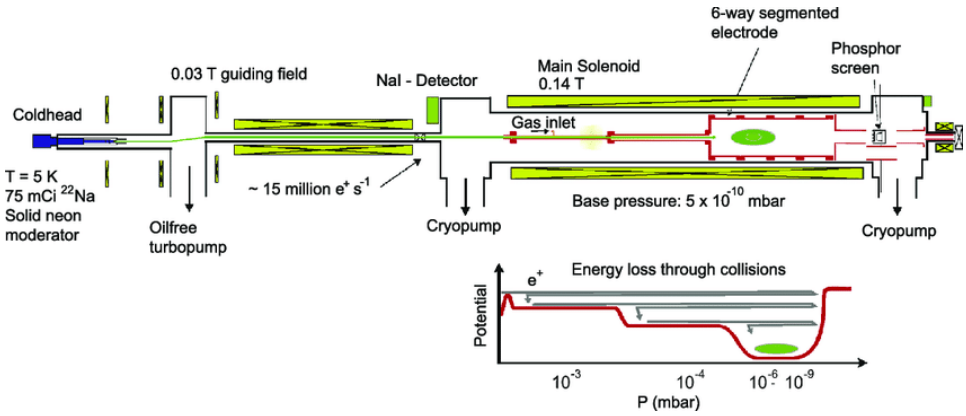

Figure 2.6: The positron beamline and the positron gas accumulator are shown. The lower panel shows the trap's axial electrical potential and how collisions end with the accumulation in the three stage Surko-type trap [93]. When the nitrogen line is closed, the gas is quickly pumped out in preparation for the positrons to be transferred to ALPHA2 or ALPHAg via the beamline. Figure taken from [89].

In the first stage, the positrons are slowed down by passing through a layer of solid neon, which acts as a moderator. While the vast majority of positrons are annihilated within the moderator volume, a small fraction (1%) survive with significantly lower kinetic energy of ∼80 eV. These lower energy positrons are sent using magnetic fields into the accumulator's Penning-Malmberg trap, which has a 0.14 T magnetic field and 7 cylindrical electrodes. The first two electrodes have a diameter of 12.7 mm each. The third electrode is 30.5 mm in diameter, while the last four electrodes are 200.7 mm in width. Near the second electrode, pure nitrogen gas is introduced into the trap. The gas diffuses gently downstream (to the left of the figure). A pressure gradient builds up within the trapping volume due to the three-stage electrode stack with varying diameters. Nitrogen operates as a

buffer gas, and positrons that bounce back and forth axially in the trap lose energy to the gas molecules.
Positrons are confined in the third stage of the trap over time by applying step-potentials to the electrodes, as shown in the lower panel of figure 2.6. Because the fourth electrode is segmented in 6 portions, the rotating wall method can be used to compress the positron cloud even further.
Thanks to a series of steps, the positrons can be sent to the ALPHA2 or the ALPHAg atom trap. To begin, the nitrogen gas is pumped out of the accumulator to prevent vacuum contamination of the beamline and atom traps. The mechanical valve that separates the accumulator from the beamline is then opened, and some electrode potentials are applied to eject the positron cloud, which is steered by the magnetic fields of the beamline to the ALPHA2 or the ALPHAg atom trap.

2.5 The Beamline

Figure 2.2 shows also the beamline that connects the positron accumulator to ALPHAg and ALPHA2. The specifics are given in [88]. Using magnetic fields created by a number of solenoids, the beamline is designed to transport positrons and antiprotons that have an energy below 100 eV. Positrons move from the positron accumulator to ALPHA2 or ALPHAg, while antiprotons travel from the catching trap to ALPHA2 or ALPHAg. The path that the beam has to travel is approximately 5 m for both particle species.
The transfer efficiency is in the 70 - 80% range for both species and bunch sizes commonly used. The particles can be steered upwards to ALPHAg or shot straight through from the positron accumulator to ALPHA2 via the interconnect, which is located beneath ALPHAg. The magnetic field lines in the beamline need to be continuous in all of the regions that need to be reached by the particles, as the particles follow these lines. The polarities along parts of the beam path need to be set in a different way with the current field configuration, depending on whether particles need to be transmitted to ALPHAg or ALPHA2. When running in the ALPHAg configuration in contrast to the ALPHA2 configuration, however, by providing a zero-field area between ALPHA2 and the interconnect, only the beamline sections (that have a bipolar power supply) need to change polarity.

2.6 The ALPHA2 apparatus

This section will provide a basic overview of the ALPHA2 apparatus. The ALPHA2 apparatus was developed in 2012, as a continuation of the older ALPHA1 apparatus, in order to measure the laser-induced transitions between anti-hydrogen's principal energy levels. The ALPHA2 experiment managed to first measure the 1S–2S transition [94, 4], and then the 1S–2P transition [3]. These measurements on anti-hydrogen were compatible within uncertainties with the same measurements performed on hydrogen.

2.6.1 Overall setup

The $\bar{p}$ trapped and cooled in the CT (section 2.3) and the e^+ accumulated in the positron accumulator (section 2.4) are transferred to the ALPHA2 atom trap, where the e^+ and $\bar{p}$ plasmas are mixed for the production of anti-hydrogen atoms. In the ALPHA2 atom trap can be sent microwaves and lasers in order to manipulate the particles (for example for ECR measurements [95]) and perform the spectroscopy of the anti-hydrogen energy levels.

2.6.2 The ALPHA2 atom trap

The atom trap is made of a Penning-Malmberg trap (34 electrodes and a 1 T external solenoid) for charged particles manipulations into a Ioffe-Pritchard trap (an octupole and five short mirror coils) for the confinement of neutral anti-hydrogen [96]. A simplified scheme of the ALPHA2 magnets and electrodes is shown in figure 2.7 (together with the silicon strip detector). Moreover there are two internal solenoids that can increase the magnetic field to enhance the cyclotron cooling (section 3.1.1).
To create anti-hydrogen, e^+ and $\bar{p}$ are combined in the middle region, where the octupole and mirror coils create the minimum of the magnetic potential to confine anti-hydrogen. It is possible to trap only anti-hydrogen atoms that are created with an energy smaller than the trap depth, about 0.5 K. When the trap is optimised, for each mixing cycle, up to 5×10^4 anti-hydrogen atoms are created and 30 of these have the suitable energy to be trapped [97]. As the anti-hydrogen lifetime in ALPHA2 is at least 66 hours [98], ALPHA can "stack" anti-hydrogen atoms over many mixing cycles so that it can accumulate around 1000 atoms.

2.6.3 The detector

Around the ALPHA2 atom trap is placed a three-layer silicon strip detector. When the anti-hydrogen atom hits the trap wall it annihilates, in this process the positron produces two gamma rays, and the antiproton creates three to five pions ($\pi^{\pm}$ and/or π^0). The charged pions are detectable and their

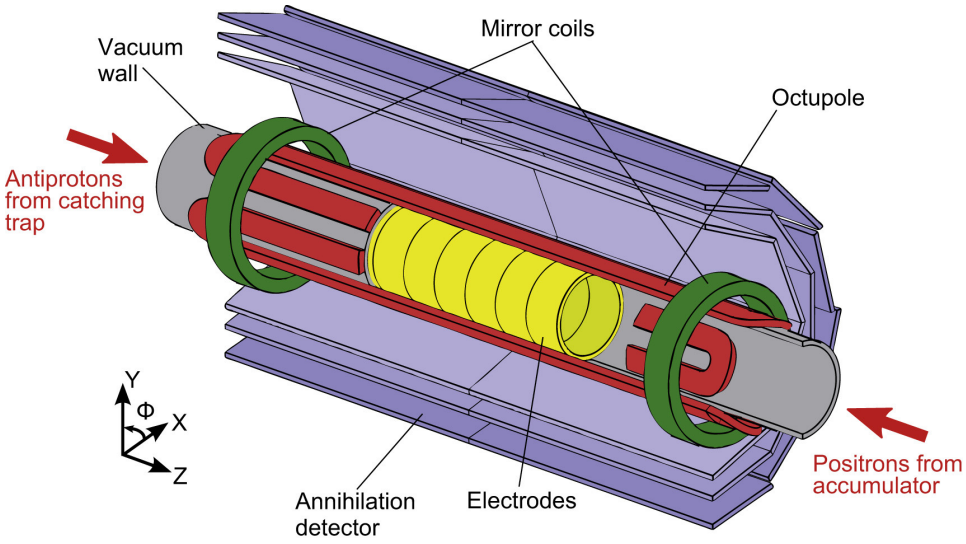

Figure 2.7: The figure shows a schematic of ALPHA2's anti-hydrogen production and trapping region. $\bar{p}$ and e^+ plasmas are prepared and manipulated on each side of the production region before being combined to create anti-hydrogen at the center of the trap where the minimum of the magnetic field is present. The apparatus is immersed in a uniform axial magnetic field of 1 T generated by an external solenoid, not shown in this scheme. Figure taken from [89].

tracks allow for the reconstruction of their annihilation vertex. However, the detector is not able to distinguish between annihilating antiprotons and anti-hydrogen atoms because of its low sensitivity to gamma rays, but all antiprotons can be eliminated from the trap after mixing by ramping down the electrodes field. The main source of background are cosmic rays, that are rejected by machine learning techniques based on boosted and bagged decision trees, considering the different topology of annihilation and cosmic events.

2.7 The ALPHAg apparatus

In this section the ALPHAg apparatus will be described. In particular this section presents the overall setup of the ALPHAg experiment. Then a more detailed description of the different ALPHA sections is given. These sections include the ALPHAg atom trap, with the electrodes and magnets composing it, and the detectors.

2.7.1 Motivation

Testing the Weak Equivalence Principle with charged antiparticles and particles is a challenging experiment [99]. Witteborn and Fairbank's [100, 101] historical tests at the end of the 1960s never gave compelling results for electrons, nor did they manage to measure the free fall acceleration of positrons. They did, however, pioneer the idea of measuring antimatter gravity. Due to the increasing availability of low-energy antiproton sources in the 1990s, another experiment to test the antiproton gravitational acceleration was suggested but never carried out [102, 103].
Because it is neutral, the $\bar{H}$ is a good candidate for a gravity experiment. Positronium, that is made of a bound state of an electron and a positron with a very short lifetime of 142 ns, is another possible candidate, although it is not totally composed of antimatter. The antineutron would be an excellent test system, but the technological obstacle is currently insurmountable. Moreover a muonium – an exotic atom consisting of an electron bound to an antimuon – gravity experiment has been proposed (MAGE) [104].

2.7.2 Overall setup

Figure 2.8 shows a sketch of the essential components of the entire apparatus. The external solenoid, the detectors, the cryogenic system, the magnets, and the electrodes at the centre of the system are the key components of ALPHAg.
The electrodes and magnets are separated into three regions: an upper trapping region, a lower trapping region, and a middle analysis region (see figure 2.9). Each trapping zone works, as the ALPHA2 atom trap, with a Penning-Malmberg trap embedded in an Ioffe-Pritchard trap. The magnetic field control in the upper and the lower trap places is insufficient to perform a "precision measurement" of antigravity, whereas the analysis region provides a greater degree of control. In the 2022 data taking however, the only full commissioned trap was the bottom one, and the gravity measurement was performed using this trap. The ALPHA experiment, on the other hand, intends to employ the analysis region for the next precision measurement. Although the analysis region is not intended to capture charged particles and produce anti-hydrogen, anti-hydrogen can be moved from one of the

trapping regions to the analysis region. Because of the fields formed by Eddy currents, having a trapping region on either side of the analysis region assures symmetry around it. A full strength region at each end of the detector also assures strong detector coverage above and below the region from where the anti-hydrogen is released.

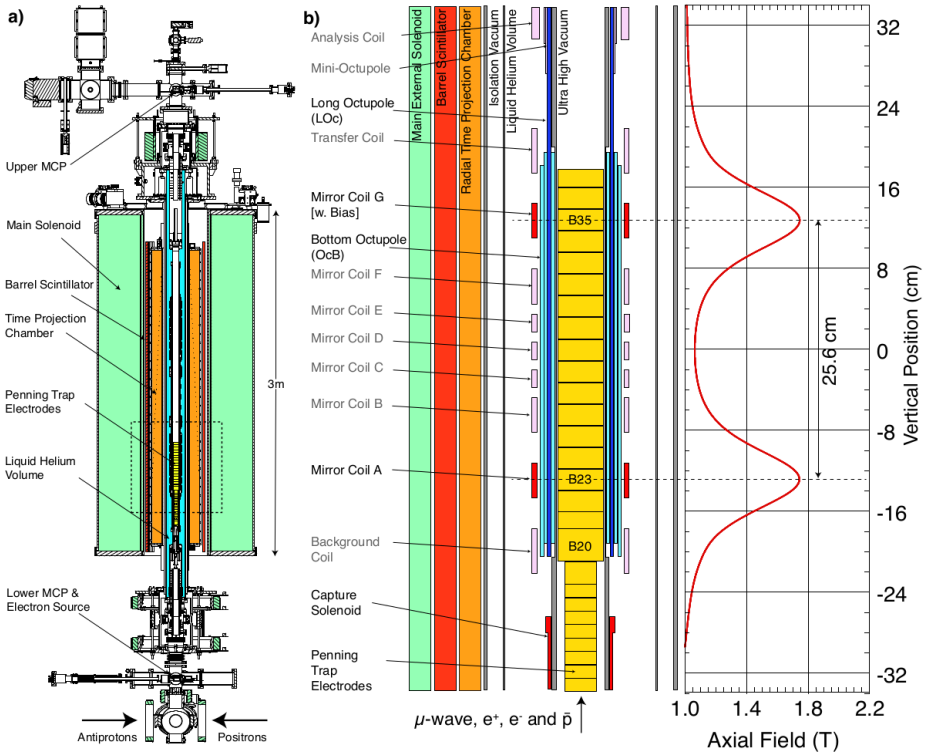

Figure 2.8: a) Cross section of the ALPHAg apparatus. The entire device includes three anti-hydrogen trap regions; only the bottom part is used for this measurement. b) View of the bottom anti-hydrogen trap (highlighted with a box in a) illustrating the Penning trap for anti-hydrogen production and the superconducting coils forming the neutral atomic trap. The axial field profile on full current is shown on the right. The mirror coils B-F, the analysis coil, the mini-octupole, the transfer coil and the background coil are not used for this measurement. The capture solenoid is used for charged particle transfer and manipulations and is de-energised for gravity measurements.

2.7.3 The ALPHAg measurement strategy

The gravity measurement involves trapping $\bar{H}$ in one of the vertical atom traps and gradually lowering the mirror coils at each end, allowing the anti-

hydrogen to escape axially. The gravitational attraction manifests itself as a difference in the number of anti-atoms escaping downwards and upwards. The axial location of the resulting annihilation vertices can be determined by the detector surrounding the trap.
Here ΔB_g defines the magnetic field difference it would take to cancel the effect of gravity for a given difference in height. The initial plan was to conduct two different measurements: the "Up/down measurement" using the full strength region (mirror A and G coils) and a "precision measurement" using the analysis region.
The "up/down measurement" would have been able to just evaluate the sign of g by making two different measurements: one applying a $\Delta B = B_G - B_A = \Delta B_g$ and one with $\Delta B = -\Delta B_g$. In the full strength region (A and G), the distance between the centers of the outermost mirror coils is 256 mm. This distance corresponds to a gravitational potential energy difference of 4.20×10^{-27}J for an hydrogen (or anti-hydrogen assuming $\bar{g} = g$) atom. When the anti-hydrogen is in its ground state, its magnetic moment is approximately equal to one Bohr magneton, hence the gravitational potential energy difference can be opposed by a magnetic field difference of $\Delta B_g = 4.53 \times 10^{-4}$ T. As a result, the maximum uncertainty on the magnetic field produced by each of the two mirror coils must be of the order of $\sigma_B \sim 10^{-4}$ T.
The analysis region instead is designed to determine the value of the gravitational acceleration on $\bar{H}$ with a precision within 1%. This measurement will be referred to as the "precision measurement". Considering that the "precision measurement" was planned to be done applying magnetic field offsets separated by $2\Delta B_g/100$ and that the analysis region is 400 mm long, the maximum uncertainty on the field produced by each of the mirrors must be of the order of $\sigma_B \sim 10^{-6}$ T.

2.7.4 Electrodes

ALPHAg requires electrodes to move and manipulate charged particle plasmas and create Penning traps. On the right of the figure 2.8 there is a representation of the electrode stack of the bottom full strength region (the bottom trap). Each electrode includes a 75 or 150 V bipolar amplifier that controls the voltage on the electrode. Electrodes 3 and 12 are divided into six parts so that they can be used for Rotating Wall compression as described in section 3.1.1.

2.7.5 Magnets

This section will go over the specifics of the internal magnets [105] that were (and will be) used to measure the gravitational acceleration on $\bar{H}$. Brookhaven National Laboratories (BNL) produced these magnets. Figure

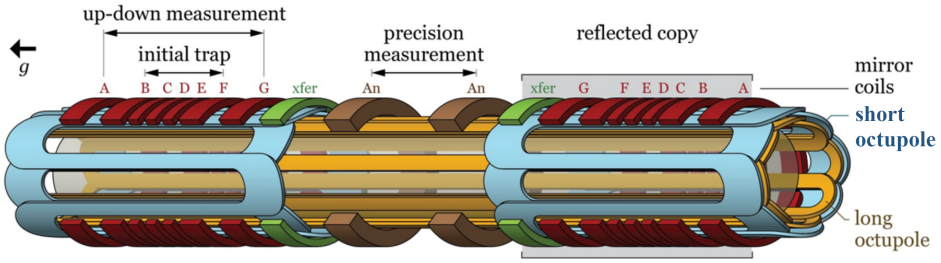

Figure 2.9: This picture shows the ALPHAg magnets layout. The analysis region consists of the long octupole (LOc) (orange) and the two analysis coils (brown) for the "precision measurement", whereas the trapping region consists of the two short/boost octupoles (blue) and the two sets of mirrors A-G (MAGB) (red) (the ones effectively used for the gravity measurement of the 2022 data taking). The two transfer coils (green) are also shown.

2.9 is a 3D drawing of the ALPHAg magnet system. The blue and orange octupoles, as well as mirror coils from A to G in red, make up the two strong trapping regions, the bottom one was used for the 2022 data taking gravity measurement. The yellow long octupole and the brown analysis coils compose the precision measurement analysis trap, that will be used in the future for the "precision measurement". The green transfer and background coils can aid in the transfer of charged particles or anti-hydrogen between different locations of the apparatus. The charged particles are initially trapped and cooled by the two outermost solenoids (not shown in the figure). The outermost magnet of the ALPHAg apparatus is the external solenoid that generates a 1 T background field for charged particle radial confinement.
The BNL manufacturers had to reduce the amount of superconducting material used to make the magnets of the analysis region, increase the distance between the analysis coils and the Strong trapping region, and make the magnet system symmetric around the analysis region in order to meet the strict requirements for the fields in the analysis region [105]. As a result, the analysis trap creates a magnetic field that is too shallow to trap enough anti-hydrogen from positrons and antiprotons mixing, hence anti-hydrogen must be created and stacked in the full strength region before being moved to the analysis region. In order to make the field in the analysis region as smooth as possible, the end-turns of the long octupole were located as far away as possible from the analysis region and the octupoles were winded with a wire as thin as possible to reduce the amount of material that can have persistent currents. The end-turns of the LOc overlap with the full strength region. As a result, the short octupoles could be constructed with fewer layers, but the radial confining field of the full strength trap must be created with both the long and the short octupole energized. To maximize the field symmetry in the analysis region, most bottom region magnets are

coupled in series with their upper region analogues. Mirror coils from B to F, the short octupoles, and the background and transfer coils are operated in series. Mirrors A and G, as well as the analysis coils, corrector coils and octupoles, and the capture solenoids, all operate independently.

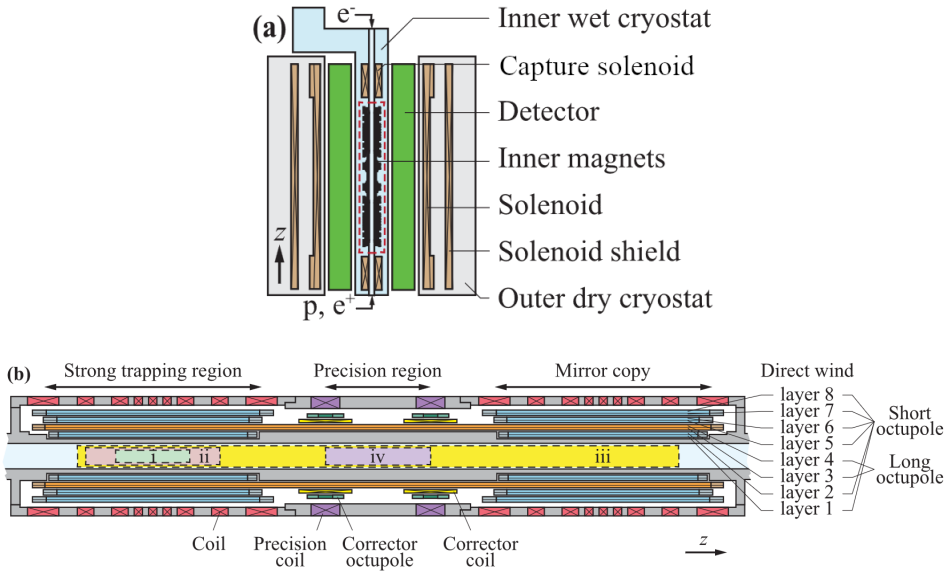

Figure 2.10: (a) A schematic of the ALPHAg magnet system's vertical cross-section. The apparatus is $\sim$ 4 m in height and $\sim$ 1.4 m in diameter. (b) A closer look at the inner magnets (indicated by red dashed rectangle in (a)). The inner magnets' height is $\sim$ 1.4 m and the diameter is $\sim$ 100 mm. Figure adapted from [105].

Capture solenoids

The capture solenoids (SoT and SoB) are located at each end of the magnet region to trap the charged particles as they are directed towards ALPHAg from the interconnect (see figure 2.10 (a) and figure 2.11). Each capture solenoid, combined with an electrodes stack, forms a Penning-Malmberg trap. In addition to the external solenoid field, the capture solenoids are made to produce a field of 3 T. The capture solenoids are located on the outer edge of the external solenoid, and the wiring layout and density are designed to compensate for the external solenoid's magnetic field gradient.

Strong trapping region

The long octupole, the top and bottom sets of mirrors from A to G, and the short octupole make up the so called strong trapping region (see figure 2.9). Around the analysis region, the two strong trapping regions are symmetric.

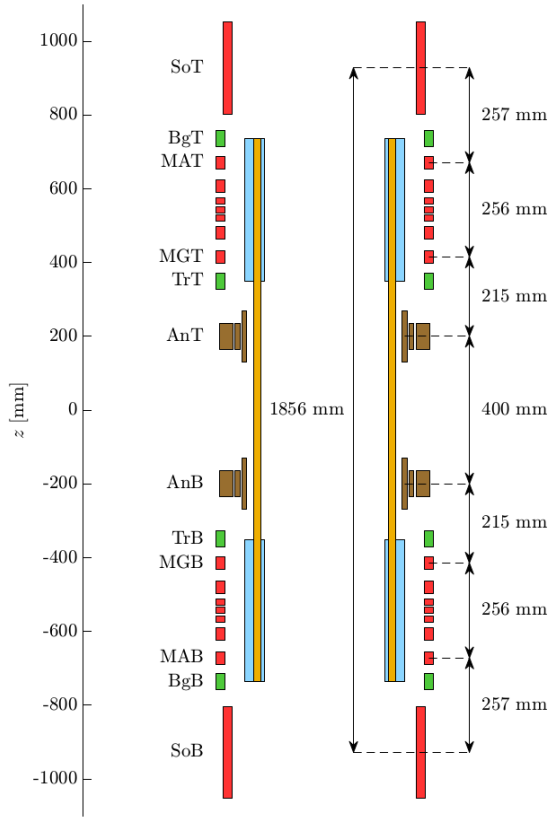

Figure 2.11: 2D representation of the ALPHAg magnets (with name abbreviations). Figure taken from [91].

Mirrors A and G supply the axial confinement for the up/down measurement since between the two there's the biggest gravitational potential energy difference in the apparatus.
In a more sophisticated measurement strategy, anti-hydrogen is first trapped between mirrors B and F and the trapping region is subsequently enlarged to A and G to adiabatically cool anti-hydrogen. The mirrors in the center can be utilized to make the trapping potential deeper between B and F, and to modify the field shape in order to obtain the least energetic $\bar{H}$ possible. To get the end-turns of the LOc as far away from the analysis region as possible, the LOc spans over the whole strong trapping region. The LOc , however, cannot offer a strong enough radial confinement for the strong trapping region, hence this action is increased by the short octupoles. All the octupoles are built of bi-layers, which are two layers of wire with oppositely wrapped end-turns to reduce the end-turns' solenoid-like field. The short octupoles have one bi-layer on the inside and two on the outside of the long octupole. The field created by the short octupole is around three times

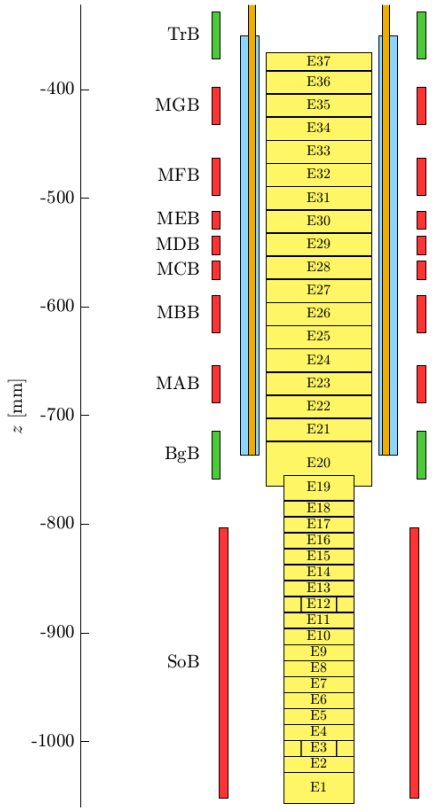

Figure 2.12: 2D representation of the magnets and electrodes of the ALPHAg bottom trap (from TrB to BgB) and of the region used for recatching $\bar{p}$ and $e+$ plasmas once they enter the ALPHAg apparatus (SoB region). Figure taken from [91].

stronger than the field produced by the long octupole.

Precision analysis region

The two analysis coils (AnT and AnB in figure 2.11) and the long octupole are the key components of the analysis region. These magnets are intended for use in the "precision measurement". The analysis coils are constructed in order to meet the requirements of $I_b > I_t$ for current in the coils (where b stands for the bottom coil and t the top coil), so that magnetic potentials fulfil $U_b = U_t + U_g$ (where U_g is the gravitational potential).
However, if this requirement is fulfilled on axis at $r = 0$, it won't be true for $r > 0$, where $U_b(r > 0) > U_t(r > 0) + U_g$. For a given value of I_b and I_t, at the axial centre $|B(r)|$ for each magnet might be made the same by having the coil with the stronger current, axially longer than the other. However, the field curvatures will only match for a specified current for a

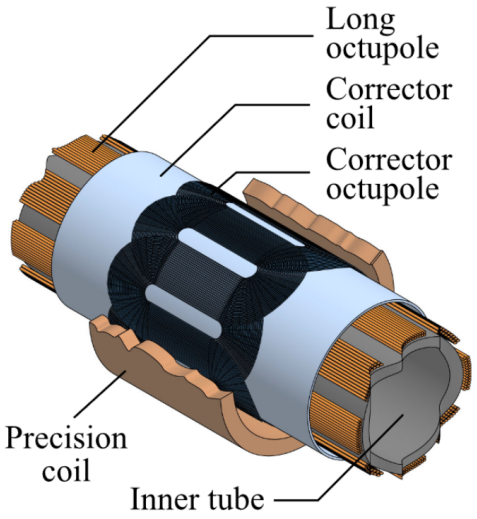

Figure 2.13: A detailed sketch of the region surrounding an analysis coil. A corrector coil and a corrector octupole are added to each of the primary analysis coils to make the magnetic field match the field of the other analysis coil for all the different values of r.

given set of magnet size. A solution to this problem is to install a long low-power "corrector" solenoid in the same position of of the analysis coils, this allows the length of the analysis coils to be adjusted [105]. The situation becomes more difficult at higher radii due to the octupole's contribution to the total magnetic field. The octupole field is perpendicular to the z axis and adds to the parallel field of the solenoids at the axial solenoid center. The total magnetic field at the upper mirror is smaller than the one at the lower because $I_b > I_t$. A short low strength corrector octupole is inserted between the analysis and corrector coils to mitigate this effect. Figure 2.13 depicts a scheme of the magnet setup around the precision analysis coil.

Transfer and background coils

The short octupole end-turns are willingly separated from the analysis coils by a 120 mm gap, in order to prevent field inhomogeneities. These gaps are too large to perform an anti-hydrogen transfer without losses from the trapping region to the analysis region, with only the 1 T background field. For this reason, a transfer coil has been installed in each gap (TrB and TrT in figure 2.11). Because the coils cause an asymmetry around the strong trapping region, two identical coils, called background coils (BgB and BgT in figure 2.11), are added outside the mirror coil A.
In the event that the external solenoid is not working, the field from the background coil can be employed to assist in the transfer of charged particles from the capture solenoid to the full strength region. It can also be

used, together with the transfer coil and the rest of the solenoids in the full strength region, to create a background field across the full strength region replacing the external solenoid field, except the field will be less uniform. Because the background solenoid covers the short and long octupole ends, finally, it can be used to cancel the axial field component produced by the octupole end-turns.

External solenoid

When supplied with a current of 191 A, the external solenoid immerses the entire ALPHAg experiment in a 1 T field. Because it was made by Babcock Noell GmbH, it is also called the Babcock magnet. Aside from the main coil, there is an independent shim coil that was added after the main coil was constructed. The shim coil is designed to smooth out the field produced by the main solenoid's imperfections. Its position was chosen by measuring the main coil's field in different regions. The external magnet is superconducting and is housed in a cylindrical vacuum vessel that also contains the cryocoolers and thermal insulation. In order to make room for the detector, internal magnets, and cryostat, the bore of the vessel is empty. It stands roughly 3 meters in height, has a 1.5 meter diameter, and about 2500 kg in weight. The inner diameter is approximately 0.5 m. The main coil is made up of several sections that are wired in series.

2.7.6 The detectors

The identification and vertexing of the $\bar{H}$ annihilations is critical for monitoring the experiment and achieving relevant physics results. This includes identifying $\bar{H}$ annihilations and rejecting cosmic rays. The treatment of the cosmic background is discussed in more detail in sections 4.2.1 and 4.4.1.
The distance between the vacuum chamber edge where annihilation happens and the first point where it is possible to measure the annihilation products is several centimetres in the ALPHA experiment, and the abundance of material with high density (the electrodes and magnets of the Penning Trap and the Ioffe-Pritchard trap) causes a degradation of the tracking performance due to multiple scattering. ALPHAg's tracking detector is a radial Time Projection Chamber, or rTPC. For the rejection of cosmic rays, a scintillator bars detector (Barrel Veto) is utilized in conjunction with the TPC. The hit multiplicity and time delay between hits are two examples of Barrel Veto variables that can be used for cosmic ray classification: the former is low for cosmic rays compared to $\bar{H}$ annihilation, while the latter is large. This detector can also act as a trigger for the TPC. These two functions of the Barrel Veto require rapid response silicon photomultipliers and accurate timing front-end electronics.

The radial Time Projection Chamber (rTPC)

The ALPHAg rTPC is a gaseous tracking detector filled with a 70% Ar - 30% CO_2 mixture that allows to track a charged particle crossing its active volume providing different samples of its trajectory thanks to the electrons released by the gas ionization. For each point sampled on the trajectory, three spatial coordinates are determined concurrently.

Regarding the TPC mode of functioning, an electric field is always applied in the active volume in order to drift of electrons, produced by the primary ionization, towards high potential regions (from the inner cathode to the field wires) where they are collected. This current is then amplified (between the field wires and the anode wires) so that an analog signal proportional to the quantity of ionization created by the charged particle, and hence to its energy deposition, is acquired (at the outer cathode pads). The usual design of a TPC is such that the anode wire plates for the collection of the electrons are located at the barrel bases, so the electric field is parallel to the barrel longitudinal axis. The ALPHAg rTPC, instead, is an unusual barrel detector with a radial electric field: $E(r) = \frac{V}{\ln(b/a)} \frac{\hat{\mathbf{r}}}{r}$ where r is the radial coordinate, a and b are the inner and outer radii of the TPC, respectively, and V = 10 kV is the typical bias voltage applied. The z axis is vertical and pointing upwards. The electrons produced by the passage of the charged particles are thus collected at the detector's outer radius. As stated before, the electric field in more common TPCs is parallel to the magnetic field, but the rTPC in ALPHAg is quite long, this would imply long drift times in a complicated magnetic field environment, which might seriously degrade the accuracy with which a particle is tracked. The strict spatial requirements, such as the need for plasma diagnostics and an electron-gun at the top of the device and antiparticle injection and laser injection from the bottom, also influenced its design. While electrons are accelerated via the electric field $\mathbf{E}$ towards the outer wall, they scatter in random directions due to the interaction with gas atoms. As a result, the primary ionization drifts at a constant velocity given by $\mathbf{v_d} = \mu_e \mathbf{E}$ [106], where μ_e is the electron mobility of the gas, that is proportional to the average time between two collisions. The ionization is collected on the TPC outer wall (the pads), which is azimuthally (along ϕ) and axially (along z) segmented. Each segment is referred to as a pad and, the knowledge of which pad is hit by the drifting electrons, determines the position of each ionization along the particle trajectory. The radial coordinate r must be calculated from the ionization drift time t_d in order to uniquely establish the space-point along the charged particle track: $r = v_d t_d$. The measurement of t_d for each hit is the time interval between the trigger and the hit on the pad. The charge arriving at the pad is a small amount and needs suitable amplification. For this reason, a series of anode wires are biased to 3.5 kV and put in front of the pads, resulting in a huge localized electric field that produces secondary ionizations and charge

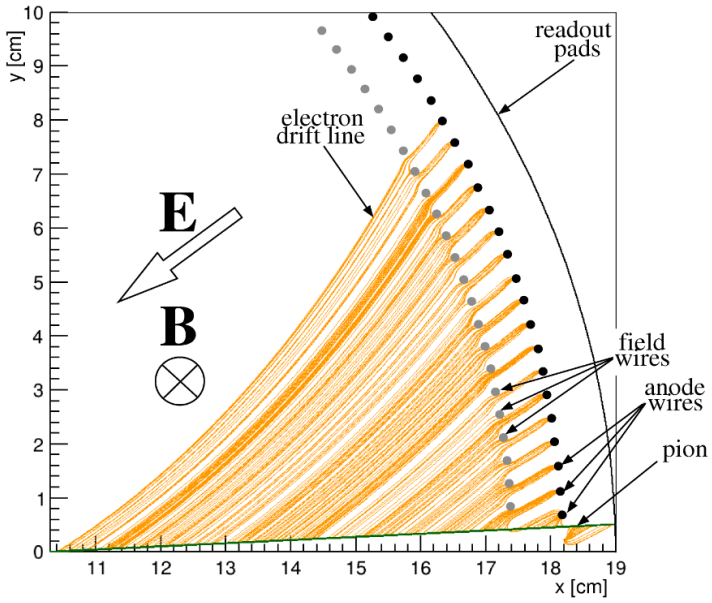

Figure 2.14: Monte Carlo simulation of the rTPC. A pion track (green) crosses the detector and is curved by a 1 T magnetic field. The orange lines represent drift lines of the electrons produced by ionization. Figure taken from [107]

multiplication. As the TPC is immersed in a magnetic field B, if the electric and magnetic fields are orthogonal, the drift follows the Lorentz force, and the angle *alpha* between the drift velocity and the electric field, known as the Lorentz angle, is given by $\tan\alpha = \omega\tau$, where $\omega = eB/m$ is the electron Larmor frequency. Thus, in the ALPHAg TPC the ϕ coordinate of the hit must be corrected for the value of α.

Regarding the TPC dimensions, the active gas volume is 1.8×10^5 cm^3 and it has a height of 230 cm in z, and extends from the inner cathode wall, at $r = 10.9$ cm, to the segmented outer cathode wall, at $r = 19.0$ cm. The drift region of the gas volume goes from $r = 10.9$ to 17.4 cm, and the proportional region (where electron multiplication happens) goes from $r = 17.4$ to 19.0 cm. The anode sensing wires which receive the signals are 256, while the outer cathode pads, which finally collect the multiplied electron signal, have a 576-fold segmentation in z and 32-fold in ϕ (11.25°), for a total of 18432 readout channels.

The Barrel Veto detector

The rTPC is surrounded by a barrel veto scintillator (BV), which offers extra information on annihilation events. During the 2022 data taking it

was primarily used to offer information on event topology as part of the cosmic background rejection analysis.

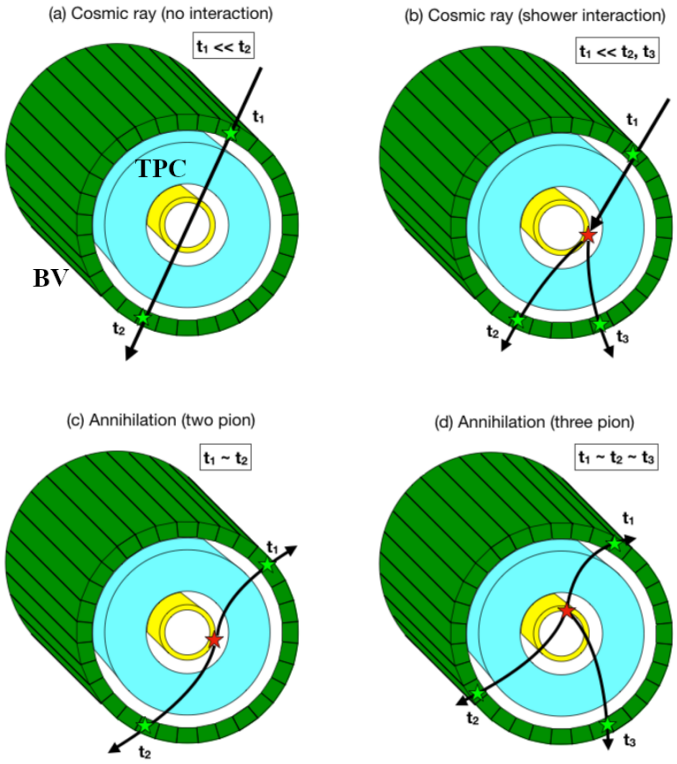

Figure 2.15: Representation of the different topologies of cosmic ray events and $\bar{H}$ annihilation events. In particular considering the time-of-flight (TOF) between different hits in the detector: cosmic rays cause a significant time delay between hits on the BV, whereas $\bar{H}$ annihilation causes several BV hits at the same time. Figure taken from [108].

In fact the main purpose of the Barrel Veto is identifying events caused by cosmic rays in order to reduce the cosmic ray background. This cosmic ray rejection relies on the different event topology that characterises cosmic rays and $\bar{H}$ annihilation events (see figure 2.15). The BV was not used as a true veto during the 2022 data taking because it was not used to remove background events in real time. Instead, it is used during offline data analysis to classify cosmic rays and actual annihilation products on an event-by-event basis.
The BV is made up of 64 - 2.6 m long and 2 cm thick - trapezoidal scintillator bars (Eljen Technology EJ-200). An array of six silicon photomultipliers (SiPMs) (MicroFJ-60035 SensL J-series) reads out the bars at each end, with each photomultiplier having an active area of 6 mm $\times$ 6 mm. Figure 2.16 shows a diagram of the layout of the SiPMs and how they are coupled

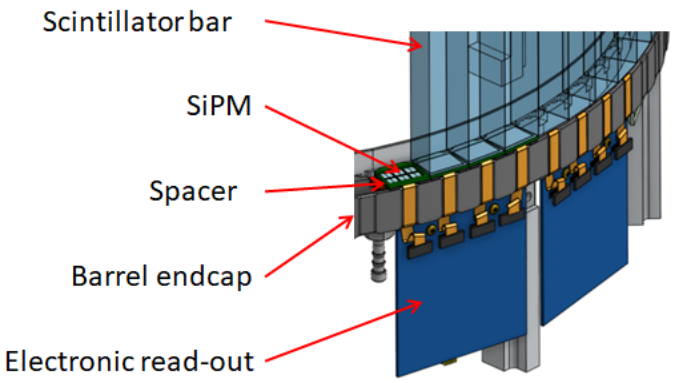

Figure 2.16: This figure shows the SiPM and electronics layout at the end of the scintillator bars. There are six SiPMs per bar end.

to the bars. The analogue signals from the six SiPMs at the top or at the bottom of a BV bar are summed on a front-end card on the detector and sent to an analog to digital converter (ADC) module and to a discriminator and then to a time-to-digital converter (TDC) for each of the 128 channels via 5m coaxial cables.

Regarding the detector's resolution characteristics, figure 2.17 shows the reconstructed annihilation vertex distribution in z for antiprotons annihilating on residual gas while being held for 2000 s in a short Penning trap. This kind of experiment gives a roughly point-like source in order to be able to test the ALPHAg detectors' resolution on the z annihilation vertex reconstruction. From the RMS of the distribution in figure 2.17 and subtracting the expected plasma width, the resolution found is of the order of ~ 2 cm.

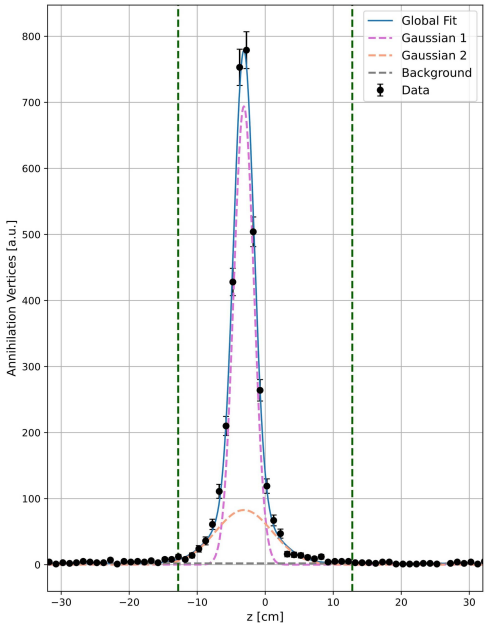

Figure 2.17: Trapped antiprotons ($\bar{p}$) in a short Penning trap for 2000 s provide an essentially point-like source of annihilation events. Where the annihilation happens due to the $\bar{p}$ interaction with the residual gas in the trap. Two Gaussian distributions and a flat background are used to fit the reconstructed vertex distribution in z (points with error bars). The standard deviations of the two distributions are 1.5 cm (Gaussian 1, that includes $\sim 70\%$ of the counts) and 4.2 cm (Gaussian 2, that includes $\sim 24\%$ of the counts). Both widths are much less than the distance between mirrors A and G (the magnet centers are indicated by green vertical lines). Figure taken from [6].

Chapter 3

Anti-hydrogen formation and gravity measurement procedure

This chapter gives the general description of the methods and traps used for confining charged particles and neutral atoms and the main techniques used in ALPHA for plasma manipulation. The final section gives the description of the measurement of the gravitational acceleration of anti-hydrogen performed by ALPHAg during the 2022 data acquisition.

3.1 Penning traps and plasma manipulations

A Penning trap is the device that allows ALPHA to handle antiparticles, positrons and antiprotons, as well as electrons. By using both electric and magnetic fields, this device traps charged particles in vacuum and constrains their motion. The Penning trap's principal purpose is to keep antiparticles separated from ordinary matter in order to prevent the annihilation between the two. A less evident purpose is thermal isolation in order to achieve extreme low temperatures suitable for the synthesis and trapping of anti-hydrogen. A Penning trap confines charged particles by using a crossing static electric field and a magnetic field generated by a solenoidal magnet. The electric field can be written in the form $\mathbf{E} = -\nabla\phi$, where ϕ is a scalar potential rotationally symmetric around the z-axis described by the formula:

$$\phi(r, z) = \frac{U_0}{2d^2}\left(2z^2 - r^2\right) \tag{3.1}$$

where d denotes the trap characteristic dimension, r and z are the radial and axial coordinates respectively. Because the equipotential surfaces of the potential ϕ are hyperboloids of revolution, one can make conducting surfaces, or electrodes, with these shapes, space them d apart, and apply

the static voltage U_0 between them to create an ideal Penning trap. (see figure 3.1).

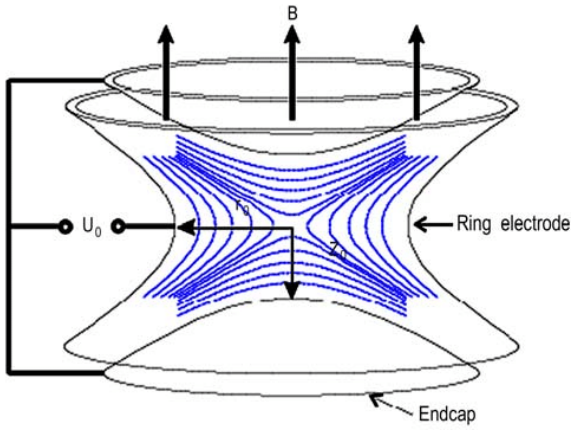

Figure 3.1: Scheme of the ideal Penning trap electric and magnetic field lines. The "rings" and the "end-caps" are hyperboloid electrodes. The figure is taken from [109].

From the sign difference between r and z in equation 3.1, where the potential has a minimum in one direction and a maximum in the other, one can deduce that it is not feasible to generate a minimum of the electrostatic potential in free space. For this reason a magnetic field B has to be added to constrain the particle's motion, in this example in the xy plane, in order to construct a trap. In the ideal Penning trap, the equation of motion of a particle with charge q and mass m is,

$$m\frac{d^2\mathbf{r}}{dt^2} = q(-\nabla\phi + \frac{d\mathbf{r}}{dt} \times \mathbf{B}) \tag{3.2}$$

where $\mathbf{r}$ is the position of the particle and can be solved analytically. The electrostatic force determines the motion in the z direction, which is a simple harmonic oscillator with angular velocity

$$\omega_z = \sqrt{\frac{2qU_0}{md^2}} \tag{3.3}$$

The motion in the xy plane, due to the confining magnetic force and the repulsive electrostatic one, has a frequency given by the cyclotron frequency (angular velocity)

$$\omega_c = \frac{qB}{m} \tag{3.4}$$

A charged particle's motion can be described as a superposition of three independent oscillation motions: the simple harmonic oscillation parallel to

B, with frequency ω_z provided by equation 3.3, the cyclotron motion in the xy plane, with modified cyclotron frequency given by the equation:

$$\omega_c' = \frac{1}{2}(\omega_c + \sqrt{\omega_c^2 - \omega_z^2}) \tag{3.5}$$

and the magnetron motion, because of the perpendicular **E** and **B** fields' cross-product [110], has magnetron frequency given by the equation

$$\omega_m = \frac{1}{2}(\omega_c - \sqrt{\omega_c^2 - \omega_z^2}) \tag{3.6}$$

Figure 3.2 shows a schematic representation of the orbits in this ideal form. The different frequencies have different order of magnitudes and follow a fixed order [90]: $\omega_c' \gg \omega_z \gg \omega_m$.

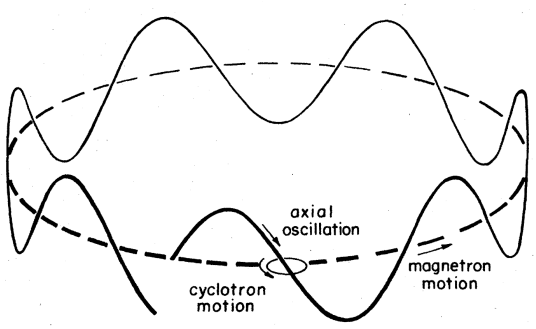

Figure 3.2: A charged particle's orbit in a Penning trap. The dashed line represents the magnetron circle component. This is combined with the axial oscillation and it results in the guiding-center motion (solid line). The total motion is calculated by adding the fast but small circular motion of the cyclotron about this moving guiding center. (Figure taken from [90]).

From equations 3.5 and 3.6 one can derive that $\omega_c = \omega_c' + \omega_m$. Combining this with the relation $\omega_c' \gg \omega_z \gg \omega_m$ one obtains that the modified cyclotron frequency is approximately equal to the cyclotron frequency: $\omega_c' \simeq \omega_c$.
The magnetron motion has a greater radius and is significantly slower than the other two. When the axial oscillation is added to the magnetron motion, the result is the so-called guiding-centre motion, which is shown in figure 3.2 by the solid line. Moreover there is the fast and small-amplitude cyclotron motion around this moving guiding-center.
One drawback of hyperboloid electrodes is that they surround the trapping region, making particle loading and monitoring difficult. While the electric potential in equation 3.1 allows for analytical calculation, there is no other advantage in this. To produce a Penning-Malmberg trap in the ALPHA traps the hyperboloid electrodes are replaced with cylindrical electrodes. This structure is particularly adaptable to the scenario useful for ALPHA

since numerous electrodes can be layered together to make a long trap that allows particles to enter from both ends of the cylinder and diagnostic instruments to be inserted. The motion of a charged particle inside the ALPHA traps is similar to that described above, but at different frequencies.

3.1.1 Plasma Cooling and Manipulation

In this section all the different techniques used by the ALPHA experiment to obtain the optimal shapes and energies of the different plasmas ($\overline{p}$, e^+, e^-) are described. These techniques are of paramount importance in order to produce anti-hydrogen in sufficient amounts to run the experimental measurement of the earth gravitational acceleration on anti-hydrogen.

Cyclotron cooling

When a charged particle is deflected by an external magnetic field, it emits cyclotron radiation, which is perpendicular to the magnetic field. With the Larmor formula one can calculate the power emitted by cyclotron radiation [111] (in CGS):

$$P = \frac{2}{3}\frac{q^2}{c^3}a^2 \tag{3.7}$$

where q denotes the charge of the particle, a is the centripetal acceleration due to cyclotron motion, and c is the speed of light. So the particle loses energy through this power radiated and as a consequence it slows down. This process is called cyclotron cooling. If one considers that the centripetal acceleration can be expressed as $a = \frac{qvB}{m}$ and that the kinetic energy of the particle is $E = \frac{1}{2}mv^2$ (where v is the component of the particle velocity perpendicular to $\boldsymbol{B}$), the emitted power can be expressed as:

$$P = \frac{2}{3}\frac{q^4B^2v^2}{c^3m^2} = \frac{4}{3}\frac{q^4B^2}{c^3m^3}E \tag{3.8}$$

moreover when one considers that $\frac{dE}{dt} = -P$ and solves this differential equation obtains:

$$\frac{dE}{dt} = -\frac{4}{3}\frac{q^4B^2}{c^3m^3}E \quad \rightarrow \quad E(t) = E_0e^{-t/\tau} \quad \text{with} \quad \tau = \frac{3}{4}\frac{c^3m^3}{B^2q^4} \tag{3.9}$$

So the energy loss of the particle is exponential with a characteristic cyclotron cooling time of $\tau = \frac{3}{4}\frac{c^3m^3}{B^2q^4}$.
For electrons or positrons in a 1 T magnetic field, the characteristic time is ~ 2.5 s, so the cyclotron motion is an efficient cooling mechanism in magnetic fields of this order and for particles with small masses as the electrons. Due to the fact that the proton has a mass that is ~ 2000 times grater than the one of the electron, the cooling time for antiprotons is $\sim 10^{10}$ s so this process

is not sufficient for cooling the $\overline{p}$ fast enough. This is why, while catching antiprotons from the AD, the catching Trap is preloaded with a cloud of electrons that cyclotron-cool themselves in the Penning-Malmberg trap's 3 T magnetic field and then $\overline{p}$ are sympathetically cooled with electrons (as described in section 2.3). Cyclotron cooling of electrons and positrons is essential in the production of antiproton and positron plasmas at ALPHA.

Rotating Wall Compression

The ALPHA penning-Malmberg traps are made of a series of cylindrical electrodes and an external solenoid that provides a $\mathbf{B} = -B\hat{z}$ field parallel to the electrodes. Longitudinal confinement is obtained by applying potentials U_0 to the end electrodes, and radial confinement is obtained by the magnetic field, as explained previously. Considering a plasma of positive charges, these charges produce a radial electric field $\mathbf{E}$ pointing to the trap wall and this creates an azimuthal drift of the particles due to the $\mathbf{E} \times \mathbf{B}$, with velocity $v_\theta = E_r/B$ that following the calculations in [112] lead to a rotation frequency:

$$f_E = \frac{nq}{4\pi\epsilon_0 B} \tag{3.10}$$

where n denotes the plasma number density, q denotes the particles' charge, and B denotes the axial magnetic field. A plasma with uniform density so rotates like a rigid rotor, with all particles having the same rotational frequency out to the plasma's edge. A non-neutral plasma in a penning trap, that is an azimuthally symmetric system, is characterized by a conserved angular momentum L_θ:

$$L_\theta = \sum_j (m v_{\theta j} + q A_\theta r_j) \tag{3.11}$$

with $A_\theta = Br/2$ in a uniform magnetic field, the first term is the mechanical angular momentum and the second is the canonical angular momentum. For large magnetic field the canonical angular momentum term dominates and the total plasma angular momentum L_θ can then simply be approximated as:

$$L_\theta \simeq \sum_j q A_\theta r_j = \sum_j \frac{q B r_j^2}{2} \tag{3.12}$$

where r_j denotes the radial position of the j-th particle with respect to the rotation axis. As a result, a particle that drifts radially outward would cause other particles to move radially inward to conserve angular momentum. A plasma that rotates in an ideal Penning-Malmberg trap is constantly confined as long as the diameter of the confining electrodes is suitably large. Penning-Malmberg traps employed in the experiments are not

ideal. Magnetic field inhomogeneities, electrode defects, and particle collisions with background gas cause outward radial particle movement, resulting in a plasma expansion. This creates a torque against the plasma motion, resulting in a reduction of its rotation rate and therefore a decrease in its density and its angular momentum.
A torque that balances the drag can be used to compensate for the reduction of plasma angular momentum. In fact, by applying a torque greater than the drag, the plasma's angular momentum can be enhanced even higher. Because the rotational frequency of the plasma is related to its density (see equation 3.10), the increase in angular momentum results in a denser plasma than previously. As a result, a plasma can be compressed using this process, known as Rotating Wall Compression.

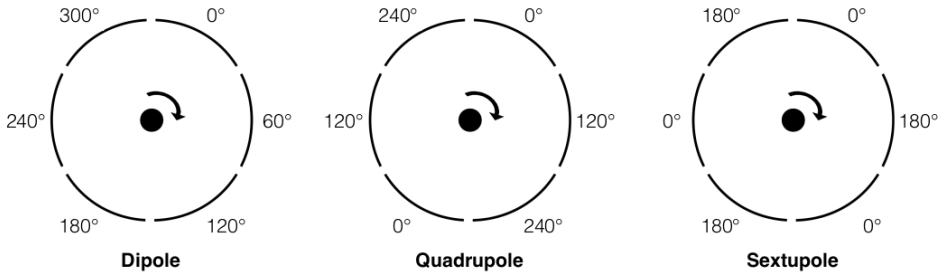

Figure 3.3: Schemes of rotating walls electrodes taken from [113]

In order to apply the torque needed one can apply a time-varying potential to an azimuthally sectored electrode, at frequencies f_{RW}. The potential $V_i(t)$ applied to each segment is given by:

$$V_i(t) = V_0 \sin[m(2\pi f_{RW} t - \theta_i)] \tag{3.13}$$

where $m = 1$ represents a dipole drive, $m = 2$ a quadrupole drive, $m = 3$ a sextupole drive. These potentials form a rotating electric field, which applies a torque and compresses the plasma. The rotation frequency of the plasma synchronizes with the applied rotating-wall frequency as long as the drive amplitude V_0 is sufficiently large. At ALPHA, rotating wall compression is an essential technique for obtaining plasmas suitable for the production of anti-hydrogen.

Evaporative cooling

The temperature of a particle ensemble is defined as the average of the ensemble's kinetic energy. When the most energetic particles are removed from the ensemble, the collection's average kinetic energy decreases, lowering the temperature. Evaporative cooling (EVC) is the technique of lowering overall temperature by selectively removing the most energetic particles. ALPHA

frequently uses the evaporative cooling approach to lower the plasma temperature during the creation of positron and antiproton plasmas for antihydrogen synthesis, as described in [114]. The particles are trapped in the Penning-Malmberg trap by a shallow potential well. The potential is then gradually reduced at one end of the well, allowing the most energetic particles to escape along the axis as shown in figure 3.4.

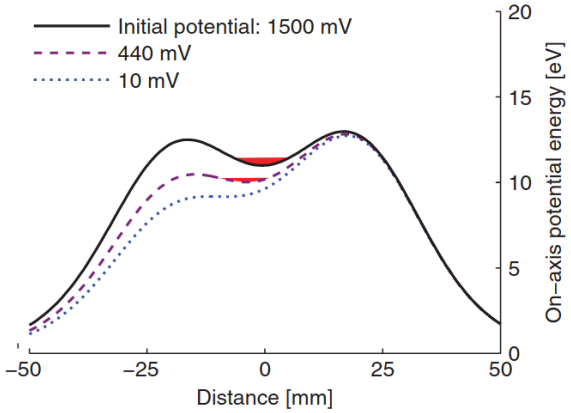

Figure 3.4: In this figure the potential wells utilized to keep antiprotons trapped during the evaporative cooling ramp are shown. The antiprotons are shown at the bottom of the potential well (red).

Because the particles escape in the axial direction, the remaining plasma's total angular momentum, whose expression is reported in equation 3.11 is conserved. As a result, a hole in the plasma is formed, which is filled by collisions between the nearby particles. As a result of the angular momentum conservation, other particles must move radially outward, resulting in a plasma expansion. This approach simultaneously reduces the particle density and space-charge of the plasma (forces generated directly by the charge distribution). This characteristic of evaporative cooling is used in the technique known as Strong-Drive-Regime-EVaporative-Cooling, or SDREVC described in the next section.

SDREVC

In steady state, a homogeneous charged particle plasma in a Penning - Malmberg trap rotates like a rigid rotor, as discussed previously. A solid cylinder with radius r_p, length l_p, and uniform charge $\rho = nq$ can be used to approximate the plasma shape. Moreover it is assumed that $k_b T \ll e\phi$ where ϕ is the potential difference over the radius of the plasma due to its own charge and e is the elementary charge. This is equivalent in the case of a cold plasma and with several Debye lengths in radius. In this case of infinitely-long (so $l_p \gg r_p$), zero-temperature plasma the on-axis self-potential ϕ_c is

given by [115]

$$\phi_p = \frac{nqr_p^2}{4\epsilon_0}\left[1 + 2\ln\left(\frac{R_w}{r_p}\right)\right] \tag{3.14}$$

where R_w is the radius of the electrodes of the Penning-Malmberg trap. The SDREVC approach involves compressing the non-neutral plasma with the rotating-wall in the Strong Drive Regime (SDR) while cooling it using evaporative cooling (EVC). It is based on the evidence that the rotating-wall frequency in equation 3.14 above fixes the plasma density n, while the shape of trap potential well and the final electrode potential during EVC fixes the plasma self-potential ϕ_p. The use of the two procedures would then determine the full set of final plasma parameters in a unique way. As a result, SDREVC can potentially produce plasmas of the appropriate number and density from a variety of different initial plasmas with different parameters. This makes the non-neutral plasma preparation in ALPHA controllable and reproducible.

Adiabatic cooling

The potential $U(z)$ in the confining well's center of a Penning-Malmberg trap can be approximated as an harmonic potential: $U(z) = \frac{1}{2}k_z z^2$. A charged particle in such a well feels an axial stabilizing force under this approximation $F_z = -k_z z = -m\omega_z^2$ where m is the particle's mass and ω_z is the axial oscillation frequency. The total energy of the particle along the z axis is $E_z = \frac{1}{2}mv_z^2 + \frac{1}{2}m\omega_z^2 z^2$.
For a certain energy E_z, the particle follows an elliptical orbit in phase space, the area of which is $2\pi\frac{E_z}{\omega_z}$. The area of the ellipse remains constant for slow changes in ω_z. As a result, the particle's energy to frequency of oscillation ratio, $\frac{E_z}{\omega_z}$ is an adiabatic invariant.
By gradually stretching the confining electrical potential well, ω_z can be decreased adiabatically. As a result, the particle's axial energy and temperature are lowered [116]. This is referred to as adiabatic cooling.
The preceding is a description of one-dimensional adiabatic cooling of a single particle. Because Coulomb interactions can be ignored in low density plasmas, the single-particle approximation is still valid. The temperature is linear with the plasma frequency $T \sim \omega_p$. On the other hand, collisions and space-charge effects must be taken into account at high densities. A rigorous theoretical three-dimensional treatment [117] predicts a scaling of $T \sim \omega_p^{4/3}$ in such a scenario. The ALPHA anti-hydrogen generation cycle includes adiabatic cooling of positrons.

Electron kicking

The capture and cooling of the antiproton beam from the AD necessitates the usage of a pre-loaded cloud of electrons, as described in section 2.3. So after $\overline{p}$ cooling, a plasma made of mixed antiprotons and electrons is confined in the potential well as a result. However, to make anti-hydrogen, the electrons must be removed from the trap before the antiprotons and positrons are mixed. If electrons are not eliminated, positrons may be lost due to electron-positron annihilations and the production of positronium. Furthermore, the electrons' space-charge can increase the positrons, resulting in a slower anti-hydrogen production and trapping rate.

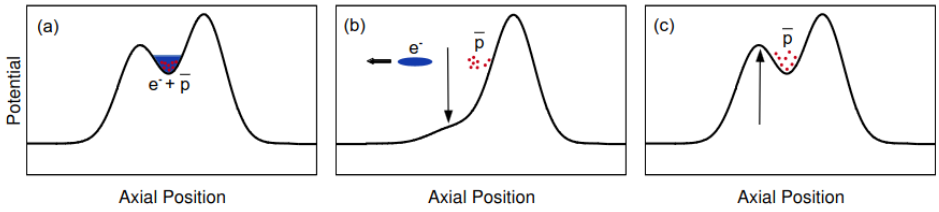

Figure 3.5: The figure shows a representation of the electrode potentials used for the "electron-kick" sequence. The panel (a) shows the electron-antiproton plasma. In the panel (b) one side of the confining well is removed, the electrons escape before the confining well is restored (in panel (c)), while the antiprotons remain trapped. The figure is taken from [113].

One of the procedures used for removing electrons from the antiproton-electron plasma uses the difference in mass between the two particle species. This procedure is called "electron-kick" and is shown in figure 3.5. First of all a fast voltage pulse lowers the trapping potential leaving the two species untrapped for a short time. During this time the electrons escape the trapping zone because they are lighter and have larger velocities with respect to antiprotons, which are still in the trap. Then the confining potential is restored fast enough (in ~ 100 ns) to not letting the antiprotons escape. In this way a pure antiproton plasma is obtained.
The heating of the antiproton plasma is a negative side effect of electron-kicking. The residual antiproton plasma heats rapidly as a result of the rapid application of the voltage pulse and the quick removal of the electron space-charge. To reduce this heating, a modified technique can be designed. By adjusting the amplitude of the electron-kick, one can remove a subset of the electrons rather than the whole electron cloud. The electrons remaining in the trap would then be cooled via cyclotron radiation, while the hot antiprotons are sympathetically cooled via Coulomb collisions with the electrons. The confining potentials are decreased once the mixed plasma re-cools to account for the reduced space-charge following the initial electron

elimination. Now, a much smaller electron-kick is required, resulting in a significantly lower level of plasma heating than previously. The electron-kicking process in ALPHA is separated into different stages, with the time and amplitude of each kick accurately tuned. The first electron-kick is set to keep $\sim 10^6$ electrons. This kick is followed immediately by a rotating-wall compression, which both compresses and increases the plasma temperature. Through cyclotron emission, the electrons help to re-cool the heated plasma and sympathetically cool the antiprotons. Once the plasma has cooled, two more electron-kicks are applied: the second one removes around 10^5 electrons, while the third removes all electrons. The end result is a dense plasma of pure antiprotons with no electrons in it and a low temperature.

3.2 Trapping of anti-hydrogen

Since anti-hydrogen ($\bar{H}$) is electrically neutral, it cannot be confined in Penning traps, but it can be confined via the interaction of its magnetic dipole moment $\boldsymbol{\mu}_{\bar{H}}$, generated by its angular momentum, with applied magnetic fields. A $\bar{H}$ atom in a magnetic field $\boldsymbol{B}$ has a potential energy given by

$$U = -\boldsymbol{\mu}_{\bar{H}} \cdot \boldsymbol{B} \tag{3.15}$$

where $\boldsymbol{\mu}_{\bar{H}}$ is the atomic magnetic dipole moment. In an inhomogeneous magnetic field, the $\bar{H}$ is subject to the force

$$\boldsymbol{F} = -\nabla U = \nabla(\boldsymbol{\mu}_{\bar{H}} \cdot \boldsymbol{B}) \tag{3.16}$$

a simplistic interpretation of equation 3.16 is that a magnetic field maximum is needed in order to generate a minimum in the potential, that is a trap. However, local maxima are forbidden by Maxwell's field equations [118], and magnetic trapping can only be obtained by establishing a magnetic field minimum. Equation 3.16 also demonstrates that the angle between the field and the dipole moment is critical to obtain a sufficient trapping force, therefore the magnetic moment's orientation with respect to the magnetic field must be kept the same while the atom moves in the trap [119]. This can be achieved if the magnetic moment of the $\bar{H}$ follow the magnetic field direction adiabatically, leaving the internal energy of the $\bar{H}$ system unaffected.
Because the magnetic moment does not depend explicitly on the spatial coordinates (but solely on internal quantum numbers), the gradient operator's argument can be written as

$$\boldsymbol{\mu}_{\bar{H}} \cdot \boldsymbol{B} = \mu_{\bar{H}}^{\parallel} B \tag{3.17}$$

where $\mu_{\bar{H}}^{\parallel}$ is the projection of the $\bar{H}$ magnetic moment on the magnetic field direction and B is the magnetic field magnitude. The combination of

equations 3.16 and 3.17 gives the trapping force:

$$\boldsymbol{F} = \mu_{\bar{H}}^{\parallel} \nabla B \tag{3.18}$$

The force in equation 3.18 can confine the $\bar{H}$ near the minimum of the potential of equation 3.15, if $\boldsymbol{\mu}_{\bar{H}}$ has a direction opposite to the one of the magnetic field $\boldsymbol{B}$ (if $\mu_{\bar{H}}^{\parallel} < 0$). The $\bar{H}$ that meet this requirement are called *low-field seeking*.

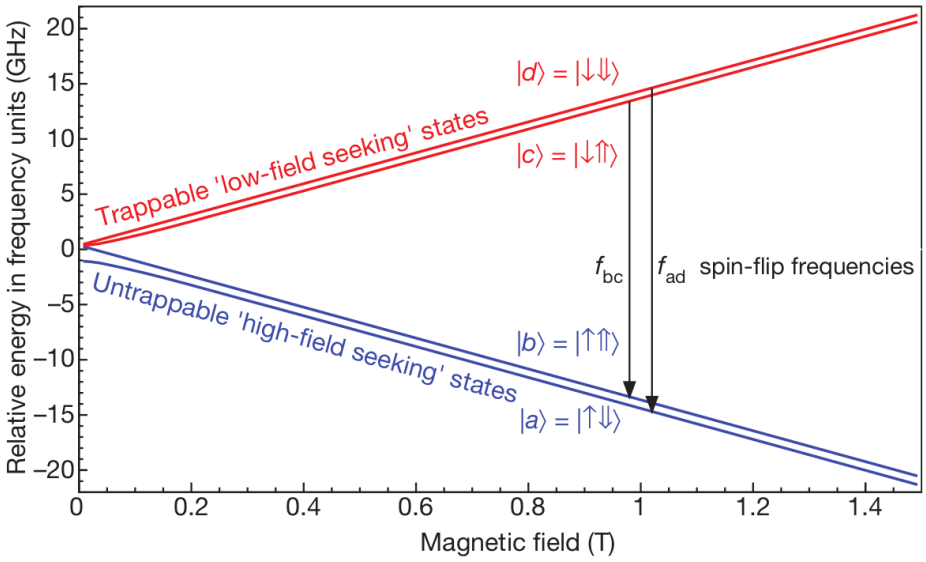

Figure 3.6: The magnetic field strength dependence of the hyperfine Zeeman sublevels of the $\bar{H}$ is shown in this Breit-Rabi diagram for $\bar{H}$ at the ground-state. The spin assignments for the four states are shown in the figure. Figure taken from [120].

The magnetic dipole moment of $\bar{H}$ is given by

$$\boldsymbol{\mu}_{\bar{H}} = \mu_B(g_l \boldsymbol{L} + g_s \boldsymbol{S}) + \mu_N g_p \boldsymbol{I} \tag{3.19}$$

where μ_B and μ_N are the Bohr and the nuclear magneton, respectively; $g_{l,s,p}$ are the gyromagnetic ratios; $\boldsymbol{L}$ is the e^+ orbital angular momentum, $\boldsymbol{S}$ is the e^+ spin, and $\boldsymbol{I}$ is the $\bar{p}$ spin.
Since $\mu_N/\mu_B \simeq 5 \times 10^{-4}$ the third term of equation 3.19 can be neglected. Moreover $L = 0$ for the $\bar{H}$ ground-state, and $g_s \simeq 2$, so equation 3.19 simplifies to

$$\mu_{\bar{H}}^{\parallel} = \pm \mu_B \tag{3.20}$$

where $\boldsymbol{S}$ is projected onto the direction of $\boldsymbol{B}$ leaving the $\pm 1/2$ term. The magnitude of the magnetic dipole moment of $\bar{H}$ is therefore $\mu_B \simeq 5.788 \times$

10^{-11} MeV T^{-1}. The positive sign of equation 3.20 describes the non-trappable high-field seeking states, while the negative sign describes the trappable low-field seeking, these states are represented in the diagram of figure 3.6. So, the low-field-seeking states for $\bar{H}$ are the ones that have the e^+ spin antiparallel to $\boldsymbol{B}$ (spin down).
In regions of the trap where B is close to zero, the separation between the trappable and non-trappable states is small (see figure 3.6), for this reason the probability that $\bar{H}$ undergoes a spin-flip ($|c\rangle \rightarrow |b\rangle$ or $|d\rangle \rightarrow |a\rangle$) is relevant. If this happens the $\bar{H}$ that was previously trapped, is then ejected from the trap. This can happen if $\bar{H}$ moves too quickly into these critical low-field regions and its magnetic dipole moment is unable to adiabatically follow the rapidly changing magnetic field direction, resulting in a misalignment between the atom magnetic moment and the magnetic field.
The ALPHA "neutral atom trap" is intended to avoid the spin-flip transition by introducing a magnetic field offset ($B \neq 0$) that is given by the solenoidal magnetic field used for the radial confinement of charged particles. The magnetic minimum trap for the axial confinement is created with two coaxial cylindrical coils, on either side of the trapping region. The radial confinement of the $\bar{H}$ is provided by an octupole magnet that generates a field, whose size is $|\boldsymbol{B}(r)| \propto r^3$ [121]. This magnetic trap arrangement is called Ioffe-Pritchard trap [96]. ALPHAg trap design will be elaborated in the next section.
Just cold $\bar{H}$ are confined via this magnetic trapping, since the typical depth of this trap is of the order of $\mu_B/k_b \simeq 0.67$ K/T. In ALPHA, the radial trap depth B_z is about 1 T, so the confined anti-hydrogen have energies of < 0.05 MeV (or < 0.5 K).

3.3 Anti-hydrogen production procedure

This section will focus on the steps performed for antiprotons and positrons preparation followed by the mixing of the two plasmas in the ALPHAg atom trap for the formation of anti-hydrogen.

3.3.1 Antiproton preparation

Antiprotons from the ELENA ring are captured in the CT 2.3, sympathetically cooled by preloaded electrons that were previously cooled by cyclotron radiation emission. After this step, SDREVC is applied and afterwards most of the electrons used for cooling are ejected via electron kicks, while $\sim 10^6$ of them are maintained. The combined electron-antiproton plasma is then radially compressed using the rotating wall to ensure an efficient transfer to the ALPHAg device. These plasma manipulation techniques are described in section 3.1.1. After the compression, the antiprotons are let to re-cool for ~ 10 s before the remaining electrons are ejected. When the CT is properly

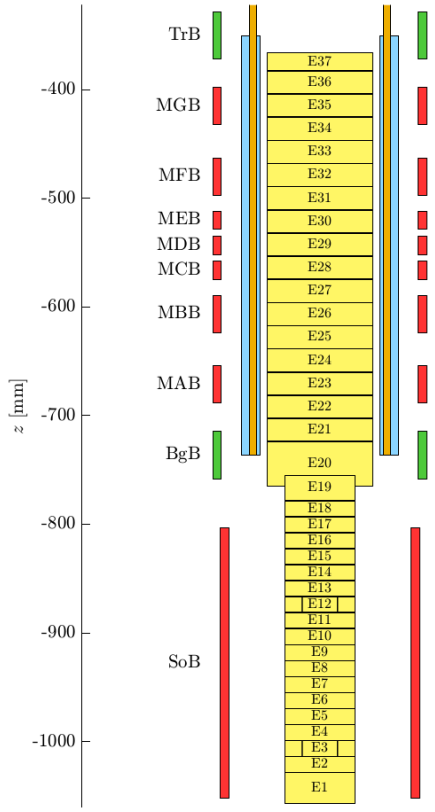

Figure 3.7: 2D representation of the magnets and electrodes of the ALPHAg bottom trap (from TrB to BgB) and of the region used for recatching $\bar{p}$ and $e+$ plasmas once they enter the ALPHAg apparatus (SoB region). Figure taken from [91].

optimised, this process gives a plasma of typically 1.1×10^5 antiprotons with a radius of 0.2 mm and a temperature of $\sim$ 400 K [122]. The antiprotons are then ejected from the CT by removing the confining potential in the trap. Antiprotons released from the CT travel ballistically, guided only by the static axial magnetic fields of the beamline, and enter the ALPHAg trap from below. When they arrive, they are manipulated in the same way that they were in the CT described above: the antiprotons enter the SoB region (figure 3.7) and are dynamically re-trapped; they are sympathetically cooled with electrons here, and the compression, cooling, electron ejection, and re-cooling procedures are repeated. The resulting plasma, after re-trapping, in 2022 had a radius of 0.4 mm and a temperature of $\sim$ 300 K.

3.3.2 Positron preparation

Positrons are prepared in parallel with the antiproton manipulations described above. Positrons are produced by a radioactive ^{22}Na source, which feeds a Surko-type buffer-gas accumulator 2.4. Plasmas containing between 10^6 and 10^8 positrons are created and transmitted to ALPHAg. A combination of EVC and SDR rotating wall compression is utilized to control the positron number and density. Positrons, entering the SoB region first (figure 3.7), are dynamically re-trapped after passing through the interconnect. They are cooled and compressed, before they are moved to a deep well under mirror B (MGB in figure 3.7). In this well, they wait until the antiprotons are loaded.

3.3.3 Plasma mixing

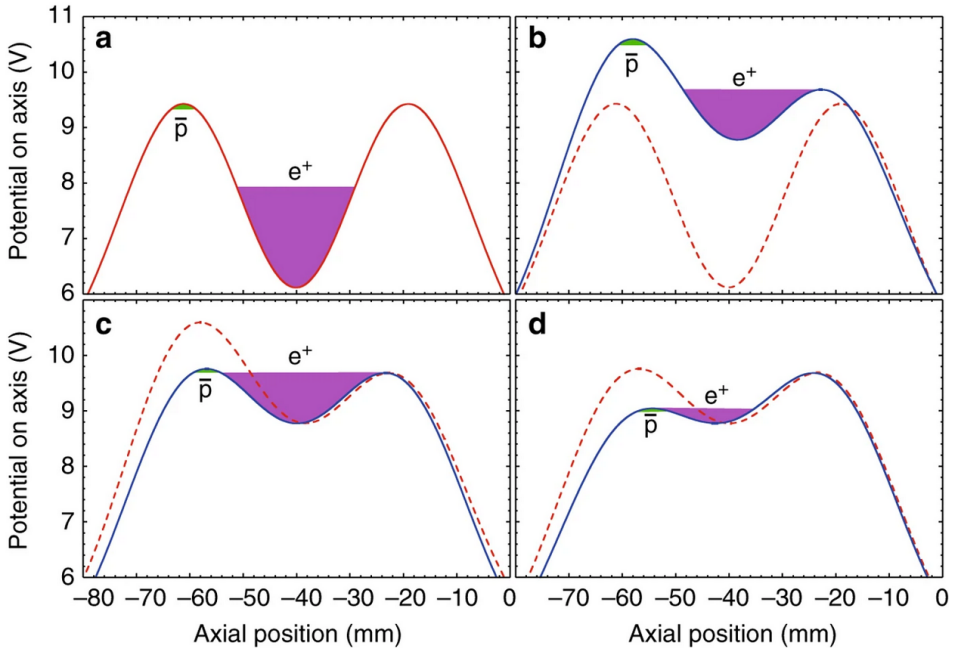

Figure 3.8: Example of mixing sequence taken from [122]. a) Potential prior to evaporative cooling. b) Evaporative cooling causes energetic positrons to escape to the right c) Potential realignment prior to mixing. d) Potential used for mixing. During mixing, positrons escape to the left, resulting in more evaporative cooling. The remaining positrons are expelled to the right to be measured, while the remaining antiprotons are thrown to the left.

The magnetic minimum trap is activated in order to perform the final preparation and mixing procedures. Antiprotons and positrons are transferred

between the electrodes E23 to E35 (figure 3.7). The positrons are evaporatively cooled after the adiabatic cooling stage (potential not indicated) by reducing the potential barrier on the right (figure 3.8 a), b)). The positrons begin to re-thermalise with their surroundings, and the potentials are quickly changed to the point where the antiprotons are on the edge of entering the positron plasma (figure 3.8 c)).
Finally, the antiprotons and positrons mixing happens by lowering the potential barrier between them; during this process, antiprotons can enter the positron plasma and positrons can drift to the left (figure 3.8 d)).
Anti-hydrogen is usually created via a three-body process in which one positron bonds to the antiproton and one positron removes the extra energy: $\bar{p} + e^+ + e^+ \rightarrow \bar{H} + e^+$. Releasing positrons from the trap during anti-hydrogen production has two advantages: during the merging process, the potential difference between antiprotons and positrons is minimized without accelerating the former, while the latter are continuously cooled via evaporation. This effect reduces the heating observed when positrons are maintained in a static well following evaporative cooling.
After the formation of anti-hydrogen atoms, only those atoms with kinetic energy below 0.5K can be trapped.

3.4 ALPHAg 2022 gravity experiment

The experimental protocol consisted in stacking anti-hydrogen atoms for 20 seconds before releasing them by ramping down the current in both mirror coils (A and G) simultaneously. The $\bar{H}$ escape either to the top of the trap (above mirror G) or the bottom (above mirror A) and then annihilate on the apparatus's walls. The ALPHAg radial time projection chamber (rTPC) is used to detect and track the $\pi^{\pm}$ produced by the $\bar{H}$ annihilation and reconstruct the annihilations position (called vertex). For the event selection, the Barrel Veto scintillator detector was also used.
Some numerical simulations of atom trajectories show that, in ALPHAg, if hydrogen atoms were trapped and released applying a symmetric field on mirror A and mirror G ($B_A = B_G$), roughly 80% of them would exit through the bottom of the trap and 20% of them through the top, with this asymmetry caused by gravity's force pointing downward. The ALPHAg experiment was designed to examine this behavior for anti-hydrogen. The influence of gravity can be favoured or contrasted via vertical gradients in the amplitude of the magnetic field. As previously indicated, the maxima in the axial field strength of the mirror coil are separated by 25.6 cm at full current, therefore a field difference of 4.53×10^{-4} T between the mirror A and G coils would have the same effect of the gravitational attraction between hydrogen and the earth in the centre of the trap.
Now one can consider a simplified a one-dimensional on-axis model in the

description of the experiment. Considering a specific $\bar{H}$ atom, as the mirror fields are gradually ramped down, it will escape the trapping field barriers when its axial kinetic energy is grater than the sum of the gravitational and magnetic potential at one of the mirror coils' maximal axial field position. Thus, the effect of gravity on matter can be balanced by imposing a field difference of around -4.53×10^{-4} T between the mirror A and G field peaks. If this difference is maintained during the ramp-down, half of the atoms will escape upwards and half downwards. This incremental field is quite modest in comparison to the size of the initial peak end field, which is approximately 1.74 T.
The mirror coils A and G are connected in series, and a bipolar current supply connected only to mirror G can provide a field increment or decrement. The magnetic gradient is not applied uniformly along the trap length and the axial escape of particles is determined by the local field geometry in the region of each mirror coil.

3.4.1 The measurement procedure

The octupole fields in ALPHAg, as previously stated, can be created by three unique coils. This measurement uses of two of them, the long octupole (LOc) and the short (or bottom) octupole (OcB). Both octupole magnets are charged to ~ 830 A for trapping and stacking. After stacking is complete, the LOc is ramped down in 1 s, removing partially the transverse confinement field above the bottom trap. This process liberates some of the more transversely energetic $\bar{H}$, accounting for around half of the stacked sample. The total number of atoms that have been stacked in the trap can be considered proportional to the number of annihilations produced by the LOc ramp-down. The experiment required numerous trials of anti-hydrogen accumulation and release at varying magnetic "bias" levels. The applied bias is defined as:

$$\frac{\mu_B(B_G - B_A)}{m_H(z_G - z_A)} \tag{3.21}$$

where μ_B denotes the Bohr magneton, $(B_G - B_A)$ is the difference between the on-axis field maxima under the two mirror coils, m_H denotes the hydrogen gravitational mass, and $(z_G - z_A = 256$ mm) denotes the height difference between the on-axis field maxima positions. Using expression 3.21 one can express the bias in terms of g in a convenient way. In the one-dimensional field model, a magnetic bias of 1g would balance hydrogen's downward gravitational force. The nominal bias values applied during the 2022 experiment are: $\pm$3g, $\pm$2g, $\pm$1.5g, $\pm$1g, $\pm$0.5g, and 0g while assuming no a priori direction or magnitude for the gravitational acceleration on $\bar{H}$. In the figure 3.9 are shown the field biases applied for the positive bias trials.

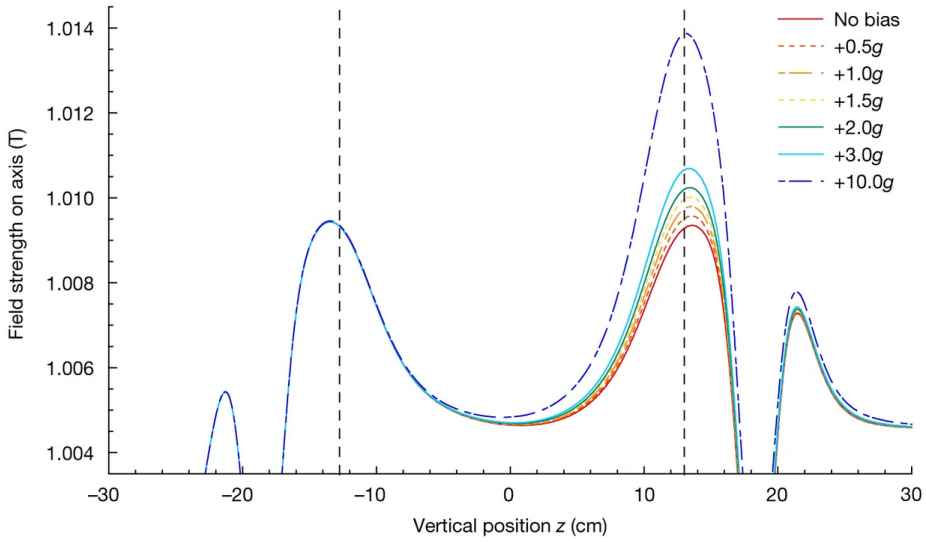

Figure 3.9: Nominal final on-axis well shapes (after ramp-down) for the positive bias trials. The OcB end turn windings are responsible for the features at $z < -20$cm and $z > 20$cm. The vertical dashed lines indicate mirrors A and G's axial midpoints.

For each trial the anti-atoms were accumulated for 50 stacks in around four hours, resulting in ~ 100 trapped atoms. After stacking and the LOc ramp-down, the on-axis field magnitude at one axial position under each mirror coil was measured using the electron cyclotron resonance (ECR) method [95]. The ECR measurement was taken 130 seconds after the LOc ramp-down. After this measurement the mirror coils are ramped down with a linear ramp lasting 20s. The smaller of the two mirror fields was not ramped down to the level of the bottom of the confinement well, but instead halted around 5×10^{-3} T above this level (this field is referred to as "porch field" in this thesis).
This was done to be sure that the atoms escaping from the trap had enough energy to overcome the axial field bumps caused by the OcB magnet's end windings (the residual fields at the plot's margins in figure3.9). The ECR measurements were repeated 96 seconds after the mirror ramp-down to measure the final axial well after the mirror A and G ramp-down. The different bias settings were interleaved during the 30-day data acquisition period. The bias values listed above are just labels used to identify the trials and refer to the nominal on-axis field maxima; nevertheless the bias is not perfectly constant during the ramp-down, and the one-dimensional model is simplistic to fully characterize the three-dimensional experiment.
Depending on the total number of events, the trials for a given bias were

repeated six or seven times. Figure 4.2 shows the raw z distributions of the reconstructed annihilation vertices for the different applied biases. In these distributions no background subtraction or detector efficiency correction was applied. The $\pm$10g trials are used to determine the rTPC detector's response, while the number of atoms observed during the LOc ramp-down is used to normalize the detector efficiency calculation (this will be treated in more detail in the chapter 4). Finally the effect of gravity on anti-hydrogen is manifested by the difference between the number of particles escaping upwards or downwards.

3.5 Simulation of the anti-hydrogen release

The simulation of the anti-hydrogen release dynamics ("the $\bar{H}$ simulation" in the following) is needed to obtain the relation between the asymmetry A of the upward- and downward-released $\bar{H}$ and the total potential difference at the mirrors (the total potential is the sum of the applied magnetic potential and the gravitational one). This can be done assuming different possible anti-hydrogen gravitational accelerations. The magnetic potential is known from the characterization measurements and the assumption that the anti-hydrogen magnetic moment is the same as the one of hydrogen [123]. In order to make this mapping between the total potential and the asymmetry A we need a simulation of the dynamics of anti-hydrogen. Further complications are related to the knowledge of the magnetic fields because the $\bar{H}$ dynamics takes place in a 3D trap while actually the field is characterized by means of 1D measurements along the axis. Moreover the magnetic field bias can vary during the $\bar{H}$ release. Due to these aspects one important element of the simulation is the modelling of the magnetic field. The other element of the simulation is the distribution of the $\bar{H}$ initial velocities.

The anti-hydrogen release simulation was done by Dr. Chuckman So. A detailed description can be found in [6], while a brief summary is reported here below. The simulation was developed assuming that CPT is conserved, even if this assumption has no effect on the final result at the experimental precision of the 2022 data acquisition.
The on-axis trap biases and the simulation of the three-dimensional trajectories of atoms in the trap were derived from a field model developed to include all knowledge of the magnetic trap during the MAGB ramp-down.
For the external solenoid, the design winding geometry was used to first calculate an ideal field, which was then compared to field measurements taken with NMR probes within the empty solenoid before the commissioning of the full experiment. To measure the current density perturbations on the solenoidal windings, the difference between the two was employed.
The external solenoid's field was then perturbed by the installation of the detector, the inner cryostat and octupole and mirror coils (the trapping

magnets). Based on the winding geometries that were measured during construction, the field contributions from the mirror coils and octupoles were calculated. Direct-Current Current-Transformers (DCCTs) were employed to measure the field model's MAGB currents. To measure the resulting field in situ with the fully commissioned apparatus, the ECR method [95] and a method based on the measurement of the frequency of the magnetron motion of the charged particles [124] are used. The results of these in situ measurement campaigns were then accounted for in the solenoidal current model.
After the field modelling, the $\bar{H}$ trajectories were simulated and evolved in time. The simulation of the trajectory was done in two steps:

1) Atoms were initialized close to the bottom of the trap to simulate the initial catching and accumulating process, uniformly distributed over a cylinder with a radius of 1 mm and a length of 5 mm. A 50 K Maxwellian distribution was used to extract the atoms initial velocity. The atoms were given a main quantum number of 30 and allowed to radiatively cascade down to the ground state. To imitate the slow accumulation of anti-hydrogen that is done during "stacking" in the gravity experiment, the time evolution of each atom was done for a randomly chosen time between 0 and 14400 s. After their available time had passed, the 6726 atoms that were still trapped were kept.

2) The time evolution of these retained atoms during the long octupole and the MAGB coils ramp-down, was performed using various trap biases and under various assumed gravitational accelerations.

The modelling of the magnetic field and the assumption on the $\bar{H}$ energy distribution is subject to uncertainties that will be taken into account in section 5.2.
Figure 3.10 shows the distributions of the z position and of the time of the $\bar{H}$ annihilations during the MAGB ramp-down for the simulations. Moreover it shows the behaviour of the release asymmetry as a function of the applied magnetic field bias for some examples of assumed gravitational acceleration ($a_g = -1$g, 0g, 1g). Due to its shape, we refer to the relation between A and bias as the S-curve.

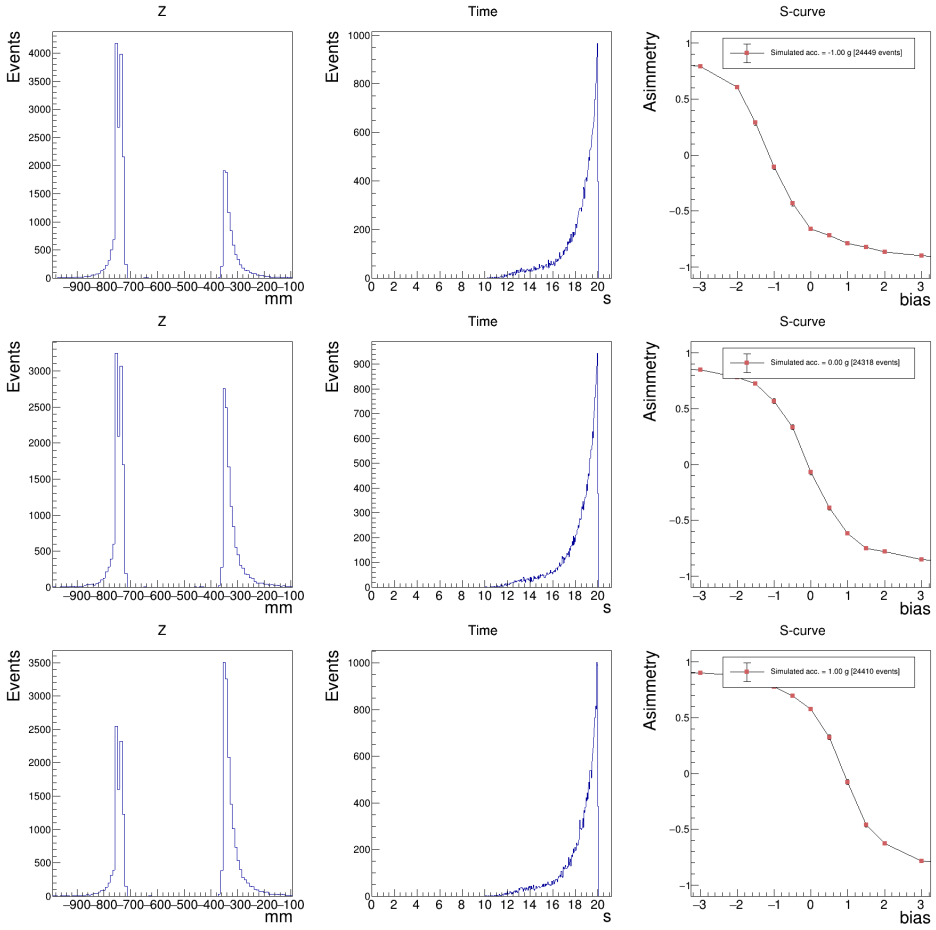

Figure 3.10: First, second and third rows show the plots of simulated events for $a_g = -1$g, 0g, 1g respectively. In these plots the detector resolution is not included. Left: distributions of the z position of the $\bar{H}$ annihilations vertices from simulation (including all the biases). Middle: time distributions of the $\bar{H}$ annihilations during the MAGB ramp-down. Right: asymmetry as a function of bias.

Chapter 4

Data analysis for the measurement of gravitational acceleration on anti-hydrogen

In this chapter the procedure followed for the data analysis for the measurement of the gravitational acceleration on anti-hydrogen is described.
The analysis is performed on the data collected by the ALPHAg experiment during the 2022 data acquisition. The data acquisition is performed by stacking the $\bar{H}$ atoms in the atom trap, applying different magnetic field biases to the $\bar{H}$ and releasing them during the MirrorA and G (MAGB) ramp-down. The escaping $\bar{H}$ atoms are released either upwards (in the MirrorG region) or downwards (MirrorA region) with respect to the center of the trap under the effect of the earth's gravitational acceleration combined with the applied magnetic field.
Anti-hydrogen annihilation candidates are reconstructed as vertices of two or more tracks in the detector. Background due to cosmic events is suppressed by a classifier based on topological and kinematic variables and trained to reject cosmic background. The annihilation candidates are also required to satisfy a set of selections in time and z-position.
In order to extract the a_g (gravitational acceleration for anti-hydrogen) parameter we perform a likelihood analysis on the MAGB data. First, the likelihood of the z positions of the annihilations detected during the MAGB ramp-down (for each bias) is built. The model for this likelihood contains the Probability Density Functions (PDF) for modelling the z distributions of the upwards and downwards released anti-atoms and of the cosmic background (the main source of background of this measurement), while the relevant parameter of this model is the asymmetry between the up (in the MirrorG region) and the down annihilation counts (in the MirrorA region).

The PDFs for modelling the z distributions of the upwards and downwards released anti-atoms are extracted assuming that for the data collected at "large" ($\pm 10g$) biases the $\bar{H}$ are purely downward or upward-released, respectively. The cosmic background rates and PDF are obtained from the data collected without any particles in the trap. Moreover, the efficiency asymmetry between the upper and the lower part of the experiment associated to detection and reconstruction is needed. This is calculated assuming that the ratio between the LOc counts and the MAGB release counts is constant. Afterwards, from the extracted asymmetries as a function of the applied biases, we build the total likelihood evaluated on the MAGB data with a_g as a parameter and perform a maximum likelihood analysis to extract this parameter. This regression is done using a simulation that associates to each gravitational acceleration value the expected upwards and downwards escaping anti-atom counts for each bias configuration. This simulation is available just for discrete values of the gravitational acceleration (a_g); Gaussian Process Regression (GPR) is used to interpolate the prediction of the asymmetries at each bias for the missing intermediate values of a_g.
This chapter, first of all, presents the data samples for the calibration of the model and for the g-measurement analysis, then it describes the tracks and vertex reconstruction and the selections applied to the data, the definition of the model for the analysis, and the regression for the extraction of the acceleration parameter.

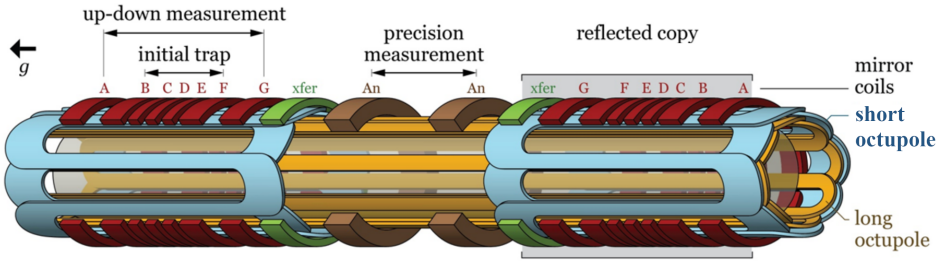

Figure 4.1: Scheme of the ALPHAg magnets. The scheme here is shown horizontally, but it is mounted vertically in the experiment as shown in figure 2.8. For the gravitational acceleration measurement of this thesis, just the bottom trap was used. The long octupole is used for the initial transverse confinement, the MirrorA and MirrorG are used for the axial confinement and the $\bar{H}$ release for the a_g measurement, while the short octuple for transverse confinement is kept powered during the MAGB release. For this reason the $\bar{H}$ escape is expected to be above and below the short octuple magnet.

4.1 Data sample

The analysed data samples consists in $\sim 1.5 \times 10^2$ detected $\bar{H}$ annihilation events during the MAGB ramp-down for each applied magnetic field value, and in about $\sim 2 \times 10^2$ detected $\bar{H}$ annihilation events during the LOc ramp-down collected during the 2022 data acquisition of the ALPHAg experiment. The different magnetic field configurations are denoted by bias configurations which correspond to the nominal value of the applied magnetic field difference in g units. $1g$ corresponds to a magnetic field difference of 4.53 Gauss (see equation 3.21). Each bias configuration required different trials of anti-hydrogen accumulation and release that form now on are called runs. The behaviour of the varying magnetic field in each of these configurations, that are associated to a bias configuration, is affected by uncertainties that will be treated as systematic uncertainties in sections 5.2.2 and 5.2.3.
The analysed data samples can be divided in three groups, according to the different ramp configurations and purposes:

- ± 10 g: the *calibration sample* collected with a fast MAGB ramp-down of 20 s with the ramp halting at the *porch* field.
- ± 3 g, ± 2 g, ± 1.5 g, ± 1 g, ± 0.5 g, 0 g: *physics sample*, with nominal release ramp (down to the "porch" field), fast (20 s) ramp.
- $-2s$ g, $-1s$ g, $0s$ g: *control sample*, with nominal release ramp (down to the "porch" field), slow (130 s) ramp.

The *calibration samples* are used to determine the detector response, while the *physics sample* runs are used for the determination of the up-down annihilation asymmetries (A^{raw}) for each bias. Figure 4.2 shows the raw event z-distributions for each of the bias values. On the top panel are shown the distributions of the fast ramp *physics samples* with the ± 10 g *calibration samples*, on the bottom panel are sown the distributions of the slow ramp *control samples*.
Moreover 2×10^3 events for each bias configuration generated by the anti-hydrogen release simulation were analysed for the comparison of the data with the expected behaviour of the $\bar{H}$ for different values of the gravitational acceleration, and the extraction of the a_g parameter. The simulation is available for the following values of gravitational acceleration a_g: -1.5 g, -1.25 g, -1 g, -0.75 g, -0.5 g, 0 g, 1 g, both for the fast ramp and the slow ramp. Here g denotes the absolute value of the nominal gravitational acceleration on the earth. The simulation for the slow ramp has a limited statistics of 10^3 events for most of the biases and g values.

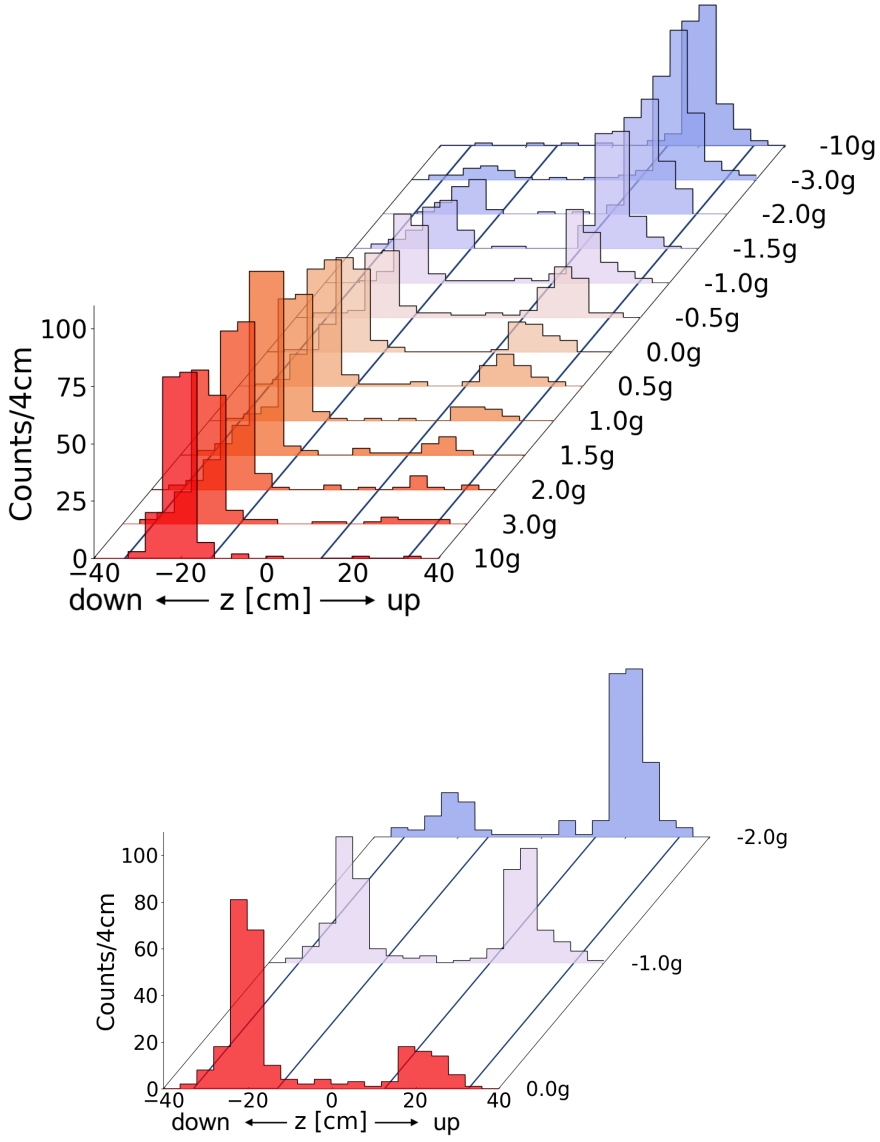

Figure 4.2: The raw event z-distributions are displayed as histograms for each of the bias values, including the ± 10 g *calibration samples*. On the top panel for the *fast ramp* data, on the bottom panel for the *slow ramp* data. These are uncorrected for background or detector relative efficiency. The time window represented here is 10 s to 20 s of the magnet ramp-down of the *fast ramp* data and 65 s to 130 s for the *slow ramp* data. The z-cut regions are indicated by the solid, diagonal lines. Explicitly, the acceptance regions in z are $[-32.805, -12.805]$ and $[12.805, 32.805]$ cm for the "down" and "up" regions, respectively. With this choice of coordinates the $z = 0$ cm position corresponds to the center of the bottom trap.

4.2 Tracks reconstruction and selection

In this section the selections applied to the data are presented. In particular it contains the description of the cuts applied for the cosmic background rejection, the selections on the reconstructed annihilation vertex z position, the studies performed for the choice of the time cuts on the MAGB and LOc ramp-down data and finally the criteria for the extraction of background enriched samples for cosmic background studies.

4.2.1 Background rejection

For the gravitational acceleration measurement, the successful annihilation vertex reconstruction in the rTPC, obtained combining at least a pair of tracks in the rTPC, is required. The vertex reconstruction algorithm was developed by Gareth Smith and Dr. Andrea Capra. The dominant background source of the gravitational acceleration measurement are cosmic rays. The background suppression is performed with a boosted decision tree (BDT) classifier developed by Lukas Golino and Dr. Joseph McKenna. The classifier is given as input twenty selection variables sensitive to the topological differences between annihilation events and background events and was trained using two control data-sets enriched on signal and background events. The signal control sample consists of anti-hydrogen produced during the mixing of antiprotons and positrons in the lower trap, where the high frequency of the events minimizes the contamination of cosmic background to negligible levels. The control sample of the background, on the other hand, consisted on events collected in the absence of antiprotons in the apparatus and therefore consists almost exclusively of cosmics. The most relevant variables for signal/background classification are the event sphericity, the cosine of the angle between the event axis and the detector axis, the variables associated to the multiplicity of hits in the event (number of Barrel Veto bar-ends triggered[1], number of bar-end clusters[2], number of rTPC pads triggered); see section 2.7.6 for more details on the detectors.
The separation between the signal and background events given by the classifier is shown in figure 4.3. The efficiencies obtained by scanning the cut value on the classifier output are shown in figure 4.4.
Finally, the cut value of 0.15 on the resulting classifier was chosen to optimize significance at 1 count of expected signal over a time interval of 8 seconds. The background rate depends slightly on z, this will be taken into account in the calibration procedure described in section 4.4.

[1]With bar-end we denote an ADC signal over threshold together with a TDC signal coming from by one end of a BV scintillator bar.

[2]With bar-end cluster we denote a set of adjacent bar-ends triggered.

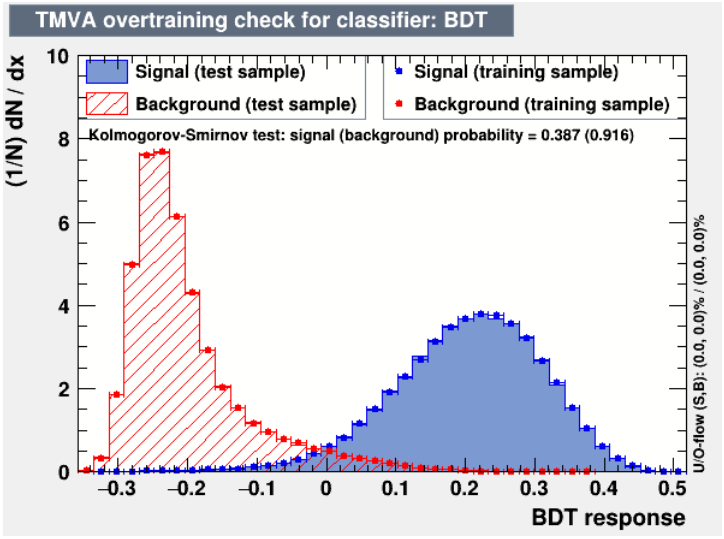

Figure 4.3: This figure shows the BDT response for the signal and background training samples. (Study performed by Lukas Golino).

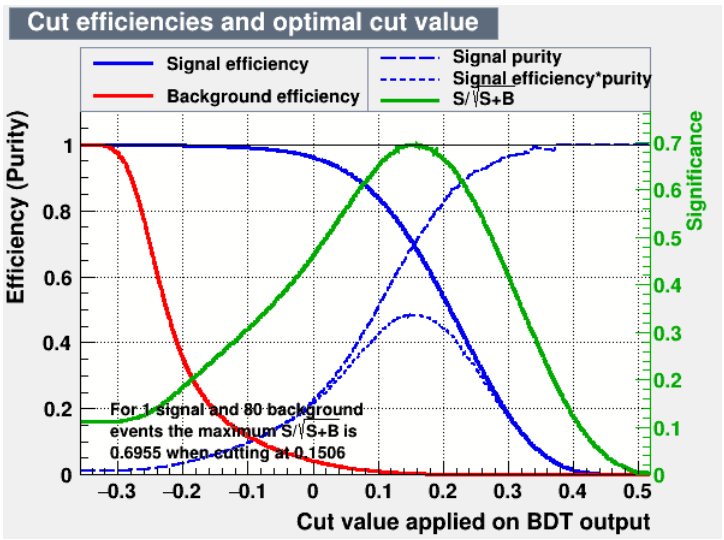

Figure 4.4: This figure shows the efficiency dependece on the BDT output cut value. Note that the $S/\sqrt{S+B}$ is not much reliable when $S \to 0$. (Study performed by Lukas Golino).

4.2.2 Vertex position (z) selection

The analysis is performed after having applied a selection on the vertex position z data. The z range was divided in 2 acceptance regions: the axial position z of the vertex is required to be in the $[-32.805, -12.805] \cup [12.805, 32.805]$ cm. These two regions are located at the edge of the short octupole coil – the first one just below the Mirror A position and the second one just above the Mirror G position – and are chosen to be centered around the lower trap magnet system (with center located at 0 cm). This is where most of the $\bar{H}$ annihilations are expected to happen when ramping down Mirror A and Mirror G. The z selection for the LOc ramp-down samples is instead chosen to be a single region: $z \in [-32.805, 32.805]$ cm. The chosen z selections are reported in table 4.1.

Sample	z **ranges**
MAGB ramps	$[-32.805, -12.805] \cup [12.805, 32.805]$ cm
LOc	$[-32.805, 32.805]$ cm

Table 4.1: Chosen z range selections.

The magnets are shown in figure 4.1 while the bottom trap electrodes and the axial field profile at full current is shown in figure 2.8. Figure 4.2 shows the z distributions obtained for the fast ramp and the slow ramp data. Table 4.3 gives the number of events occurred in each acceptance region (N_{up} and N_{dn}) during the MAGB ramp down. Moreover it gives the number of events occurred during the LOc ramp down (considering both regions). The numbers in table 4.3 are background subtracted for the expected cosmic rate in each region.

4.2.3 Vertex time (t) selection studies

In order to choose properly the time selections to be applied in the MAGB and LOc ramps, some studies were performed in order to understand at which time during the ramp the number of events detected is no more compatible with the cosmic background.
The LOc ramp-down happens in a $\sim$ 7s time window before the ECR measurement and the MAGB ramp-down. There is a $\sim$ 160 s wait between the end of the LOc ramp-down and the beginning of the MAGB ramp-down. The vertex time distributions during LOc ramp-down (for the 10 g, fast ramp and slow ramp) are shown in figure 4.5. There is a negligible amount of events beyond 13.1 s from the start of the LOc ramp-down.
The MAGB fast ramp-down happens in a 20 s time window from the starting magnetic field to the "porch" magnetic field that is the final value of the field reached during the MAGB ramp-down. The MAGB slow ramp-down happens in a 130 s time window from the starting magnetic field to the

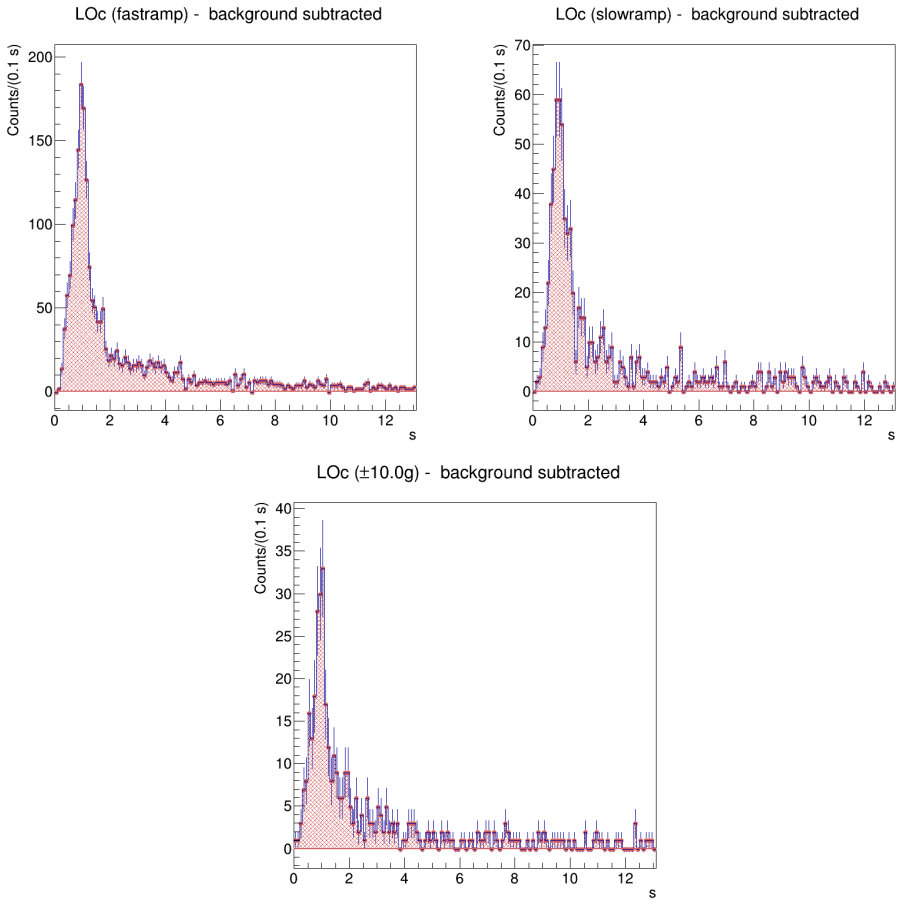

Figure 4.5: Vertex time distributions during LOc ramp-down for the fast ramp (top left), slow ramp (top right), 10 g (bottom).

"porch" magnetic field. The vertex time distribution during the MAGB ramp-down for the 10 g (*calibration samples*) is shown in figure 4.6, while the same distributions for the *physics sample* fast ramp and slow ramp are shown in figure 4.7. The latter shows also the integrals from start and from the end of the time window in order to understand where the vertices given by the escaping $\bar{H}$ enhance the events rate above the cosmic background. As one can notice from figure 4.7 the "integral from end" remains quite constant before 10 s for the fast ramp, and before 65 s for the slow ramp corresponding in both cases to the 50% of the whole ramp-down time window. This means that there is a negligible fraction of $\bar{H}$ escaping the trap before these times.

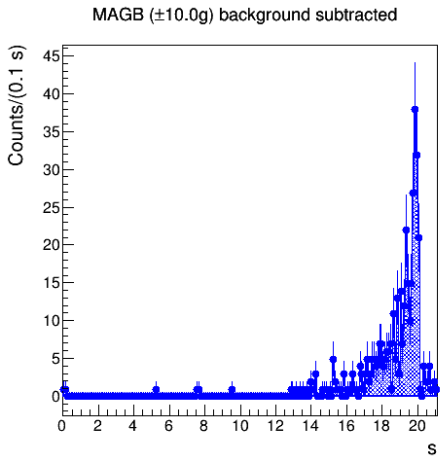

Figure 4.6: Vertex time distribution during MAGB ramp-down for the 10 g sample.

Chosen vertex time selections

The selection cuts of $t \in [10.00, 20.00]$ s are chosen according to the nominal ± 10 g and fast ramps and the selection cut of $t \in [65.00, 130.00]$ s for the slow ramp is chosen. These selections retain the annihilations occurring after the nominal ramp has progressed to the "porch" value. As a cross-check also annihilations occurring up 1.1 s after the "porch" can be used.

For the LOc ramp the time (t) window is tightened to $t \in [0.00, 13.10]$ s in which the escape of $\bar{H}$ is present.
The chosen time ranges relative to the start of the LOc ramp are summarised in table 4.2.

Sample	**Time ranges**
MAGB ± 10 g and fast ramp	$[10.00, 20.00]$ s
MAGB slow ramp	$[65.00, 130.00]$ s
LOc	$[0.00, 13.10]$ s

Table 4.2: Chosen time range selections.

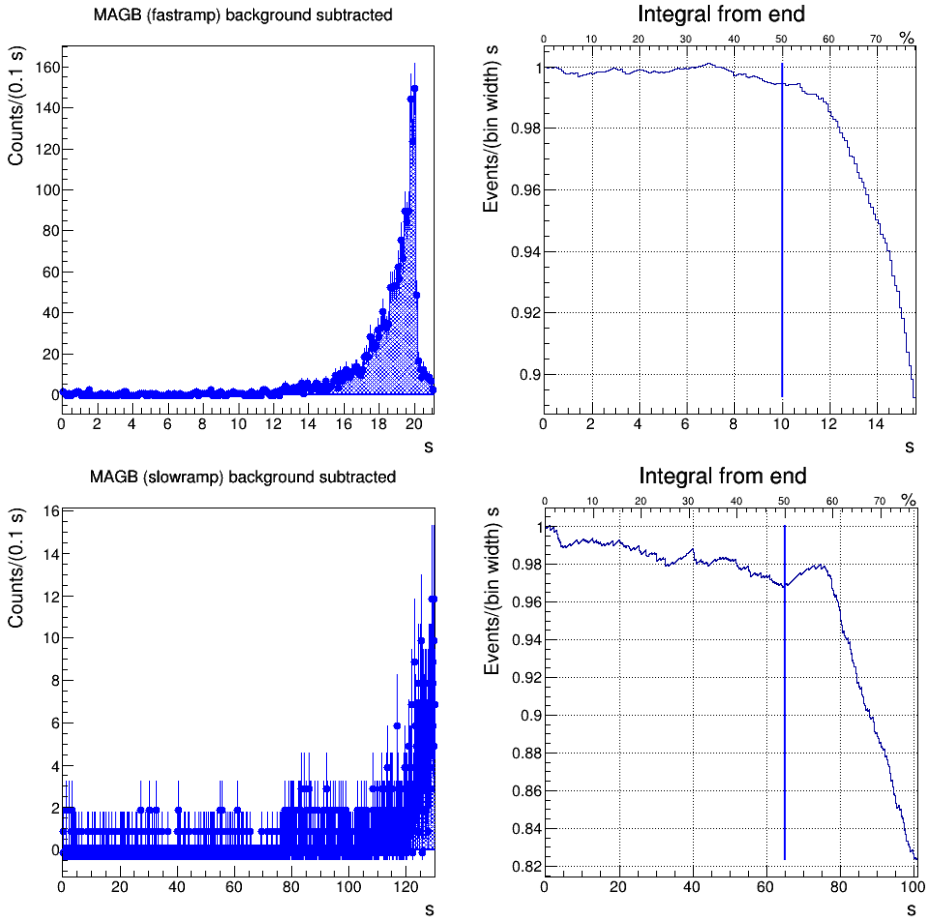

Figure 4.7: Vertex time distributions during MAGB ramp-down for fast ramp (top row) and slow ramp (bottom row). The left plots, for each row, are the raw time distributions. The right plots are the integral from the end of the time window to check for changes in slope. The slow ramp (bottom) plots of the "integral from end" are zoomed in the region $t \in [0, 100]$ s in order to highlight their change in slope. The vertical lines indicate the limit chosen for the selection of the events to be analyzed.

Bias (g)	Number of runs	N_{up} (MAGB)	N_{dn} (MAGB)	LOc events
-3.0	7	151.7	16.5	199.2
-2.0	7	128.7	33.5	168.2
-1.5	6	128.9	57.7	192.0
-1.0	7	69.7	62.5	183.2
-0.5	7	55.7	67.5	201.2
0	7	36.7	94.5	144.2
0.5	7	36.7	124.5	177.2
1.0	7	17.7	119.5	185.2
1.5	6	13.9	180.7	234.0
2.0	7	6.7	163.5	228.2
3.0	7	7.7	147.5	199.2
-10.0	6	142.9	0.7	169.0
10.0	6	-0.1	185.7	213.0

Table 4.3: For each bias configuration, the number of events for anti-atoms escaping upwards or downwards is listed. These events are selected in a time window between 10 and 20 s during the MAGB ramp-down and in the z-regions shown in figure 4.2. The number of anti-hydrogen annihilation events during the LOc ramp down is also indicated. These numbers have been adjusted to account for the expected cosmic ray background. The background per run was 0.18 ± 0.01 events in the top region and 0.21 ± 0.01 events in the bottom region. The background per run for the LOc ramp-down window (duration 13.1 s) was 0.83 ± 0.02 events. The uncertainties in counting are not indicated. The counts for the ± 10 g runs are also listed. This table is also presented in [6].

4.3 Model definition

This section contains the definition of the models for constructing the likelihoods for the analysis of the MAGB and LOc data samples.
The probability density function for an event e to be detected at the position z_e, in the bias configuration i for the MAGB ramp-down samples, is:

$$\mathcal{P}_i(z_e) = \frac{N_{d,i} f_d(z_e) + N_{u,i} f_u(z_e) + B_i f_b(z_e)}{N_{d,i} + N_{u,i} + B_i}$$

with $N_{u,i} = \frac{1}{2} S_i (1 + A_i^{raw})$ and $N_{d,i} = \frac{1}{2} S_i (1 - A_i^{raw})$, where $S_i = N_{u,i} + N_{d,i}$ is the total anti-hydrogen yield, $N_{u,i}$ and $N_{d,i}$ are the yields for the upwards released anti-atoms ($\bar{H}_u$) and the downwards released anti-atoms ($\bar{H}_d$), respectively, $A_i^{raw} = (N_{u,i} - N_{d,i})/S_i$ is their asymmetry, B_i is the expected background yield, f_u, f_d, and f_b are the probability density functions in z for $\bar{H}_u$, $\bar{H}_d$, and background, respectively.
From this, one can build the extended likelihood for the MAGB release ramp annihilations in a given bias configuration

$$\mathcal{L}_i(\mathbf{Z}_i | A_i^{raw}, S_i) \propto e^{-(S_i + B_i)} \prod_{z_e \in \mathbf{Z}_i} \big[\frac{1}{2} S_i (1 - A_i^{raw}) f_d(z_e) + \\ + \frac{1}{2} S_i (1 + A_i^{raw}) f_u(z_e) + B_i f_b(z_e) \big] \quad (4.1)$$

The extended likelihood for the long-octupole ramp events is

$$\mathcal{L}_{i,o} \propto e^{-(S_{i,o} + B_{i,o})} (S_{i,o} + B_{i,o})^{N_{i,o}} \quad (4.2)$$

where $S_{i,o}$, $B_{i,o}$ are the parameters for the number of signal events and cosmic background events during the LOc ramp-down for the bias i, respectively; $N_{i,o}$ is the number counts recorded during the LOc ramp-down for the bias i. A detailed derivation of the parameterization of these likelihoods is presented in the appendix A.
Note that this model is cast in terms of the raw asymmetry A^{raw}. As it will be shown in 4.5 these A^{raw} needs to be corrected for the detection reconstruction efficiency D_i in order to extract the release asymmetry A_i which is determined by the total confinement potential which includes the contributions of both the magnetic fields and the gravitational field (see section 3.4). The formula that relates A_i to A_i^{raw} is:

$$A_i^{raw} = \frac{A_i - D_i}{1 - D_i A_i} \quad (4.3)$$

Roughly speaking, the release asymmetry A_i is used to determine the total potential (due to magnetic field and gravitational field) difference between the Mirror A and G saddle points, so that, knowing the magnetic potential

from the ancillary measurements, one can derive the gravitational potential through the simulations.
The calibration of this model, used to extract the PDF shapes and the values of D_i and K_i, is presented in the next section (4.4).

4.4 Calibration of the model

The calibration of the model presented in section 4.3 is performed on the ±10g *calibration samples*, on the MAGB data, and on the cosmic background enriched samples. This allows the extraction of the z probability distribution functions and the cosmic background rate. The comparison between the counts observed during the MAGB ramp-down to the counts observed during the LOc ramp-down allows the extraction of the efficiency asymmetry parameter.

4.4.1 Signal and background models

The signal and background models are extracted directly from the *calibration samples* ±10 g and cosmic data, rather than imposing an analytical model. In particular the background PDF (f_b) is obtained from the background-enriched samples, after selection. On the other hand the z PDF shapes (f_u, f_d) of equation 4.1 are derived from calibration data by making an assumption on the relative mixture of up-wards and down-wards released anti-atoms – i.e., on the purity – in the *calibration samples*. For the $\pm 10g$ MAGB data the assumption is that these samples are composed of purely up-wards and purely down-wards released $\bar{H}$, respectively.

Background rate and yields

The background z-distributions and yields (f_b and B_i) are constrained from data collected without antiprotons in the experiment. In particular the background rate r and the background PDF f_b are calculated from the background-enriched samples. These samples are obtained selecting the time intervals at the beginning of each data taking run, in which there are no antiprotons in the experiment and the detected events are mostly due to cosmic rays hitting the detector.
The background rate r in the acceptance region presented in section 4.2 is obtained dividing the total number of counts after selection by the total exposure time ($T = 39666.6\,\mathrm{s}$):

$$r^{LOc} = (0.0650 \pm 0.0013)\,\mathrm{Hz}, \quad r^{MAGB} = (0.0403 \pm 0.0010)\,\mathrm{Hz}.$$

The cosmic rate is different in the LOc and the MAGB samples because the applied z selections are different (see section 4.2.2). The rate is not uniform over z, and this is taken into account in the likelihood by the PDF

shape $f_b(z_e)$. The $f_b(z_e)$ PDF shape is obtained from the z distribution of the background-enriched samples. There is no significant variations of the background rate over the data-taking periods, so the average rate is used in the analysis. The expected background $B_{i,(o)}$ at each bias is therefore calculated as $B_{i,(o)} = r \times N_i^{runs} \times T_{i,(o)}$, where $T_{i,(o)}$ is the length of the selection window for MAGB or LOc data in bias configuration i, and N_i^{runs} is the number of runs. Both N_i^{runs} and $T_{i,(o)}^{runs}$ vary with i (the latter according to table 4.2).

Signal PDFs extraction for upwards and downwards released $\bar{H}$

The (binned) probability distributions in z of the $\bar{H}_u$ and $\bar{H}_d$ annihilations during the MAGB ramps (f_u and f_d) are determined from the MAGB data in *calibration samples* at large biases ($\pm 10g$ samples), in which the signal is assumed to consist almost entirely of $\bar{H}_u$ or $\bar{H}_d$.
In order to obtain the probability distribution functions for the upwards escaping $\bar{H}$ and the downwards escaping $\bar{H}$ (f_u, f_d) presented in section 4.3, the negative log-likelihood $-\log \mathcal{L}_{\pm 10g,MAGB}$ was minimized with respect to the PDF value in each bin. Here $\mathcal{L}_{i,MAGB}$ is the likelihood presented in equation 4.1, where the background yields B_i and the background PDF shape $f_b(z_e)$ are fixed to the values obtained from the background-enriched samples (as described in the previous section), and the value of the asymmetries in the two configurations is fixed according to the following assumption: $A^{raw} = +1$ for the $-10\,g$ sample and $A^{raw} = -1$ for the $+10\,g$ sample. With these assumptions the negative log-likelihood of the $+10g$ samples depends just on a normalization factor S_i and on the parameters defining the weight of each bin of the $f_d(z_e)$ PDF. Likewise the negative log likelihood for the $-10g$ samples depends just on S_i and the parameters of the $f_u(z_e)$. The plots of the obtained PDFs are shown in figure 4.8.

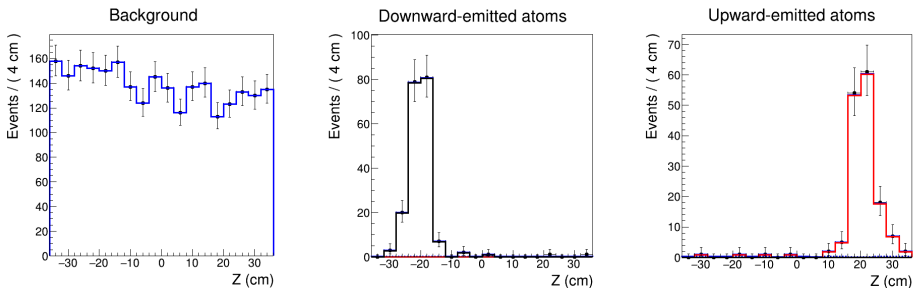

Figure 4.8: Distributions for the background (blue), the downward-escaping anti-atoms (black) and the upward-escaping anti-atoms (red), assuming a pure sample ($A^{raw} = \pm 1.00$). Dots with error bars are the data, the solid lines are a fit to the data. From these distributions the (binned) PDFs $f_b(z)$, $f_u(z)$, $f_d(z)$ for the binning choice descried in section 4.2.2 are derived.

4.4.2 Extraction of the efficiency asymmetry from long- octupole data

The number of counts observed during the LOc ramp-down is assumed to be proportional to the total number of $\bar{H}$s present in the trap immediately before the start of the MAGB ramp-down, independently of the magnetic bias. The detection efficiency asymmetry can then be determined as follows. The $\bar{H}$ counts $S_{i,o}$ during the LOc ramps are proportional to the efficiency-corrected yields in the MAGB ramp:

$$\frac{S_{i,o}}{S_i} = \kappa_i(1 + D_i A_i^{raw}), \tag{4.4}$$

where the rightmost factor is a correction for the asymmetry D_i of the detection efficiency [3] and $\kappa_i = [K_i(1 - D_i^2)]^{-1}$. The proportionality factor K_i is assumed to be independent of the bias configuration, whenever the experimental conditions in each bias configuration can be considered similar, e.g., the proportionality factor K_i is assumed to be the same for data samples acquired close in time. The detection efficiency is also considered independent of the bias, assuming the same event selection is always applied, whenever the detector conditions can be considered stable and the underlying signal distributions equal between the different configurations.
The assumption of the proportionality between the LOc counts and the MAGB counts as shown in equation 4.4, is equivalent to imposing a linear model $y = mx + q$ for the data, where $y = S_{i,o}/S_i$ and $x = A_i^{raw}$ (here, we note that x and y are uncorrelated). The detection asymmetry D is then given by the ratio m/q of the parameters of the linear model (as $q \equiv \kappa_i$ and $m \equiv \kappa_i D_i$ in equation 4.4). The procedure for extracting the efficiency asymmetry therefore requires, at a minimum, data collected at two different biases and the asymmetry for the two points must be different, in order to determine the slope m.
The ratios of the number of LOc counts and the number of MAGB counts as a function of the corresponding A^{raw} values for each experimental configuration are shown in figure 4.9. The slope m is extracted using a method called Orthogonal Distance Regression (ODR Python library [4]) of $y = S_{i,o}/S_i$ as a function of $x = A_i^{raw}$.
The extracted values of the efficiency asymmetries for different collection of datasets are shown in table 4.4. The procedure has been validated using repeated pseudo-experiments on simulated data. For the fit to the fast ramp *physics sample* the value of D is determined from the *calibration sample* and the slow ramp *physics sample*. Vice-versa for the fit to the slow ramp *physics sample*.

[3] Being η_u and η_d the efficiencies in detecting respectively *up* and *down* annihilations, D is defined as $\frac{\eta_d - \eta_u}{\eta_u + \eta_d}$.

[4] `https://docs.scipy.org/doc/scipy/reference/odr.html`

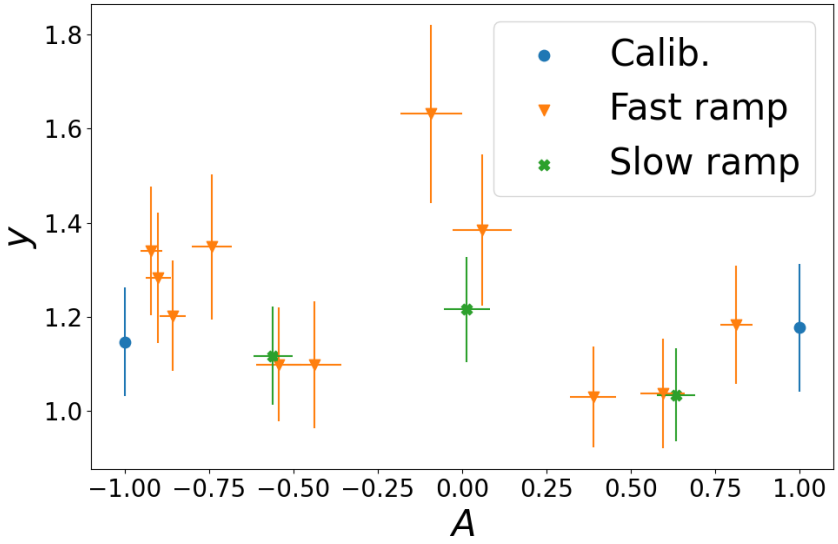

Figure 4.9: This plot shows the ratio between the number of LOc counts and the number of MAGB counts ($y = S_{i,o}/S_i$) as a function of the corresponding A^{raw} values, for different bias configurations. This is used as input of the Orthogonal Distance Regression for the extraction of the efficiency asymmetry parameter D.

Data	D
Calib. only	$+0.01 \pm 0.08$
Calib. and slow ramp	-0.03 ± 0.06
Calib. and fast ramp	-0.05 ± 0.04

Table 4.4: Dependence of the value of the estimated efficiency correction D from the different data samples.

4.5 Regression of the acceleration parameter

Having determined the cosmic background PDFs and rate and the signal PDFs for annihilations of upward- and downward-released anti-hydrogen, from the likelihood 4.1 that is also reported here:

$$\mathcal{L}_i(\mathbf{Z}_i|A_i^{raw}, S_i) \propto e^{-(S_i+B_i)} \prod_{z_e \in \mathbf{Z}_i} \Big[\frac{1}{2} S_i(1 - A_i^{raw}) f_d(z_e) + \\ + \frac{1}{2} S_i(1 + A_i^{raw}) f_u(z_e) + B_i f_b(z_e)\Big]$$

it is possible to readily determine the maximum likelihood estimator of the

raw signal asymmetries A_i^{raw}. Note that, since data has been collected independently in each bias configuration, the raw asymmetries are uncorrelated when the PDFs and the background rate are fixed. Small correlations – from using the same PDF models and background rates for all biases – arise and are accounted for when evaluating systematic uncertainties.
However, we are primarily interested in determining the acceleration a_g of anti-hydrogen due to the gravitational field of the Earth. To do so we rely on the anti-hydrogen release simulations described in section 3.5 to derive the expected relation ("S-curve") $f(x_i, a_g)$ between the nominal on-axis magnetic field bias x_i and the release asymmetry $A_i^{sim}(a_g)$ in each configuration i. Due to the computational burden, the simulation is run only for the discrete values of the bias x_i for which experimental data were collected, and only for a finite number of gravitational accelerations a_g. For each bias i, the expected $A_i^{sim}(a_g)$ corresponding to intermediate a_g values are obtained from a Gaussian Process Regression (GPR Python library [5] [125]) that uses the existing simulation points as input (figure 4.10).
The expected value of the raw asymmetry associated to each release asymmetry $A_i^{sim}(a_g)$ is then calculated by correcting $A_i^{sim}(a_g)$ for the detector efficiency asymmetry D.

$$A_i^{raw}(a_g, D) = \frac{A_i^{sim}(a_g) - D}{1 - A_i^{sim}(a_g)D} = \frac{f(x_i, a_g) - D}{1 - f(x_i, a_g)D} \tag{4.5}$$

It is then possible to recast 4.1 in terms of $A^{raw}(a_g, D)$ and write the total likelihood:

$$\mathcal{L}(\mathbf{Z}|a_g, D, \mathbf{S}) = \prod_i \mathcal{L}_i[\mathbf{Z}_i|A_i^{raw}(a_g, D), \mathbf{S}] = \prod_i \mathcal{L}_i[\mathbf{Z}_i|f(x_i, a_g), D, \mathbf{S}]. \tag{4.6}$$

Equation 4.6 then shows that the uncertainty on D cannot be neglected in the determination of a_g. Instead of fixing D to the best value determined from calibration, we let it vary in the fit and incorporate the calibration information by multiplying $\mathcal{L}$ by a Gaussian-constraint term on D:

$$\mathcal{L}' = \mathcal{L} \cdot \frac{1}{\sqrt{2\pi\sigma_D^2}} \exp\left\{-\frac{(D - \mu_D)^2}{2\sigma_D^2}\right\}. \tag{4.7}$$

Where μ_D is the value of D estimated as described in section 4.4.2, σ_D is obtained by summing in quadrature the statistical uncertainty on D with its systematic uncertainty, quantified to be 0.02 (see section 5.1.3). We then minimize the negative logarithm of $\mathcal{L}'$, NLL $= -\log(\mathcal{L}')$, to obtain an estimate of a_g from the fast-ramp data, the uncertainty is obtained from the confidence interval corresponding to min(NLL) + 1/2:

[5] `https://scikit-learn.org/stable/modules/gaussian_process.html`

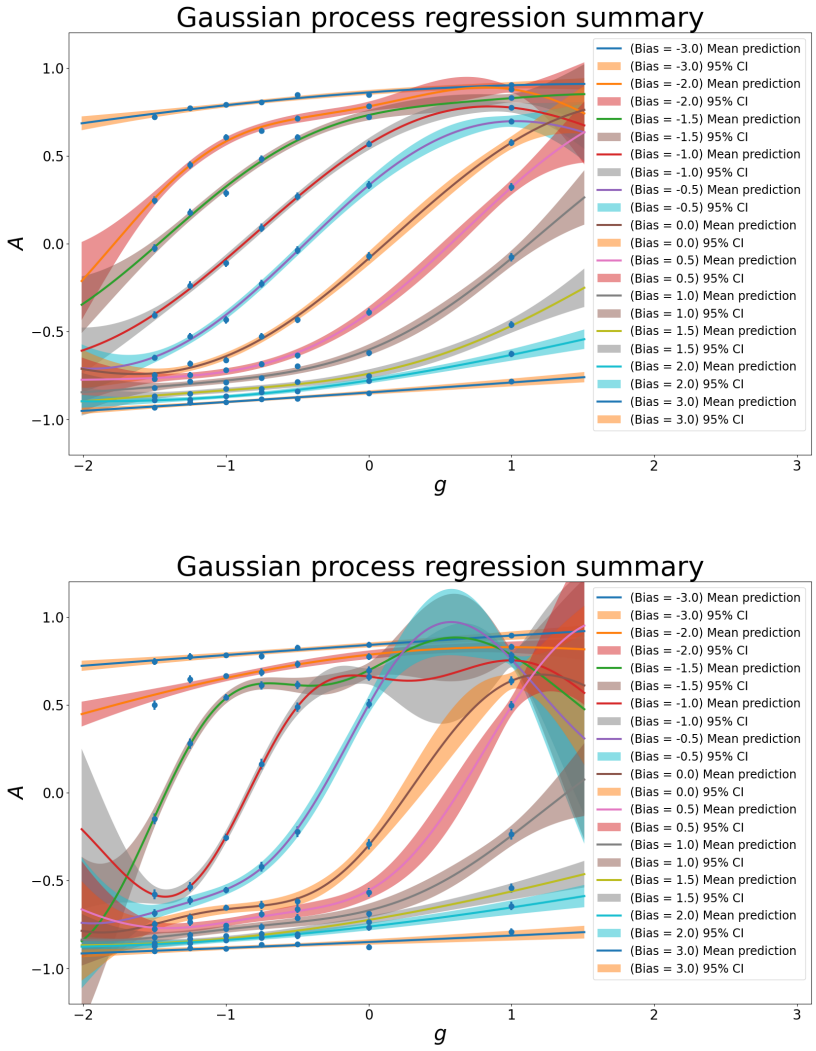

Figure 4.10: Results of Gaussian Process Regression on the fast ramp simulated data (top panel) and on the slow ramp simulated data (bottom panel). The different curves shown in this plot correspond to the different bias configurations. The lines are the mean predictions from Gaussian Process Regression, the bands represent the 95% confidence intervals for the GPR prediction.

$$a_g^{fast} = (-0.75 \pm 0.12)\ g \tag{4.8}$$

this estimate of a_g contains both the statistical uncertainty and the systematic uncertainty due to the uncertainties on the efficiency correction D. To separate the statistical uncertainty of 0.06 g from the systematic uncertainty

of 0.11 g due to D, the fit was performed again fixing D to its mean value (with no Gaussian constraint on the likelihood). The a_g estimate is subject to other sources of systematic uncertainty that will be treated in detail in the next chapter (5). Similarly, for the slow-ramp data we obtain:

$$a_g^{slow} = (-0.86 \pm 0.05)\ g \tag{4.9}$$

also this estimate contains both the statistical uncertainty (0.04 g) and the systematic uncertainty due to D (0.03 g). We point out that these two estimates are correlated, since the datasets from which D is determined overlap. Figure 4.11 shows the confidence intervals for the a_g parameter, for the MAGB fast ramp and slow ramp data. Figure 4.12 shows the A^{raw} asymmetries estimated from data maximising the likelihood of equation 4.1 with superimposed the S-curve for $a_g = 0.75\ g$ extracted via GPR.
As a cross-check, these results have been compared to those obtained by a Bayesian approach, by using $\mathcal{L}(Z|a_g, D, \mathbf{S})$, to determine the a_g posterior probability for a given value of D, by integrating out the nuisance parameters $\mathbf{S}$, and then averaging the results over the D posterior distribution determined in the calibration step. Using this method with a flat prior for a_g over the range $[-3, 3]$ yields, for the fast-ramp data, $a_g = (-0.73 \pm 0.12)\ g$, consistent with the result obtained before.

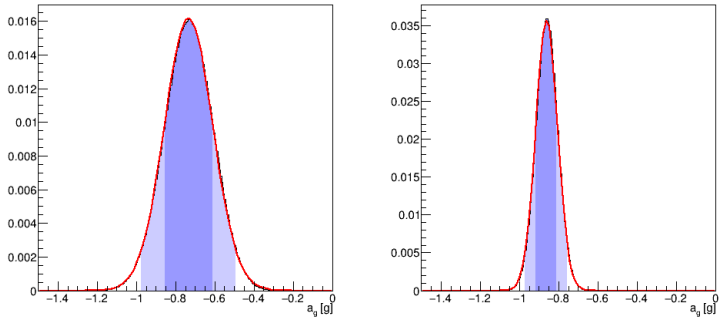

Figure 4.11: Confidence intervals for the a_g parameter, for the MAGB fast ramp (left) and slow ramp data (right). Shaded areas represent 68% (dark shade) and 95% (light shade) CI.

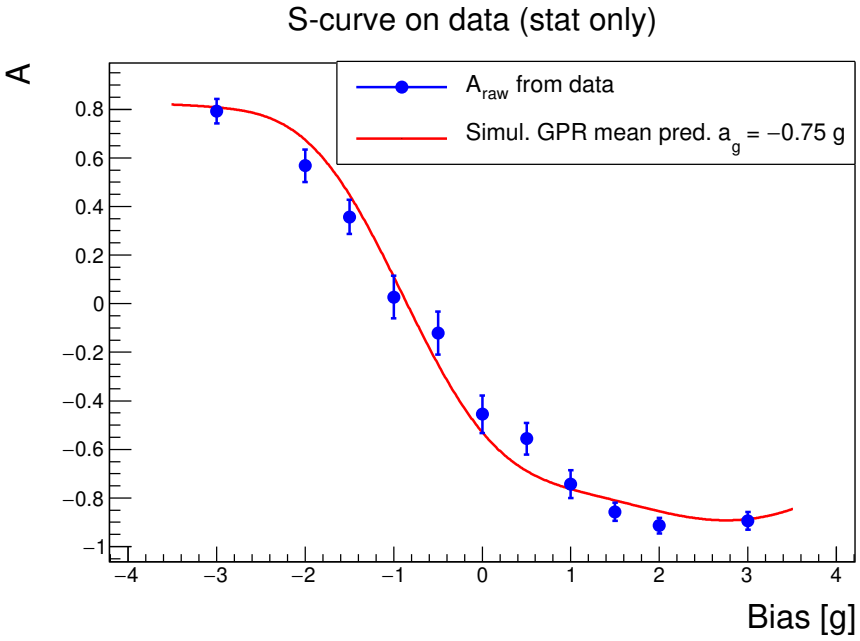

Figure 4.12: This figure shows the A^{raw} asymmetries (blue dots) estimated from data maximising the likelihood of equation 4.1. The error bars include just the statistical contribution. The red curve is the S-curve for $a_g = -0.75\ g$ extracted via GPR. In particular the red line is the mean prediction from GPR.

Chapter 5

Systematic uncertainties on the anti-hydrogen gravitational acceleration

In this chapter are the described the different sources of systematic uncertainty on the estimation of a_g and their treatment.
The dominant source of systematic uncertainty in this measurement is the model used for the simulation of the $\bar{H}$ release, for this reason this source of systematic is treated separately in section 5.2. Section 5.1 addresses all the other sources of systematic uncertainty namely those associated with the extraction of the calibration parameters and the extraction of the value of a_g assuming that the model used for the regression was realistic and the parameters of anti-hydrogen perfectly characterized.

5.1 Systematic uncertainty due to the analysis procedure

This section describes the treatment of the different sources of systematic uncertainty that affect the a_g parameter estimation.

5.1.1 Calibration and background samples size

The *calibration sample* and the *background sample* are used to determine the (binned) probability density functions (PDFs) (f_d, f_u, f_b of equation 4.1). The value of these PDFs in each z bin is affected by an uncertainty due to Poisson fluctuations in the calibration and background samples. To account for these uncertainties a Poisson variation to the binned z distribution is applied in the calibration and background samples. Then, for each varied z distribution a new set of PDFs is determined and the determination of a_g is repeated. This systematic contribution was found to be 0.03 g.

5.1.2 Calibration sample purity assumption

As shown before, the *calibration samples* ($\pm 10g$) are assumed to be pure samples of upwards or downward-released anti-atoms. This means that the asymmetry of these samples is assumed to be $A^{raw} = \mp 1$ for the biases $\pm 10g$ respectively. In order to take into account the systematic uncertainty introduced with this assumption, the assumed asymmetry in the *calibration samples* is changed to the values ∓ 0.99 and ∓ 0.98 and the analysis is performed again for each of these variations. This systematic contribution was found to be compatible with 0.

5.1.3 Uncertainty on the detection efficiency asymmetry

The assumption of proportionality between long octupole counts and the $\bar{H}$ population before the MAGB ramp might not hold due to $\bar{H}$ losses occurring between the two ramps. This time interval is used to measure the on-axis field magnitude at one axial position under each mirror coil using the electron cyclotron resonance (ECR) method (see section 3.4.1), and the losses may vary across runs. A systematic uncertainty is therefore evaluated by varying the numerator of the count ratio $y = \frac{S_{i,o}}{S_i}$ (equation 4.4) by the number of annihilations observed during this interval. The systematic uncertainty on D is found to be 0.02 and is included in the Gaussian constraint on D of equation 4.7 before the fit as described in section 4.5. This systematic contribution was found to be 0.11 g.

5.1.4 Calibration/physics sample discrepancies

The release asymmetry in simulation depends on the considered selection criteria. In particular, while for the fast-ramp data the analysis is calibrated on data that undergo the same treatment as the *physics sample*, for the slow-ramp data the calibration and the *physics samples* undergo different selections, thus introducing a systematic uncertainty. The systematic uncertainty on the PDFs and on the efficiency correction due to time and z selections are estimated from simulations, after accounting for the detector resolution. A cross-check was also performed by comparing the results obtained with different time selections (including 1.1 s after the "porch"). This systematic contribution was found to be negligible.

5.1.5 Simulation sample size

The limited size of the simulation sample leads to a statistical uncertainty on the A_i^{sim} that influences the uncertainty on the GPR predictions for the intermediate a_g values not present in the simulation. This uncertainty on the predicted asymmetries has been propagated to the final result by varying the A_i^{sim} values with a Gaussian distribution with mean equal to the mean

prediction of the GPR and standard deviation equal to the uncertainty on the GPR prediction. The regression is performed for each variation of the set of A^i_{sim} and the resulting posterior distributions are averaged. The variation of the resulting posterior width, with respect to the result obtained without including this effect, is used to estimate this systematic uncertainty and it was found to be 0.02 g.

5.1.6 Effect of the choice of the range of magnetic biases

As the data are collected applying discrete magnetic bias values in the range $[-3, +3]g$, for most acceleration hypotheses, the collected biases are not symmetric around the balance position. This may introduce an acceleration-dependent bias.
This systematic uncertainty is determined from toy experiments generated scanning the values of a_g around the maximum of the posterior probability in figure 4.11 left.
The pull distributions of the $(a_g^{fit} - a_g^{gen})/\sigma_{a_g^{fit}}$, where $\sigma_{a_g^{fit}}$ is the uncertainty on the a_g parameter, are then constructed as shown in figure 5.1. This uncertainty is found to be 0.01 g on a_g.

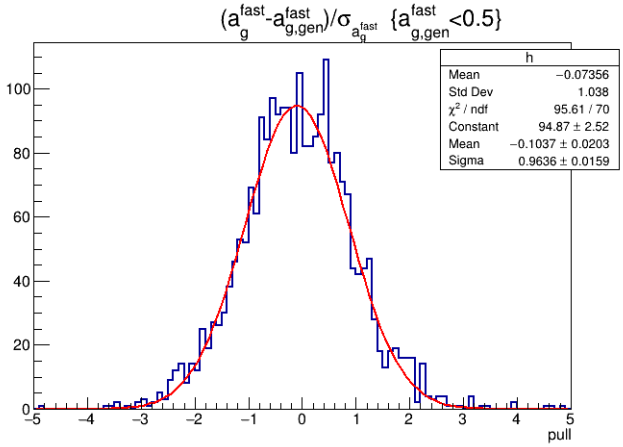

Figure 5.1: Results of fit bias studies: normalized residuals of extracted vs. generated values of a_g for fast ramp configurations generated with $a_g^0 < 0.5$ g.

5.1.7 Simulation interpolation

Due to computing constraints, the distributions of release asymmetries are sampled only at a limited set of acceleration values and for a limited set of bias configurations. The distributions associated to the missing acceleration

values are obtained by Gaussian Process Regression, and the resulting uncertainties must be propagated to the a_g results. In figure 4.10 the results of the Gaussian Process Regression on the fast and slow ramp simulations are shown.
A systematic uncertainty of 0.03 g on a_g, due to the interpolation method, is estimated by comparing the results of the interpolation method described above to the results obtained by an alternative method. In the alternative method, a linear relationship between the on-axis magnetic field bias and the gravitational acceleration is assumed, as observed on simulation, where two experiments yield the same asymmetries if they have the same value of $x = a_g - bias = a_g - \mu_B(B_G - B_A)/[m_H(z_G - z_A)]$. A more detailed description of the tests performed in order to extract this systematic uncertainty is given in section 6.2.3.

5.2 Systematic uncertainties due to the $\bar{H}$ simulation

Apart from the systematic uncertainties mentioned earlier, there are particular sources of systematic uncertainty linked to discrepancies between data and simulation that impact the result on the acceleration parameter.

The simulation reproduces the experimental conditions to the best knowledge, but clearly with some limitations. The model uncertainties resulting from systematic and statistical uncertainties in the tuning (e.g., of the magnetic field and of the initial and final conditions of the $\bar{H}$ population) must be propagated to the a_g results.

5.2.1 Energy distribution of the anti-hydrogen (S-curve slope)

The first source of systematic uncertainty due to the simulation tuning is the one associated to the not well known energy distribution of the $\bar{H}$s released in the MAGB ramp-down. This effect was evaluated using two different approaches. One estimate was obtained by Dr. Andrew Evans [6] simulating a uniform and linear initial energy distributions of the $\bar{H}$s by bootstrapping the results of the nominal 50K Maxwellian initial energy simulation. Using this method systematic uncertainty was found to be 0.03g.
A different approach consists in considering the effect of the late escaping $\bar{H}$s that was evaluated by considering different final time selections in the simulation of the $\bar{H}$ release during the MAGB ramp-down. This approach accounts for the possibility that the time of the $\bar{H}$ escape from the trap in the experimental data is delayed with respect to the one expected from the simulation. A change in the final time selection alters the energy distribution of the $\bar{H}$s released during the MAGB ramp-down. A more tight selection in the MAGB ramp-down (for example $[10, 19.5]$ s instead of $[10, 20]$ s) results

in excluding the least energetic $\bar{H}$s escaping the magnetic field bias when it is really shallow. We note that changing the final time value cut from 20.0 to 19.5 allows to reproduce the more shallow S-curve distribution observed in data with respect to the nominal simulation (see figure 5.2)

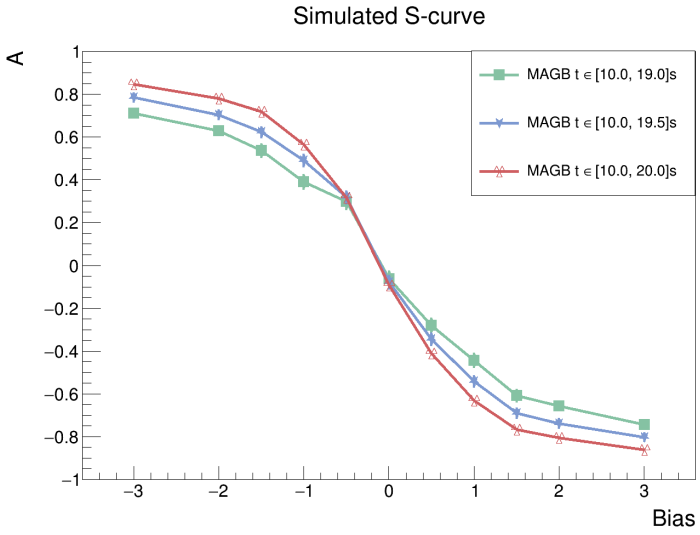

Figure 5.2: Plot of the simulated S-curves obtained for different time cuts. One can notice that the different time cuts influence the S-curve slope.

To estimate the associated systematic uncertainty, the final time cut on the simulation is varied from 19.5 s (that better reproduces the data) to 20 s and to 19.0 s (in order to have a symmetric interval around 19.5 s) and the regression for the extraction of the a_g parameter is repeated (by performing the regression using a model derived from simulation with the different time cuts). This change mostly affects the width of the a_g posterior distribution. For this reason this systematic uncertainty was evaluated as: $(\sqrt{\sigma^2_{19.5} - \sigma^2_{20.0}} + \sqrt{\sigma^2_{19.5} - \sigma^2_{19.0}})/2 = 0.04\ g$ which is very close to the value estimated with the first method.
To avoid double counting, only the estimate from a single method is assigned to this source of uncertainty. In table 5.2 the value obtained from the first method is reported.

5.2.2 On-axis magnetic field

The asymmetries $A_i^{sim}(a_g)$, expected for a given value of the $\bar{H}$ gravitational acceleration, for each configuration (bias) i of the magnetic fields, are evaluated from simulation. In the simulation, and for each configuration, the time evolution of the currents in the various simulated conductive elements are tuned to reproduce the time-dependent on-axis magnetic field observed when running the real experiment in that configuration. The uncertainties

in the experimental characterization of the on-axis magnetic field introduce therefore a systematic uncertainty on the measurement of a_g. This uncertainty source was evaluated by Dr. Chukman So and Dr. Chris Rasmussen. We classify these uncertainties according to whether they're correlated or uncorrelated among biases. The sources of uncertainty uncorrelated between biases are: (1) the uncertainty associated to the ECR spectrum width, that was estimated by the mean of the sum in quadrature of the ECR width of Mirror A and G for all the measured biases; (2) the bias measure reproducibility, given by the standard deviation of all the bias measurements; (3) the uncertainty associated to the extrapolation of the magnetic field maxima positions, that are shifted from the geometrical centre of the mirror coils by some background fields at the end of the ramp; (4) the uncertainty associated to the bias time evolution: the bias is obtained as the average of the biases extracted at the time of each annihilation event using a model of the bias time evolution, the uncertainty is given by the standard deviation of the single calculated biases.
The sources of uncertainty correlated between biases are: (1) the field decay asymmetry between Mirror A and Mirror G between the end of the ramp-down and the field measurement estimated considering the maximum variation asymmetry observed among three investigated biases; (2) the uncertainty on the field modelling, obtained comparing the model prediction with ECR measurements along the nominal ramp for 5 different current configurations, the uncertainty is the mean of the residual between the measurements and the model.
The magnitude of the contributions are listed in table 5.1, and are expressed in units of g using the equivalence in equation 3.21. The contribution of 0.054 g, due to the correlated uncertainties, is the dominant one as it produces a shift to all the biases all at once in the same direction, while the uncertainty of 0.075 g, due to the uncertainties that are uncorrelated across biases, produce a negligible effect on the systematic uncertainties on a_g. Therefore the systematic uncertainty on the a_g parameter due to this source is 0.06 g.
The uncertainty associated to the on-axis magnetic field can be converted into an uncertainty on a_g by assuming a linear relation between the magnetic bias and the gravitational acceleration, as determined in simulations. Therefore the magnetic field contributions are quoted in terms of their effect on a_g.

5.2.3 Off-axis magnetic field

As stated before, the measurements of the magnetic field inside the trap are carried out on-axis, while, in order to obtain the magnetic field values in the 3 dimensions, it is necessary to introduce an off-axis model in which the on-axis measurements are used as a constraint. There are effects that modify

Effect	**Size (g)**
Uncorrelated across biases	
ECR spectrum width	0.07
ΔB reproducibility	0.014
Peak field z-location	0.009
Bias(t)	0.02
Total uncorrelated	0.075
Correlated across biases	
Field decay	0.02
Field modelling	0.05
Total correlated	0.054

Table 5.1: Systematic uncertainties associated to on-axis B-field calibration

the behavior of the off-axis magnetic field (due to possible extrapolation errors) while leaving the on-axis magnetic field unchanged. These effects introduce the off-axis magnetic field systematic uncertainties.
The uncertainty contribution associated to the not well known off-axis field was evaluated by Dr. Andrew Christensen and Dr.Chukman So by studying the impact of possible magnet misalignment on the S-curves [6]. In particular the simulation of the $\bar{H}$ gravity measurement was redone for different possible magnet elements misalignment configurations and the effect of this misalignment on the S-curve intercept with A=0 was evaluated. The magnetic trap elements are described in section 2.7.5.
The maximum shifts from the unperturbed configuration are found to be $\pm 0.26\, g$ (corresponding to the "octupole 8-fold" configurations). They are interpreted here as a worst-case scenario as they are derived by assuming a current in the wires close to the critical current. Because of that, a uniform distribution in range $[-0.26, 0.26]$ g is associated to this source. The treatment of this error source was done by using a convolution of the NLL with a Gaussian distribution with standard deviation equal to $0.52/\sqrt{12} = 0.26/\sqrt{3}$.

The statistical uncertainty together with all the sources of systematic uncertainty on the a_g estimate are reported in table 5.2.

	Source	**Fast ramp** $\sigma(g)$	**Slow ramp** $\sigma(g)$
	Statistical	0.06	0.04
	Systematics		
a)	Efficiency correction	0.11	0.03
b)	Calibration sample size	0.03	0.01
c)	Calibration sample purity	0.00	0.00
d)	Simulation sample size	0.02	0.02
e)	Simulation interpolation	0.03	0.02
f)	Calibration/physics	0.00	0.01
g)	Fit bias (for $a_g < 0.5$)	0.01	0.01
	$\bar{H}$ simulation		
h)	Energy distribution (A_i^{sim} slope)	0.03	0.03
i)	Simulation B-field on-axis tuning	0.06	N/A
l)	Simulation off-axis model - 8-fold	$0.15 = 0.26/\sqrt{3}$	N/A

Table 5.2: Error budget on a_g (in units of g) for the fast and slow ramp data.

Chapter 6

Results and cross checks

From the total likelihood obtained after the regression in section 4.5, for the fast ramp data, the estimate $a_g = (-0.75 \pm 0.12)\ g$ is extracted, where the uncertainty of 0.12 g includes the statistical uncertainty (of 0.06 g) and the systematic uncertainty due to the efficiency correction D (of 0.11 g) (see table 5.2 a)). By including the other sources of systematic uncertainty due to the calibration of the model and the regression described in section 5.1, and quoting the simulation model uncertainties separately due to their subjective nature (see section 5.2 and table 5.2 h), i), l)), the obtained result is:

$$a_g^{(fast)} = [-0.75 \pm 0.06\ (stat.) \pm 0.12\ (syst.) \pm 0.16\ (\bar{H}sim.)]\ g$$

6.1 Significance

In this section the calculation of the significance value of the obtained a_g with respect to the null model is shown. This calculation is intended to assess whether the result obtained is compatible with the zero gravity case. That is, whether the observed effect is due solely to the magnetic fields applied by the experiment. This significance can be calculated by using the likelihood ratio method (incorporating systematic uncertainties by convolution with Gaussian distributions with standard deviation equal to the systematic uncertainties of table 5.2) and relying on the likelihood ratio asymptotic distribution [126]. The use of an approximate method is justified by the large contributions from model systematic uncertainties.
The likelihood scan as a function of a_g is shown in figure 6.1 where the red line is obtained after the inclusion of all systematics and the blue line is obtained after the inclusion of the statistical uncertainty and all systematics (table 5.2 a) to i)) excluding the one associated to the off-axis magnetic field model. The significance of the extracted value of a_g with respect to the null model can then be approximately estimated from the value of the red curve

at $a_g = 0$, in number of standard deviations, as $\Sigma = \sqrt{2 \log \frac{\mathcal{L}(0)}{\mathcal{L}_{max}}} \approx 3.6\ \sigma$. The significance of the extracted value of a_g with respect to the normal gravity model ($a_g = -1$ g) is $\Sigma \approx 1.2\ \sigma$. Moreover the probability of repulsive interaction was also quoted and was found to be negligible.

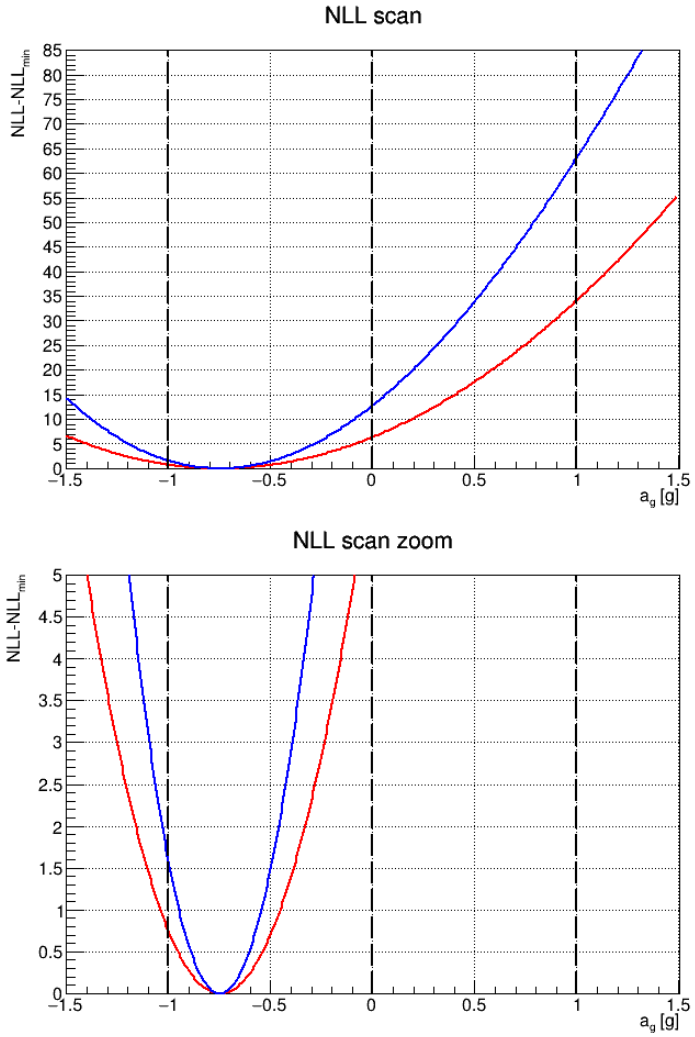

Figure 6.1: Negative log-likelihood scan, relative to its minimum. The red line is obtained after the inclusion of all systematics. The blue line is obtained after the inclusion of the statistical uncertainty and all systematics (table 5.2 a) to i)) excluding the one associated to the off-axis magnetic field model. The bottom plot shows a zoom of the NLL scan between 0 and 5 in the NLL $-$ NLL_{min} axis.

6.2 Cross-Checks

The analysis procedure is validated through the production and analysis of a number of Monte Carlo toys from the probability density functions used for the analysis itself. This is done to verify the correctness of the estimation of parameters and uncertainties, in particular the goal is to verify that the estimated parameters have Gaussian distribution and that the procedure does not introduce any bias to the estimated parameters.
In the final part of this section the tests performed on the GPR fit to the simulation and the extraction of the systematic uncertainty due to the simulation interpolation method are described.

6.2.1 Validation of the fit to the *calibration samples*

The PDFs used for the MAGB ramp-down *calibration samples* are the ones contained in the likelihood of equation 4.1, with a fixed value of the asymmetry ($A^{raw} = \mp 1$ for $\pm 10g$ samples respectively). The PDF used for modelling the the 10g LOc ramp-down samples is the one contained in the likelihood of equation 4.2. For the validation study, the parameters K_i and D_i are set to the values corresponding to those obtained using the Orthogonal Distance regression Method (ODR) on the $S_{i,o}/S_i$ as a function of the A_{raw} data (as described in section 4.4.2).
After that, 1000 pseudo-experiments are generated from the MAGB and LOc PDFs. The ODR fit is applied again to the generated data letting the parameters K_i, D_i to vary. In this way the pull distributions containing the variable

$$\frac{(Par_{Gen} - Par_{Fit})}{\sigma_{Fit}} \tag{6.1}$$

for these parameters are constructed (with 1000 events each). In case the fit procedure is correct and bias-free, these distributions are expected to be Gaussian with mean value equal to zero and standard deviation equal to 1. In the figure 6.2 two of these distributions (for the pair of biases $\pm 10g$) are shown. The distributions obtained are consistent with this statement.

6.2.2 Validation of the fit to the *physics samples*

The likelihood evaluated on the MAGB *physics samples* is the one of equation 4.1 with fixed PDF shapes and cosmic background, and A_i^{raw} to be extracted for each Bias i. For this validation study, the parameters A_i^{raw} are fixed to the values corresponding to those obtained maximizing the likelihood evaluated on the *physics sample* for each bias. After that, 1000 pseudo-experiments are generated starting from the MAGB PDF. The maximum likelihood fit procedure is applied again on the generated data but letting the A_i^{raw} parameters to vary. The pull distributions of A_i^{raw} (see formula

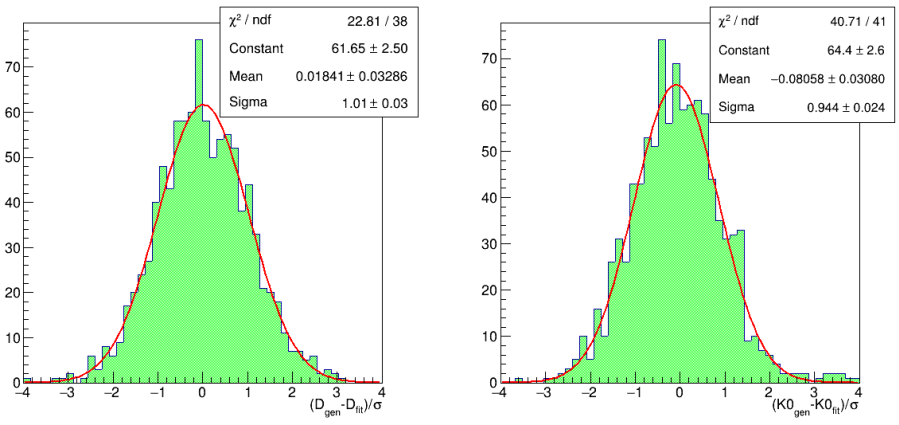

Figure 6.2: Pull distributions of 1000 generated pseudo-experiments for the validation of the analysis on *calibration samples*, in particular for the $\pm 10g$ samples. Left: pull distribution of D parameter. Right: pull distribution of K parameter.

6.1 in the previous paragraph) are shown in figure 6.3. Also in this case the fit behaves correctly, excluding +3g bias where the extracted value of the asymmetry is close to -1.

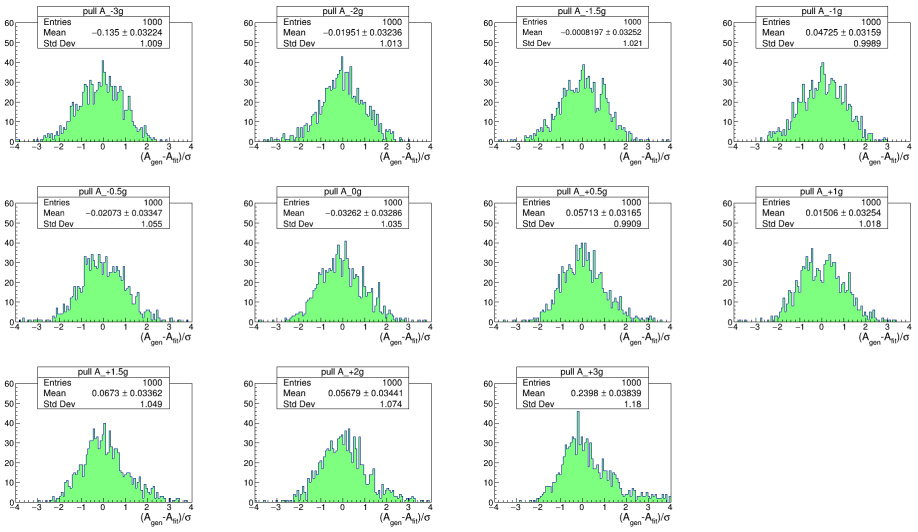

Figure 6.3: Pull distributions of 1000 generated pseudo-experiments for the validation of the analysis on *physics samples*. In the different panels the pull distributions of the different A_i obtained for the different biases are shown.

6.2.3 GPR fitting tests

Gaussian Process Regression fitting is used to obtain predictions on the A_i^{sim} corresponding to a_g values not provided by the simulations, this prediction is performed on the distributions of A_i^{sim} as a function of a_g fixing each bias configuration i, as described in section 4.5.
In this paragraph some tests performed using the GPR fitting in order to evaluate the effect of simulation interpolation on the final a_g result are presented. After the GPR interpolation along the a_g axis, the GPR fitting is applied along the bias axis, the result of this fit is shown in figure 6.4.

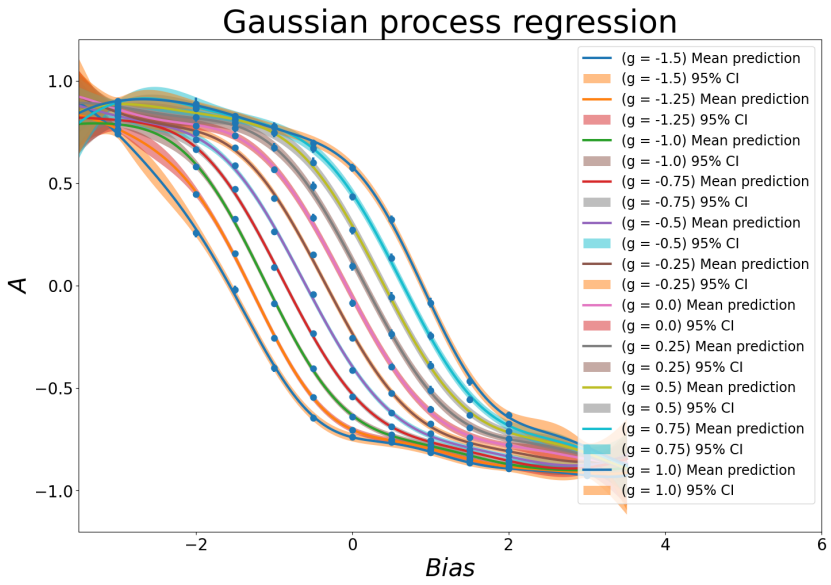

Figure 6.4: Results of Gaussian Process Regression along the bias axis on the fast ramp simulated data. The different curves shown in this plot correspond to different a_g values. The lines are the mean predictions from Gaussian Process Regression, the bands represent the 95% confidence intervals for the GPR prediction.

The uncertainty on the a_g value caused by the choice of the interpolation method applied to the simulation is evaluated extracting the bias bands corresponding to $A^{sim} = 0$ from the different S-curves corresponding to the different values of a_g. The 1-σ uncertainty on the bias is given by the width of the GPR prediction along the bias axis at $A^{sim} = 0$. The plot of the zero-crossing bias as a function of the corresponding a_g values is then constructed and fitted with a first degree polynomial; after that, the plot of the residuals is also constructed. This test is done both using the S-curves corresponding to the a_g values provided by simulations (6.5) and also using GPR predicted

S-curves for some intermediate values of a_g (6.6).

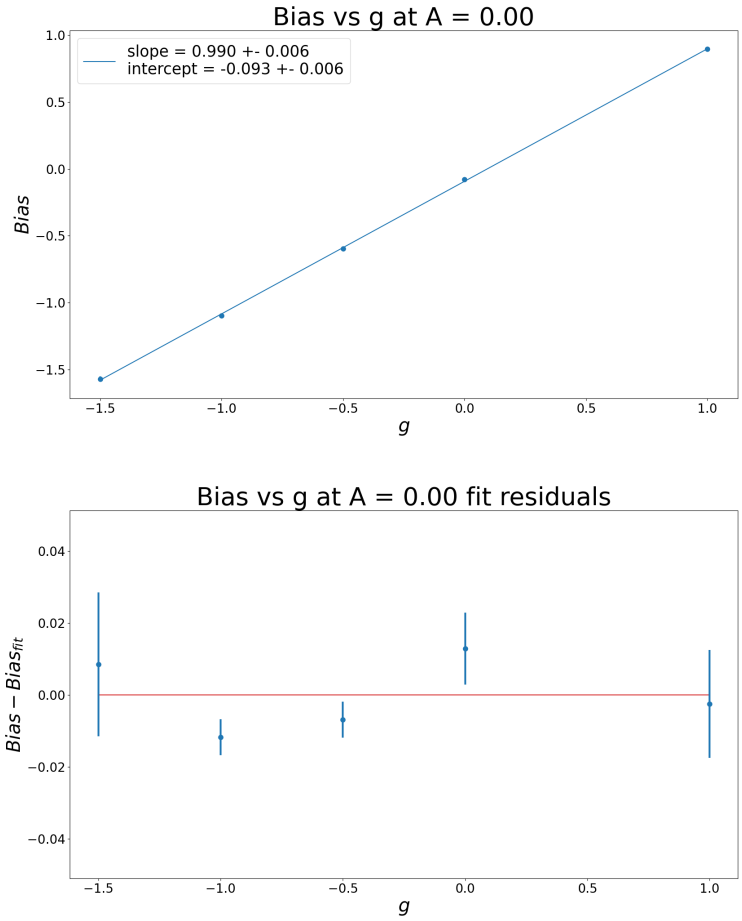

Figure 6.5: Top: zero-crossing bias values (at $A^{sim} = 0$) plotted at the corresponding different values of assumed gravitational acceleration a_g. The values of a_g in this plot are the ones provided directly by simulation. The distribution is fitted with a first degree polynomial in order to test the linearity of the relation. Bottom: plot of the fit residuals as a function of a_g. Note that the slope is compatible with 1, but there are too few points to draw a conclusion from this test.

One can notice that, by including the S-curves predicted with GPR, the residuals have a different structure. This means that extracting the S-curves for intermediate values of a_g with GPR fitting is not exactly equivalent to shifting the S-curves provided by simulation by a certain Δa_g amount along the bias axis. This discrepancy is taken into account in the systematic uncertainty on the final estimated a_g parameter as described in section 5.1.7. The maximum deviation from the linear model in the residuals distribution

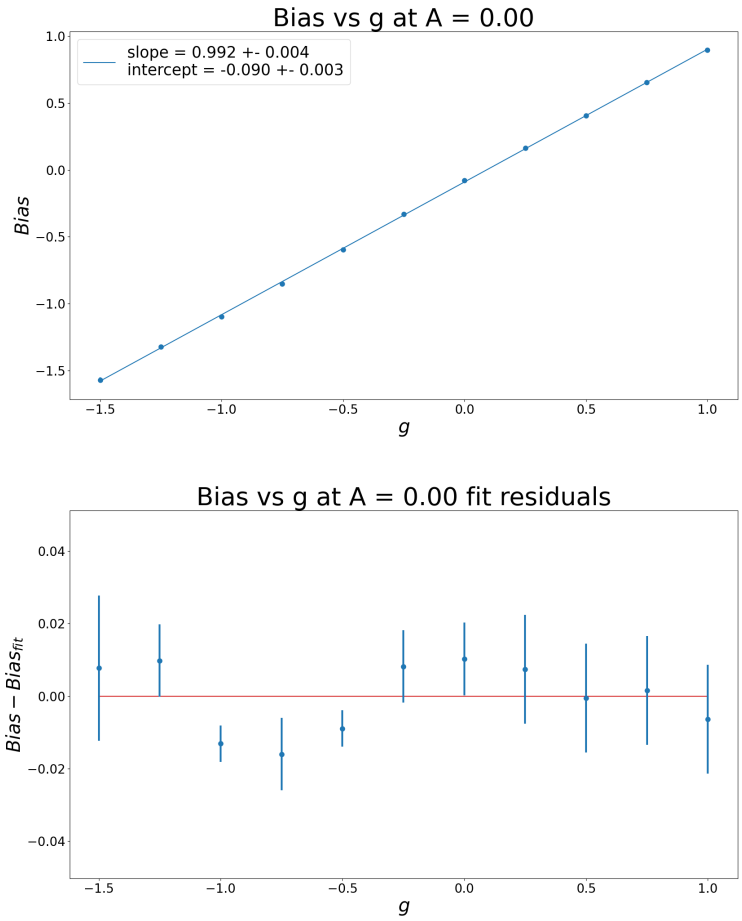

Figure 6.6: Top: zero-crossing bias values (at $A^{sim} = 0$) plotted at the corresponding different values of assumed gravitational acceleration a_g including also some of the GPR predicted S-curves. The distribution is fitted with a first degree polynomial in order to test the linearity of the relation. Bottom: plot of the fit residuals as a function of a_g. Note that the slope is compatible with 1, but the fit residuals have a structure. The maximum deviation from the linear model is taken as an estimate of the uncertainty related to the simulation fitting method.

in figure 6.5 is ~ 0.03 g and this is used as an estimate of the systematic uncertainty on the a_g parameter due to the choice of the simulation interpolation method as reported in section 5.1.7.

Chapter 7

Conclusions

The main topic of this thesis is the determination of the Earth's gravitational acceleration on anti-hydrogen ($\bar{H}$). This measurement was done by the ALPHA experiment at CERN and it represents a test of the Weak Equivalence Principle (WEP) on anti-hydrogen [6].
The $\bar{H}$, is a good candidate for a gravity experiment because of its neutrality. In fact, testing the Weak Equivalence Principle with charged antiparticles and particles is a challenging experiment: in the 1960s some experiments on electrons were attempted but didn't give conclusive results [100, 101], while experiments on positrons were suggested but never developed; furthermore, another experiment to investigate antiproton gravitational acceleration was proposed in the 1990s but never carried out [102, 103].
According to WEP, that is a fundamental principle of Einstein's general relativity theory, all masses have the same gravitational behaviour, independent of their internal structure, so gravitational acceleration of anti-hydrogen on the Earth should be the same as the one of hydrogen.
However, there are proposed alternate cosmological models in which antimatter's gravitational acceleration differs from that of ordinary matter [9, 10]. These theories attempt to explain the dominance of matter over antimatter in our universe while also offering a different approach to the cosmological challenges brought by the presumed existence of dark matter and dark energy. These models are incompatible with WEP and experimental data for testing WEP on antimatter were not present so far.

The first gravity experiment on anti-hydrogen was carried out by ALPHA (*Anti-hydrogen Laser PHysics Apparatus*) during the 2022 data taking and the analysis presented in this thesis, in chapter 4, is performed on these data. The data acquisition procedure is described in detail in section 3.4 and it was performed by accumulating the $\bar{H}$ atoms in the electromagnetic vertical Penning-Malmberg trap embedded in a Ioffe-Pritchard trap of the ALPHAg apparatus, the so called "atom trap" described in section 2.7. In this trap, different magnetic field "biases" (difference between the upper and lower

axial magnetic field barriers) were applied to the $\bar{H}$, that subsequently were released during the ramp-down of the magnets maintaining the "bias". The escaping $\bar{H}$ atoms are released either upwards or downwards with respect to the center of the trap under the effect of the earth's gravitational acceleration combined with the applied magnetic field "bias". The release of the anti-hydrogen atoms causes their annihilation against the trap walls.
Anti-hydrogen annihilation candidates are reconstructed as vertices of two or more tracks in the detector (a radial time projection chamber). These candidates are identified as signal by a classifier based on topological and kinematic variables and trained to reject cosmic background. The annihilation vertex z position is reconstructed, and it is also required to satisfy a set of fiducial cuts in time and z-position.

After the application of time and z-position cuts, the model for constructing the likelihood of the z positions distributions of the annihilation vertices is parameterized in terms of the asymmetry between the up and the down counts. The contributions of the different event sources are taken into account introducing the PDFs of the upwards released anti-atoms, of the downwards released anti-atoms and of the cosmic ray events.
The Probability Density Functions (PDF) for modelling the z distributions of the upwards and downwards released anti-atoms are extracted assuming that for the data collected at "large" "biases" (called calibration samples) the $\bar{H}$ are purely downward or upward-released. The main source of background of this measurement is given by cosmic rays. The cosmic background rates are obtained from the data collected without anti-hydrogen in the experiment.
The total likelihood (including all the data from all the different "biases") and dependent on the anti-hydrogen gravitational acceleration parameter (a_g), is obtained by performing a regression on the extracted asymmetries as a function of the corresponding applied "biases". This regression is done using a simulation (of the magnetic fields and the three-dimensional trajectories of atoms in the trap) that associates to each gravitational acceleration value the expected upwards and downwards escaping anti-atom counts for each "bias" configuration. This simulation is available just for discrete values of gravitational acceleration (a_g); Gaussian Process Regression (GPR) fitting is used to obtain the simulation prediction at intermediate values of a_g.
The sources of systematic uncertainty are divided into two main sources treated separately: the systematic uncertainties associated to the assumptions used in the analysis procedure and to the calibration samples statistics, whose treatment is described in section 5.1; the systematic uncertainty associated to the model used for the regression on the experimental release asymmetries as a function of the applied magnetic "bias", described in section 5.2.

Finally, separating the statistical uncertainty, the systematic uncertainty and the uncertainty associated to the model used for regression, the estimated value of anti-hydrogen acceleration in the Earth's gravitational field is:

$$a_g = [-0.75 \pm 0.06\ (stat.) \pm 0.12\ (syst.) \pm 0.16\ (\bar{H} sim.)]\ g$$

where g is the local gravitational acceleration.
The calculation of the significance value of the obtained a_g with respect to the null model was performed in order to assess whether the obtained result is compatible with the zero gravity case, i.e. if it's just an effect of the magnetic fields applied by the experiment. This significance was calculated by using the likelihood ratio method. The significance of the extracted value of a_g with respect to the null model is then estimated in number of sigmas as $\Sigma = \sqrt{2 \log \frac{\mathcal{L}(0)}{\mathcal{L}_{max}}} \approx 3.6\sigma$. Moreover, the significance of the extracted value of a_g with respect to the normal gravity model ($a_g = -1$ g) is $\Sigma \approx 1.2\ \sigma$.
In conclusion, anti-hydrogen atom's dynamic behaviour is consistent with the existence of an attractive gravitational interaction between anti-hydrogen and the Earth of the same magnitude as for ordinary matter, in line with the WEP.

The ALPHA experiment's next objective is to improve the measurement of the magnitude of gravitational acceleration on $\bar{H}$ in order to be as precise as possible in order to provide a more stringent test of the WEP.
Colder atoms would allow for more sensitive measurements, and the recent demonstration of trapped anti-hydrogen laser cooling by ALPHA [97] is a promising step in this approach. The laser cooling of anti-hydrogen would lead to temperatures below 50 mK, this would steepen the S-curves around the balance point and reduce the uncertainty on the final a_g estimate. Future tests will also include adiabatic expansion cooling of trapped anti-hydrogen [127] and Be^+ ion assisted cooling of the positron plasma [128].
Improving the precision of magnetic field management and measurement in the atom trap and its surroundings is critical since it accounts for the majority of systematic uncertainty in the measurement along with the one associated to simulations. It is worth mentioning here that the ALPHAg central trapping zone, is designed to work with colder atoms and it was not used during the 2022 data taking. The central trapping zone is designed to perform a 1% precision gravity measurement by controlling the trap field at the 10 ppm level (see section 2.7.5 and the article [105]). Fountain-type gravitational interferometry experiments [129] might be performed using this trap (in a medium-long term), with precision of order 10^{-6} in determining a_g.
The coming years will be focused in the attempt to improve our knowledge of the gravitational interaction between matter and antimatter. These mea-

surement, for the first time, will have a solid and promising experimental foundation.

Appendix A

Derivation of gravity measurement model parametrization

DEFINITIONS

Detector counts without efficiency
N_u = *up* number of counts raw (not corrected by detection efficiency)
N_d = *down* number of counts raw (not corrected by detection efficiency)
$S = N_u + N_d$
$A^{raw} = \frac{N_u - N_d}{S}$
consequently
$N_u = \frac{1}{2} \cdot S \cdot (1 + A^{raw})$
$N_d = \frac{1}{2} \cdot S \cdot (1 - A^{raw})$

Detector efficiency
η_u = efficiency in detecting *up* events
η_d = efficiency in detecting *down* events
$\bar{\eta} = \frac{\eta_d + \eta_u}{2}$
$D = \frac{\eta_d - \eta_u}{\eta_u + \eta_d} = \frac{\eta_d - \eta_u}{2\bar{\eta}}$ up-down efficiency asymmetry
consequently
$\eta_u = \bar{\eta} \cdot (1 - D)$
$\eta_d = \bar{\eta} \cdot (1 + D)$

Detector counts with efficiency
n_u = *up* number of counts (corrected by efficiency)
n_d = *down* number of counts (corrected by efficiency)
$s = n_u + n_d$
$A = \frac{n_u - n_d}{s}$
consequently

$n_u = \frac{1}{2} \cdot s \cdot (1 + A)$
$n_d = \frac{1}{2} \cdot s \cdot (1 - A)$

Taking into account the efficiencies we can write that:
$N_u = n_u \cdot \eta_u = n_u \cdot \bar{\eta} \cdot (1 - D)$
$N_d = n_d \cdot \eta_d = n_d \cdot \bar{\eta} \cdot (1 + D)$

Detector counts during Long octupole
S_o = number of counts raw (not corrected by efficiency) during the Long Octupole ramp-down
η_{LOc} = efficiency in detecting LOc events
s_o = number of counts raw (corrected by efficiency) during the Long Octupole ramp-down
$S_o = s_o \cdot \eta_{LOc}$

RELATIONS BETWEEN VARIABLES

S and s

$$S = N_u + N_d = n_u \cdot \bar{\eta} \cdot (1 - D) + n_d \cdot \bar{\eta} \cdot (1 + D) = \bar{\eta} \cdot (n_u + n_d - n_u D + n_d D)$$
$$\Rightarrow S = \bar{\eta} \cdot [s - D(n_u - n_d)] = \bar{\eta} \cdot [s - sD\frac{(n_u - n_d)}{s}]$$
$$\Rightarrow S = s \cdot \bar{\eta} \cdot (1 - DA)$$

analogously

$$s = n_u + n_d = \frac{N_u}{\eta_u} + \frac{N_d}{\eta_d} = \frac{1}{\bar{\eta}}\Big[\frac{N_u}{(1 - D)} + \frac{N_d}{(1 + D)}\Big] = \frac{1}{\bar{\eta} \cdot (1 - D^2)}(N_u + N_d + DN_u - DN_d)$$
$$\Rightarrow s = \frac{1}{\bar{\eta} \cdot (1 - D^2)}\Big(S + DS\frac{N_u - N_d}{S}\Big) = S \cdot \frac{1}{\bar{\eta} \cdot (1 - D^2)}(1 + DA^{raw})$$
$$\Rightarrow s = S \cdot \frac{1 + DA^{raw}}{\bar{\eta} \cdot (1 - D^2)}$$

$\mathbf{A^{raw}}$ and A

$$A^{raw} = \frac{N_u - N_d}{S} = \frac{\bar{\eta}}{S} \cdot \Big[n_u \cdot (1 - D) - n_d \cdot (1 + D)\Big] = \frac{\bar{\eta}}{s \cdot \bar{\eta} \cdot (1 - DA)} \cdot \Big[(n_u - n_d) - D(n_u + n_d)\Big]$$
$$\Rightarrow A^{raw} = \frac{1}{(1 - DA)} \cdot \Big[\frac{(n_u - n_d)}{s} - D\frac{(n_u + n_d)}{s}\Big]$$

$$\Rightarrow A^{raw} = \frac{A - D}{1 - DA} \tag{A.1}$$

analogously

$$A = \frac{n_u - n_d}{s} = \frac{1}{s}\cdot\Big(\frac{N_u}{\eta_u} - \frac{N_d}{\eta_d}\Big) = \frac{\bar{\eta}\cdot(1-D^2)}{S\cdot(1+DA^{raw})}\cdot\Big(\frac{N_u}{\bar{\eta}\cdot(1-D)} - \frac{N_d}{\bar{\eta}\cdot(1+D)}\Big)$$

$$\Rightarrow A = \frac{(1-D^2)}{S\cdot(1+DA^{raw})}\cdot\frac{N_u - N_d + D(N_u+N_d)}{(1-D^2)} = \frac{1}{1+DA^{raw}}\cdot\Big[\frac{N_u - N_d}{S} + D\frac{N_u+N_d}{S}\Big]$$

$$\Rightarrow A = \frac{A^{raw} + D}{1 + DA^{raw}} \tag{A.2}$$

Long octupole and MAGB rampdown

Assuming a proportionality between the *true* (= corrected for the corresponding detector efficiencies) events detected during the Long octupole and during the MAGB rampdowns, then:

$$s \propto s_o$$

This relation can be written taking into account the raw counts

$$S\cdot\frac{1+DA^{raw}}{\bar{\eta}\cdot(1-D^2)} \propto \frac{S_o}{\eta_{LOc}}$$

Introducing an overall constant K, that incorporates also all the efficiencies $\bar{\eta}$ and η_{LOc}, we can thus write:

$$\frac{S_o}{S} = \frac{1}{K\cdot(1-D^2)}\cdot(1+DA^{raw}) \text{ or equivalently } \frac{S_o}{S} = \frac{1}{K}\cdot\frac{1}{1-DA}$$

Error on p and on A

$$A = \frac{A^{Raw} + D}{1 + DA^{Raw}}$$

$$1 - 2p_d = \frac{1 - 2p^{Raw} + D}{1 + D(1-2p_d)}$$

We start with the equation:

$$A = \frac{N_u - N_d}{N_u + N_d}$$

To find the error on A as a function of the errors on N_u and N_d, we use the formula for the propagation of errors:

$$\Delta A/A = \sqrt{\left(\frac{\partial A}{\partial N_u}\Delta N_u\right)^2 + \left(\frac{\partial A}{\partial N_d}\Delta N_d\right)^2}$$

To find the partial derivatives, we first simplify the equation for A:

$$A = \frac{N_u - N_d}{N_u + N_d} = \frac{1 - N_d/N_u}{1 + N_d/N_u}$$

Using the quotient rule, we get:

$$\frac{\partial A}{\partial N_u} = -\frac{(N_d/N_u)^2}{(1 + N_d/N_u)^2}$$

$$\frac{\partial A}{\partial N_d} = \frac{2N_d}{(N_u + N_d)^2}$$

Substituting these partial derivatives into the formula for the error on A, we get:

$$\Delta A/A = \sqrt{\left(\frac{-N_d^2}{N_u^2(1 + N_d/N_u)^2}\Delta N_u\right)^2 + \left(\frac{2N_d}{(N_u + N_d)^2}\Delta N_d\right)^2}$$

Simplifying this expression, we get:

$$\Delta A/A = 2\sqrt{\left(\frac{N_d}{N_u + N_d}\right)^2\left(\frac{\Delta N_u}{N_u}\right)^2 + \left(\frac{N_u}{N_u + N_d}\right)^2\left(\frac{\Delta N_d}{N_d}\right)^2}$$

Therefore, the final formula for the error on A as a function of the errors on N_u and N_d is:

$$\Delta A/A = 2\sqrt{\left(\frac{N_d}{N_u + N_d}\right)^2\left(\frac{\Delta N_u}{N_u}\right)^2 + \left(\frac{N_u}{N_u + N_d}\right)^2\left(\frac{\Delta N_d}{N_d}\right)^2}$$

Bibliography

[1] G. B. Andresen, M. D. Ashkezari, M. Baquero-Ruiz, W. Bertsche, P. D. Bowe, E. Butler, C. L. Cesar, S. Chapman, M. Charlton, A. Deller, S. Eriksson, J. Fajans, T. Friesen, M. C. Fujiwara, D. R. Gill, A. Gutierrez, J. S. Hangst, W. N. Hardy, M. E. Hayden, A. J. Humphries, R. Hydomako, M. J. Jenkins, S. Jonsell, L. V. Jørgensen, L. Kurchaninov, N. Madsen, S. Menary, P. Nolan, K. Olchanski, A. Olin, A. Povilus, P. Pusa, F. Robicheaux, E. Sarid, S. Seif el Nasr, D. M. Silveira, C. So, J. W. Storey, R. I. Thompson, D. P. van der Werf, J. S. Wurtele, and Y. Yamazaki. Trapped antihydrogen. *Nature*, 468(7324):673–676, 2010.

[2] M. Ahmadi, B. X. R. Alves, C. J. Baker, W. Bertsche, E. Butler, A. Capra, C. Carruth, C. L. Cesar, M. Charlton, S. Cohen, R. Collister, S. Eriksson, A. Evans, N. Evetts, J. Fajans, T. Friesen, M. C. Fujiwara, D. R. Gill, A. Gutierrez, J. S. Hangst, W. N. Hardy, M. E. Hayden, C. A. Isaac, A. Ishida, M. A. Johnson, S. A. Jones, S. Jonsell, L. Kurchaninov, N. Madsen, M. Mathers, D. Maxwell, J. T. K. McKenna, S. Menary, J. M. Michan, T. Momose, J. J. Munich, P. Nolan, K. Olchanski, A. Olin, P. Pusa, C. Ø. Rasmussen, F. Robicheaux, R. L. Sacramento, M. Sameed, E. Sarid, D. M. Silveira, S. Stracka, G. Stutter, C. So, T. D. Tharp, J. E. Thompson, R. I. Thompson, D. P. van der Werf, and J. S. Wurtele. Observation of the hyperfine spectrum of antihydrogen. *Nature*, 548(7665):66–69, 2017.

[3] M. Ahmadi, B. X. R. Alves, C. J. Baker, W. Bertsche, A. Capra, C. Carruth, C. L. Cesar, M. Charlton, S. Cohen, R. Collister, S. Eriksson, A. Evans, N. Evetts, J. Fajans, T. Friesen, M. C. Fujiwara, D. R. Gill, J. S. Hangst, W. N. Hardy, M. E. Hayden, E. D. Hunter, C. A. Isaac, M. A. Johnson, J. M. Jones, S. A. Jones, S. Jonsell, A. Khramov, P. Knapp, L. Kurchaninov, N. Madsen, D. Maxwell, J. T. K. McKenna, S. Menary, J. M. Michan, T. Momose, J. J. Munich, K. Olchanski, A. Olin, P. Pusa, C. Ø. Rasmussen, F. Robicheaux, R. L. Sacramento, M. Sameed, E. Sarid, D. M. Silveira, D. M. Starko, G. Stutter, C. So, T. D. Tharp, R. I. Thompson, D. P. van der Werf,

and J. S. Wurtele. Observation of the 1s–2p lyman- transition in antihydrogen. *Nature*, 561(7722):211–215, 2018.

[4] M. Ahmadi, B. X. R. Alves, C. J. Baker, W. Bertsche, A. Capra, C. Carruth, C. L. Cesar, M. Charlton, S. Cohen, R. Collister, S. Eriksson, A. Evans, N. Evetts, J. Fajans, T. Friesen, M. C. Fujiwara, D. R. Gill, J. S. Hangst, W. N. Hardy, M. E. Hayden, C. A. Isaac, M. A. Johnson, J. M. Jones, S. A. Jones, S. Jonsell, A. Khramov, P. Knapp, L. Kurchaninov, N. Madsen, D. Maxwell, J. T. K. McKenna, S. Menary, T. Momose, J. J. Munich, K. Olchanski, A. Olin, P. Pusa, C. Ø. Rasmussen, F. Robicheaux, R. L. Sacramento, M. Sameed, E. Sarid, D. M. Silveira, G. Stutter, C. So, T. D. Tharp, R. I. Thompson, D. P. van der Werf, and J. S. Wurtele. Characterization of the 1s–2s transition in antihydrogen. *Nature*, 557(7703):71–75, 2018.

[5] M. Ahmadi, M. Baquero-Ruiz, W. Bertsche, E. Butler, A. Capra, C. Carruth, C. L. Cesar, M. Charlton, A. E. Charman, S. Eriksson, L. T. Evans, N. Evetts, J. Fajans, T. Friesen, M. C. Fujiwara, D. R. Gill, A. Gutierrez, J. S. Hangst, W. N. Hardy, M. E. Hayden, C. A. Isaac, A. Ishida, S. A. Jones, S. Jonsell, L. Kurchaninov, N. Madsen, D. Maxwell, J. T. K. McKenna, S. Menary, J. M. Michan, T. Momose, J. J. Munich, P. Nolan, K. Olchanski, A. Olin, A. Povilus, P. Pusa, C. Ø. Rasmussen, F. Robicheaux, R. L. Sacramento, M. Sameed, E. Sarid, D. M. Silveira, C. So, T. D. Tharp, R. I. Thompson, D. P. van der Werf, J. S. Wurtele, and A. I. Zhmoginov. An improved limit on the charge of antihydrogen from stochastic acceleration. *Nature*, 529(7586):373–376, 2016.

[6] E. K. Anderson et al. Observation of the effect of gravity on the motion of antimatter. *Nature*, 621(7980):716–722, 2023.

[7] P. AR Ade, N. Aghanim, MIR Alves, C. Armitage-Caplan, M Arnaud, M Ashdown, F Atrio-Barandela, J Aumont, H Aussel, C Baccigalupi, et al. Planck 2013 results. i. overview of products and scientific results. *Astronomy and Astrophysics*, 571:A1, 2014.

[8] A. D. Sakharov. Violation of CP Invariance, C asymmetry, and baryon asymmetry of the universe. *Pisma Zh. Eksp. Teor. Fiz.*, 5:32–35, 1967.

[9] D. S. Hajdukovic. Do we live in the universe successively dominated by matter and antimatter? *Astrophysics and Space Science*, 334(2):219–223, 2011.

[10] A. Benoit-Lévy and G. Chardin. Introducing the dirac-milne universe. *Astronomy &amp Astrophysics*, 537:A78, 2012.

[11] G. Bertone and D. Hooper. History of dark matter. *Rev. Mod. Phys.*, 90:045002, 2018.

[12] A. G. Riess, A. V. Filippenko, P. Challis, A. Clocchiatti, A. Diercks, P. M. Garnavich, R. L. Gilliland, C. J. Hogan, S. Jha, R. P. Kirshner, B. Leibundgut, M. M. Phillips, D. Reiss, B. P. Schmidt, R. A. Schommer, R. C. Smith, J. Spyromilio, C. Stubbs, N. B. Suntzeff, and J. Tonry. Observational evidence from supernovae for an accelerating universe and a cosmological constant. *The Astronomical Journal*, 116(3):1009–1038, 1998.

[13] S. Perlmutter, G. Aldering, G. Goldhaber, R. A. Knop, P. Nugent, P. G. Castro, S. Deustua, S. Fabbro, A. Goobar, D. E. Groom, I. M. Hook, A. G. Kim, M. Y. Kim, J. C. Lee, N. J. Nunes, R. Pain, C. R. Pennypacker, R. Quimby, C. Lidman, R. S. Ellis, M. Irwin, R. G. McMahon, P. Ruiz-Lapuente, N. Walton, B. Schaefer, B. J. Boyle, A. V. Filippenko, T. Matheson, A. S. Fruchter, N. Panagia, H. J. M. Newberg, W. J. Couch, and The Supernova Cosmology Project. Measurements of ω and λ from 42 high-redshift supernovae. *The Astrophysical Journal*, 517(2):565–586, 1999.

[14] B. A. Robson. *Redefining Standard Model Cosmology.* IntechOpen, Rijeka, 2019.

[15] N. Aghanim et al. Planck 2018 results. VI. Cosmological parameters. *Astron. Astrophys.*, 641:A6, 2020. [Erratum: Astron.Astrophys. 652, C4 (2021)].

[16] M. Thomson. *Modern particle physics.* Cambridge University Press, New York, 2013.

[17] A. Friedman. Über die krümmung des raumes. *Zeitschrift für Physik*, 10(1):377–386, 1922.

[18] G. Lemaître. Un univers homogène de masse constante et de rayon croissant rendant compte de la vitesse radiale des nébuleuses extra-galactiques. *Annales de la Société Scientifique de Bruxelles, A47, p. 49-59*, 47:49–59, 1927.

[19] E. Hubble. A relation between distance and radial velocity among extra-galactic nebulae. *Proceedings of the national academy of sciences*, 15(3):168–173, 1929.

[20] A. A Penzias and R.W. Wilson. A measurement of excess antenna temperature at 4080 mc/s. *Astrophysical Journal, vol. 142, p. 419-421*, 142:419–421, 1965.

[21] R. A Alpher, H. Bethe, and G. Gamow. The origin of chemical elements. *Physical Review*, 73(7):803, 1948.

[22] L. Canetti, M. Drewes, and M. Shaposhnikov. Matter and antimatter in the universe. *New Journal of Physics*, 14(9):095012, 2012.

[23] Gary Steigman. Primordial nucleosynthesis: The predicted and observed abundances and their consequences, 2010.

[24] E. Komatsu et al. K. M. Smith, J. Dunkley, C. L. Bennett, B. Gold, G. Hinshaw, N. Jarosik, D. Larson, M. R. Nolta, L. Page, D. N. Spergel, M. Halpern, R. S. Hill, A. Kogut, M. Limon, S. S. Meyer, N. Odegard, G. S. Tucker, J. L. Weiland, E. Wollack, and E. L. Wright. Seven-year wilkinson microwave anisotropy probe (wmap) observations: Cosmological interpretation. *The Astrophysical Journal Supplement Series*, 192(2):18, 2011.

[25] C. S. Wu, E. Ambler, R. W. Hayward, D. D. Hoppes, and R. P. Hudson. Experimental test of parity conservation in beta decay. *Phys. Rev.*, 105:1413–1415, 1957.

[26] J. H. Christenson, J. W. Cronin, V. L. Fitch, and R. Turlay. Evidence for the 2π Decay of the K_2^0 Meson. *Phys. Rev. Lett.*, 13:138–140, 1964.

[27] Glennys R. Farrar and M. E. Shaposhnikov. Baryon asymmetry of the universe in the minimal standard model. *Phys. Rev. Lett.*, 70:2833–2836, 1993.

[28] N. Cabibbo. Unitary symmetry and leptonic decays. *Phys. Rev. Lett.*, 10:531–533, 1963.

[29] M. Kobayashi and T. Maskawa. CP-Violation in the Renormalizable Theory of Weak Interaction. *Progress of Theoretical Physics*, 49(2):652–657, 1973.

[30] M. Gell-Mann. A Schematic Model of Baryons and Mesons. *Phys. Lett.*, 8:214–215, 1964.

[31] G. Zweig. *An SU(3) model for strong interaction symmetry and its breaking. Version 2*, pages 22–101. 1964.

[32] B. Robson. The matter-antimatter asymmetry problem. *Journal of High Energy Physics, Gravitation and Cosmology*, 04:166–178, 2018.

[33] M. Dine and A. Kusenko. Origin of the matter-antimatter asymmetry. *Rev. Mod. Phys.*, 76:1–30, 2003.

[34] A. Ekstedt and J. Löfgren. A critical look at the electroweak phase transition. *Journal of High Energy Physics*, 2020(12), 2020.

[35] W. Buchmüller, R.D. Peccei, and T. Yanagida. Leptogenesis as the origin of matter. *Annual Review of Nuclear and Particle Science*, 55(1):311–355, 2005.

[36] M. Shaposhnikov. Baryogenesis. *Journal of Physics: Conference Series*, 171(1):012005, 2009.

[37] B. Garbrecht. Why is there more matter than antimatter? calculational methods for leptogenesis and electroweak baryogenesis. *Progress in Particle and Nuclear Physics*, 110:103727, 2020.

[38] A. G. Cohen and D. B. Kaplan. Thermodynamic generation of the baryon asymmetry. *Physics Letters B*, 199(2):251–258, 1987.

[39] D. Colladay and V. A. Kostelecký. CPT violation and the standard model. *Phys. Rev. D*, 55:6760–6774, 1997.

[40] D. Colladay and V. A. Kostelecký. Lorentz-violating extension of the standard model. *Phys. Rev. D*, 58:116002, 1998.

[41] M. Charlton, S. Eriksson, and G. M. Shore. Testing fundamental physics in antihydrogen experiments, 2022.

[42] E. W. Kolb and M. S. Turner. *The Early Universe*, volume 69. 1990.

[43] V. A. Kostelecký and Neil Russell. Data tables for lorentz and cpt violation. *Reviews of Modern Physics*, 83(1):11–31, 2011.

[44] O. Bertolami, D. Colladay, V.A. Kostelecký, and R. Potting. CPT violation and baryogenesis. *Physics Letters B*, 395(3-4):178–183, 1997.

[45] V. A. Kostelecký and Matthew Mewes. Fermions with lorentz-violating operators of arbitrary dimension. *Physical Review D*, 88(9), 2013.

[46] C. M. Will. The confrontation between general relativity and experiment. 2014.

[47] R. H. Dicke. Republication of: The theoretical significance of experimental relativity. *General Relativity and Gravitation*, 51(5), 2019.

[48] M. M. Nieto and J. Terrance Goldman. The Arguments against 'antigravity' and the gravitational acceleration of antimatter. *Phys. Rept.*, 205:221–281, 1991.

[49] R. P. Feynman. *Feynman lectures on gravitation.* 1996.

[50] D. C. Peaslee. Nonexistence of gravity shields. *Science*, 124(3235):1292–1292, 1956.

[51] H. Bondi and T. Gold. The Steady-State Theory of the Expanding Universe. *Mon. Not. Roy. Astron. Soc.*, 108:252, 1948.

[52] F. Hoyle. A New Model for the Expanding Universe. 108(5):372–382, 1948.

[53] H. Bondi. Negative Mass in General Relativity. *Rev. Mod. Phys.*, 29:423–428, 1957.

[54] P. Morrison. Approximate Nature of Physical Symmetries. *American Journal of Physics*, 26(6):358–368, 1958.

[55] L. I. Schiff. Sign of the gravitational mass of a positron. *Phys. Rev. Lett.*, 1:254–255, 1958.

[56] T. Yarman, A.L. Kholmetskii, C. Marchal, O. Yarman, and M. Arik. The eötvös experiment, gtr, and differing gravitational and inertial masses proposition for a crucial test of metric theories. *Journal of Physics: Conference Series*, 1251(1):012051, 2019.

[57] F. Scuri and G. Zavattini. On the possibility to detect a vector term in the gravitational potential through the vacuum polarization in atoms. *Physics Letters B*, 220(1):276–278, 1989.

[58] T.E.O. Ericson and A. Richter. Empirical limits to antigravity. *EPL*, 11:295–300, 1990.

[59] M. L. Good. ${K_2}^0$ and the equivalence principle. *Phys. Rev.*, 121:311–313, 1961.

[60] G. Chardin. Cp violation and antigravity (revisited). *Nuclear Physics A*, 558:477–495, 1993.

[61] D. V. Ahluwalia. Nonlocality and gravity-induced CP violation. *Modern Physics Letters A*, 13(39):3123–3136, 1998.

[62] R. M. Santilli. *Isodual theory of point-like antiparticles*, pages 85–136. Springer Netherlands, Dordrecht, 2006.

[63] R. Santilli. Elements of iso-, geno-, hyper-mathematics for matter, their isoduals for antimatter, and their applications in physics, chemistry, and biology. *Foundations of Physics*, 33:1373–1416, 2003.

[64] A. G. Riess, P. E. Nugent, R. L. Gilliland, B. P. Schmidt, J. Tonry, M. Dickinson, R. I. Thompson, T. Budavári, S. Casertano, A. S. Evans, A. V. Filippenko, M. Livio, D. B. Sanders, A. E. Shapley, H. Spinrad, C. C. Steidel, D. Stern, J. Surace, and S. Veilleux. The farthest known supernova: Support for an accelerating universe and

a glimpse of the epoch of deceleration. *The Astrophysical Journal*, 560(1):49, 2001.

[65] S. Perlmutter. Supernovae, dark energy, and the accelerating universe: The status of the cosmological parameters. *International Journal of Modern Physics A - IJMPA*, 15:715–739, 2000.

[66] D. Dürr, S. Goldstein, and N. Zanghì. Quantum equilibrium and the role of operators as observables in quantum theory. *Journal of Statistical Physics*, 116(1-4):959–1055, 2004.

[67] J. M. Ripalda. Time reversal and negative energies in general relativity, 2010.

[68] S. Menary. What exactly is antimatter (gravitationally speaking)?, 2024.

[69] Y. Yang, J. Liang, Y. Bi, Y. Chen, T. Draper, K. Liu, and Z. Liu. Proton mass decomposition from the qcd energy momentum tensor. *Phys. Rev. Lett.*, 121:212001, 2018.

[70] S. Adhikari, F. Afzal, C. S. Akondi, M. Albrecht, M. Amaryan, V. Arroyave, A. Asaturyan, A. Austregesilo, Z. Baldwin, F. Barbosa, J. Barlow, E. Barriga, R. Barsotti, T. D. Beattie, V. V. Berdnikov, T. Black, W. Boeglin, W. J. Briscoe, T. Britton, W. K. Brooks, D. Byer, E. Chudakov, P. L. Cole, O. Cortes, V. Crede, M. M. Dalton, D. Darulis, A. Deur, S. Dobbs, A. Dolgolenko, R. Dotel, M. Dugger, R. Dzhygadlo, D. Ebersole, H. Egiyan, T. Erbora, P. Eugenio, A. Fabrizi, C. Fanelli, S. Fang, S. Fegan, J. Fitches, A. M. Foda, S. Furletov, L. Gan, H. Gao, A. Gardner, A. Gasparian, C. Gleason, K. Goetzen, V. S. Goryachev, B. Grube, J. Guo, L. Guo, T. J. Hague, H. Hakobyan, J. Hernandez, N. D. Hoffman, D. Hornidge, G. Hou, G. M. Huber, P. Hurck, A. Hurley, W. Imoehl, D. G. Ireland, M. M. Ito, I. Jaegle, N. S. Jarvis, T. Jeske, R. T. Jones, V. Kakoyan, G. Kalicy, V. Khachatryan, M. Khatchatryan, C. Kourkoumelis, A. LaDuke, I. Larin, D. Lawrence, D. I. Lersch, H. Li, W. B. Li, B. Liu, K. Livingston, G. J. Lolos, L. Lorenti, V. Lyubovitskij, D. Mack, A. Mahmood, P. P. Martel, H. Marukyan, V. Matveev, M. McCaughan, M. McCracken, C. A. Meyer, R. Miskimen, R. E. Mitchell, K. Mizutani, V. Neelamana, L. Ng, E. Nissen, S. Orešić, A. I. Ostrovidov, Z. Papandreou, C. Paudel, R. Pedroni, L. Pentchev, K. J. Peters, E. Prather, S. Rakshit, J. Reinhold, A. Remington, B. G. Ritchie, J. Ritman, G. Rodriguez, D. Romanov, K. Saldana, C. Salgado, S. Schadmand, A. M. Schertz, K. Scheuer, A. Schick, A. Schmidt, R. A. Schumacher, J. Schwiening, P. Sharp, X. Shen, M. R. Shepherd, A. Smith, E. S. Smith, D. I. Sober, S. Somov, A. Somov, J. R.

Stevens, I. I. Strakovsky, B. Sumner, K. Suresh, V. V. Tarasov, S. Taylor, A. Teymurazyan, A. Thiel, T. Viducic, T. Whitlatch, N. Wickramaarachchi, M. Williams, Y. Wunderlich, B. Yu, J. Zarling, Z. Zhang, Z. Zhao, X. Zhou, J. Zhou, and B. Zihlmann. Measurement of the j/ψ photoproduction cross section over the full near-threshold kinematic region. *Physical Review C*, 108(2), 2023.

[71] B. Duran, Z.-E. Meziani, S. Joosten, M. K. Jones, S. Prasad, C. Peng, W. Armstrong, H. Atac, E. Chudakov, H. Bhatt, D. Bhetuwal, M. Boer, A. Camsonne, J.-P. Chen, M. M. Dalton, N. Deokar, M. Diefenthaler, J. Dunne, L. El Fassi, E. Fuchey, H. Gao, D. Gaskell, O. Hansen, F. Hauenstein, D. Higinbotham, S. Jia, A. Karki, C. Keppel, P. King, H. S. Ko, X. Li, R. Li, D. Mack, S. Malace, M. McCaughan, R. E. McClellan, R. Michaels, D. Meekins, Michael Paolone, L. Pentchev, E. Pooser, A. Puckett, R. Radloff, M. Rehfuss, P. E. Reimer, S. Riordan, B. Sawatzky, A. Smith, N. Sparveris, H. Szumila-Vance, S. Wood, J. Xie, Z. Ye, C. Yero, and Z. Zhao. Determining the gluonic gravitational form factors of the proton. *Nature*, 615(7954):813–816, 2023.

[72] D. A. Pefkou, D. C. Hackett, and P. E. Shanahan. Gluon gravitational structure of hadrons of different spin. *Physical Review D*, 105(5), 2022.

[73] K. A. Mamo and I. Zahed. j/ψ near threshold in holographic qcd: a and d gravitational form factors. *Physical Review D*, 106(8), 2022.

[74] T. A. Wagner, S. Schlamminger, J. H. Gundlach, and E. G. Adelberger. Torsion-balance tests of the weak equivalence principle. *Classical and Quantum Gravity*, 29(18):184002, 2012.

[75] Pierre Touboul, Gilles Métris, Manuel Rodrigues, Joel Bergé, Alain Robert, Quentin Baghi, Yves André, Judicaël Bedouet, Damien Boulanger, Stefanie Bremer, Patrice Carle, Ratana Chhun, Bruno Christophe, Valerio Cipolla, Thibault Damour, Pascale Danto, Louis Demange, Hansjoerg Dittus, Océane Dhuicque, Pierre Fayet, Bernard Foulon, Pierre-Yves Guidotti, Daniel Hagedorn, Emilie Hardy, Phuong-Anh Huynh, Patrick Kayser, Stéphanie Lala, Claus Lämmerzahl, Vincent Lebat, Françoise Liorzou, Meike List, Frank Löffler, Isabelle Panet, Martin Pernot-Borràs, Laurent Perraud, Sandrine Pires, Benjamin Pouilloux, Pascal Prieur, Alexandre Rebray, Serge Reynaud, Benny Rievers, Hanns Selig, Laura Serron, Timothy Sumner, Nicolas Tanguy, Patrizia Torresi, and Pieter Visser. *MICROSCOPE* mission: Final results of the test of the equivalence principle. *Physical Review Letters*, 129(12), September 2022.

[76] M. Hori and J. Walz. Physics at CERN's antiproton decelerator. *Progress in Particle and Nuclear Physics*, 72:206–253, 2013.

[77] B. Autin, F. Perriollat, A. Poncet, D. Möhl, H. Mulder, F. Pedersen, J. Bosser, M. Giovannozzi, R. Giannini, S. Maury, et al. The antiproton decelerator (ad), a simplified antiproton source (feasibility study). Technical report, 1995.

[78] S. Maury. The antiproton decelerator: Ad. *Hyperfine Interactions*, 109(1-4):43–52, 1997.

[79] P. Belochitskii, J. Bosser, J. Buttkus, C. Carli, F. Caspers, V. Chohan, D. Cornuet, T. Eriksson, A. Findlay, M. Giovannozzi, et al. Commissioning and first operation of the antiproton decelerator (ad). In *PACS2001. Proceedings of the 2001 particle accelerator conference (Cat. No. 01CH37268)*, volume 1, pages 580–584. IEEE, 2001.

[80] G. Tranquille, P. Belochitskii, S. Maury, W. Oelert, and T. Eriksson. Elena: from the first ideas to the project. In *Conf. Proc.*, volume 1205201, page THPPP017, 2012.

[81] T. Eriksson, S. Pasinelli, W. Oelert, P. Belochitskii, F. Butin, W. Bartmann, C. Carli, S. Maury, H. Breuker, G. Tranquille, et al. The elena project: progress in the design. In *Conf. Proc.*, volume 1205201, page THPPP008, 2012.

[82] V. Chohan, C. Alanzeau, ME. Angoletta, J. Baillie, D. Barna, W. Bartmann, P. Belochitskii, J. Borburgh, H. Breuker, F. Butin, et al. Extra low energy antiproton (elena) ring and its transfer lines: Design report. 2014.

[83] R. Caravita et al. The AEgIS experiment at CERN: Probing antimatter gravity. *Nuovo Cim. C*, 42(2-3):123, 2019.

[84] E. Widmann. Atomic spectroscopy and collisions using slow antiprotons — the asacusa experiment at cern-ad. In H. Knudsen, J. U. Andersen, and H. Kluge, editors, *Atomic Physics at Accelerators: Stored Particles and Fundamental Physics*, pages 313–317, Dordrecht, 2003. Springer Netherlands.

[85] B. M. Latacz et al. BASE—high-precision comparisons of the fundamental properties of protons and antiprotons. *Eur. Phys. J. D*, 77(6):94, 2023.

[86] P. Perez, D. Banerjee, F. Biraben, D. Brook-Roberge, M. Charlton, P. Cladé, P. Comini, P. Crivelli, O. Dalkarov, P. Debu, A. Douillet, G. Dufour, P. Dupré, S. Eriksson, P. Froelich, P. Grandemange,

S. Guellati-Khelifa, R. Guérout, J. Heinrich, and Y. Yamazaki. The gbar antimatter gravity experiment. *Hyperfine Interactions*, 233:21–27, 2015.

[87] T. Aumann et al. PUMA, antiProton unstable matter annihilation. *Eur. Phys. J. A*, 58(5):88, 2022.

[88] C. J. Baker et al. Design and performance of a novel low energy multispecies beamline for an antihydrogen experiment. *Phys. Rev. Accel. Beams*, 26(4):040101, 2023.

[89] C. Amole, G.B. Andresen, M.D. Ashkezari, M. Baquero-Ruiz, W. Bertsche, P.D. Bowe, E. Butler, A. Capra, P.T. Carpenter, C.L. Cesar, S. Chapman, M. Charlton, A. Deller, S. Eriksson, J. Escallier, J. Fajans, T. Friesen, M.C. Fujiwara, D.R. Gill, A. Gutierrez, J.S. Hangst, W.N. Hardy, R.S. Hayano, M.E. Hayden, A.J. Humphries, J.L. Hurt, R. Hydomako, C.A. Isaac, M.J. Jenkins, S. Jonsell, L.V. Jørgensen, S.J. Kerrigan, L. Kurchaninov, N. Madsen, A. Marone, J.T.K. McKenna, S. Menary, P. Nolan, K. Olchanski, A. Olin, B. Parker, A. Povilus, P. Pusa, F. Robicheaux, E. Sarid, D. Seddon, S. Seif El Nasr, D.M. Silveira, C. So, J.W. Storey, R.I. Thompson, J. Thornhill, D. Wells, D.P. van der Werf, J.S. Wurtele, and Y. Yamazaki. The alpha antihydrogen trapping apparatus. *Nuclear Instruments and Methods in Physics Research Section A: Accelerators, Spectrometers, Detectors and Associated Equipment*, 735:319–340, 2014.

[90] L. S. Brown and G. Gabrielse. Geonium theory: Physics of a single electron or ion in a penning trap. *Rev. Mod. Phys.*, 58:233–311, 1986.

[91] P. Granum. *Measuring the Properties of Antihydrogen*. PhD thesis, 2022.

[92] G. Andresen, W. Bertsche, P. Bowe, C. Bray, E. Butler, C. Cesar, S. Chapman, M. Charlton, J. Fajans, M. Fujiwara, D. Gill, J. Hangst, W. Hardy, R. Hayano, M. Hayden, A. Humphries, R. Hydomako, L. Jørgensen, S. Kerrigan, and Y. Yamazaki. Antiproton, positron, and electron imaging with a microchannel plate/phosphor detector alpha collaboration. *The Review of scientific instruments*, 80:123701, 2009.

[93] T. J. Murphy and C. M. Surko. Positron trapping in an electrostatic well by inelastic collisions with nitrogen molecules. *Phys. Rev. A*, 46:5696–5705, 1992.

[94] M. Ahmadi, B. X. R. Alves, C. J. Baker, W. Bertsche, E. Butler, A. Capra, C. Carruth, C. L. Cesar, M. Charlton, S. Cohen, R. Collister, S. Eriksson, A. Evans, N. Evetts, J. Fajans, T. Friesen, M. C. Fujiwara, D. R. Gill, A. Gutierrez, J. S. Hangst, W. N. Hardy, M. E. Hayden, C. A. Isaac, A. Ishida, M. A. Johnson, S. A. Jones, S. Jonsell, L. Kurchaninov, N. Madsen, M. Mathers, D. Maxwell, J. T. K. McKenna, S. Menary, J. M. Michan, T. Momose, J. J. Munich, P. Nolan, K. Olchanski, A. Olin, P. Pusa, C. Ø. Rasmussen, F. Robicheaux, R. L. Sacramento, M. Sameed, E. Sarid, D. M. Silveira, S. Stracka, G. Stutter, C. So, T. D. Tharp, J. E. Thompson, R. I. Thompson, D. P. van der Werf, and J. S. Wurtele. Observation of the 1s–2s transition in trapped antihydrogen. *Nature*, 541(7638):506–510, 2016.

[95] C. Amole, M. D. Ashkezari, M. Baquero-Ruiz, W. Bertsche, E. Butler, A. Capra, C. L. Cesar, M. Charlton, A. Deller, N. Evetts, S. Eriksson, J. Fajans, T. Friesen, M. C. Fujiwara, D. R. Gill, A. Gutierrez, J. S. Hangst, W. N. Hardy, M. E. Hayden, C. A. Isaac, S. Jonsell, L. Kurchaninov, A. Little, N. Madsen, J. T. K. McKenna, S. Menary, S. C. Napoli, K. Olchanski, A. Olin, P. Pusa, C. Ø. Rasmussen, F. Robicheaux, E. Sarid, D. M. Silveira, C. So, S. Stracka, T. Tharp, R. I. Thompson, D. P. van der Werf, and J. S. Wurtele. In situ electromagnetic field diagnostics with an electron plasma in a penning–malmberg trap. *New Journal of Physics*, 16(1):013037, 2014.

[96] D. E. Pritchard. Cooling neutral atoms in a magnetic trap for precision spectroscopy. *Phys. Rev. Lett.*, 51:1336–1339, 1983.

[97] C. J. Baker, W. Bertsche, A. Capra, C. Carruth, C. L. Cesar, M. Charlton, A. Christensen, R. Collister, A. Cridland Mathad, S. Eriksson, A. Evans, N. Evetts, J. Fajans, T. Friesen, M. C. Fujiwara, D. R. Gill, P. Grandemange, P. Granum, J. S. Hangst, W. N. Hardy, M. E. Hayden, D. Hodgkinson, E. Hunter, C. A. Isaac, M. A. Johnson, J. M. Jones, S. A. Jones, S. Jonsell, A. Khramov, P. Knapp, L. Kurchaninov, N. Madsen, D. Maxwell, J. T. K. McKenna, S. Menary, J. M. Michan, T. Momose, P. S. Mullan, J. J. Munich, K. Olchanski, A. Olin, J. Peszka, A. Powell, P. Pusa, C. Ø. Rasmussen, F. Robicheaux, R. L. Sacramento, M. Sameed, E. Sarid, D. M. Silveira, D. M. Starko, C. So, G. Stutter, T. D. Tharp, A. Thibeault, R. I. Thompson, D. P. van der Werf, and J. S. Wurtele. Laser cooling of antihydrogen atoms. *Nature*, 592(7852):35–42, 2021.

[98] A. Capra. Lifetime of magnetically trapped antihydrogen in alpha. 2020.

[99] T. W. Darling, F. Rossi, G. I. Opat, and G. F. Moorhead. The fall of charged particles under gravity: A study of experimental problems. *Rev. Mod. Phys.*, 64:237–257, 1992.

[100] F. C. Witteborn and W. M. Fairbank. Experimental comparison of the gravitational force on freely falling electrons and metallic electrons. *Phys. Rev. Lett.*, 19:1049–1052, 1967.

[101] Fairbank W. Witteborn, F. Experiments to determine the force of gravity on single electrons and positrons. *Nature*, 220:436–440, 1968.

[102] P. Dyer, J. Camp, M.H. Holzscheiter, and S. Graessle. Falling antimatter: An experiment to measure the gravitational acceleration of the antiproton. *Nuclear Instruments and Methods in Physics Research Section B: Beam Interactions with Materials and Atoms*, 40-41:485–488, 1989.

[103] R. E. Brown, J.B. Camp, and T.W. Darling. Antimatter gravity experiment. *Nuclear Instruments and Methods in Physics Research Section B: Beam Interactions with Materials and Atoms*, 56-57:480–483, 1991.

[104] T. J. Phillips. The Muonium Antimatter Gravity Experiment. *EPJ Web Conf.*, 181:01017, 2018.

[105] C. So, J. Fajans, and W. Bertsche. The alpha-g antihydrogen gravity magnet system. *IEEE Transactions on Applied Superconductivity*, 30(4):1–5, 2020.

[106] W. R. Leo. *Techniques for Nuclear and Particle Physics Experiments: A How to Approach*. 1987.

[107] J. S. Hangst. Addendum to the ALPHA Proposal; The ALPHA-g Apparatus. Technical report, CERN, Geneva, 2016.

[108] G. Smith. *Characterization and analysis development for the ALPHA-g barrel scintillator*. PhD thesis, University of British Columbia, 2021.

[109] S. Kt, A. Gupta, G. Joshi, S. Mohan, R. Pushpa, and S. Anantharmurthy. Loading detection and number estimation of an electron plasma in a penning trap. *Plasma Science and Technology*, 11:521, 2009.

[110] F.G. Major, V.N. Gheorghe, and G. Werth. *Charged Particle Traps: Physics and Techniques of Charged Particle Field Confinement*. Springer Series on Atomic, Optical, and Plasma Physics. Springer Berlin Heidelberg, 2005.

[111] J.D. Jackson. *Classical Electrodynamics*. Wiley, 2012.

[112] F. Anderegg. Rotatingwall Technique and Centrifugal Separation. In *Trapped Charged Particles: A Graduate Textbook with Problems and Solutions. Edited by R.C. Thompson et al. Published by World Scientific Publishing Co. Pte. Ltd*, pages 221–238. 2016.

[113] T. P. Friesen. *Probing Trapped Antihydrogen: In Situ Diagnostics and Observations of Quantum Transitions.* PhD thesis, 2014. Presented on 2014.

[114] G. B. Andresen et al. Evaporative Cooling of Antiprotons to Cryogenic Temperatures. *Phys. Rev. Lett.*, 105:013003, 2010.

[115] M. Ahmadi, B. X. R. Alves, C. J. Baker, W. Bertsche, A. Capra, C. Carruth, C. L. Cesar, M. Charlton, S. Cohen, R. Collister, S. Eriksson, A. Evans, N. Evetts, J. Fajans, T. Friesen, M. C. Fujiwara, D. R. Gill, J. S. Hangst, W. N. Hardy, M. E. Hayden, C. A. Isaac, M. A. Johnson, S. A. Jones, S. Jonsell, L. Kurchaninov, N. Madsen, M. Mathers, D. Maxwell, J. T. K. McKenna, S. Menary, T. Momose, J. J. Munich, K. Olchanski, A. Olin, P. Pusa, C. Ø. Rasmussen, F. Robicheaux, R. L. Sacramento, M. Sameed, E. Sarid, D. M. Silveira, C. So, G. Stutter, T. D. Tharp, J. E. Thompson, R. I. Thompson, D. P. van der Werf, and J. S. Wurtele. Enhanced control and reproducibility of non-neutral plasmas. *Phys. Rev. Lett.*, 120:025001, 2018.

[116] A. W. Hyatt, C. F. Driscoll, and J. H. Malmberg. Measurement of the anisotropic temperature relaxation rate in a pure electron plasma. *Phys. Rev. Lett.*, 59:2975–2978, 1987.

[117] G. Manfredi and P. Hervieux. Adiabatic cooling of trapped non-neutral plasmas. *Phys. Rev. Lett.*, 109:255005, 2012.

[118] W. H. Wing. On neutral particle trapping in quasistatic electromagnetic fields. *Progress in Quantum Electronics*, 8(3):181–199, 1984.

[119] H. Metcalf and P. van der Straten. Cooling and trapping of neutral atoms. *Physics Reports*, 244(4):203–286, 1994.

[120] C. Amole, M. Ashkezari, M. Baquero-Ruiz, W. Bertsche, P. Bowe, E. Butler, A. Capra, C. Cesar, M. Charlton, A. Deller, P. Donnan, S. Eriksson, J. Fajans, T. Friesen, M. Fujiwara, D. Gill, A. Gutierrez, J. Hangst, W. Hardy, and J. Wurtele. Resonant quantum transitions in trapped antihydrogen atoms. *Nature*, 483:439–43, 2012.

[121] W. Bertsche, A. Boston, P.D. Bowe, C.L. Cesar, S. Chapman, M. Charlton, M. Chartier, A. Deutsch, J. Fajans, M.C. Fujiwara, R. Funakoshi, K. Gomberoff, J.S. Hangst, R.S. Hayano, M.J. Jenkins, L.V. Jørgensen, P. Ko, N. Madsen, P. Nolan, R.D. Page, L.G.C.

Posada, A. Povilus, E. Sarid, D.M. Silveira, D.P. van der Werf, Y. Yamazaki, B. Parker, J. Escallier, and A. Ghosh. A magnetic trap for antihydrogen confinement. *Nuclear Instruments and Methods in Physics Research Section A: Accelerators, Spectrometers, Detectors and Associated Equipment*, 566(2):746–756, 2006.

[122] M. Ahmadi, B. X. R. Alves, C. J. Baker, W. Bertsche, E. Butler, A. Capra, C. Carruth, C. L. Cesar, M. Charlton, S. Cohen, R. Collister, S. Eriksson, A. Evans, N. Evetts, J. Fajans, T. Friesen, M. C. Fujiwara, D. R. Gill, A. Gutierrez, J. S. Hangst, W. N. Hardy, M. E. Hayden, C. A. Isaac, A. Ishida, M. A. Johnson, S. A. Jones, S. Jonsell, L. Kurchaninov, N. Madsen, M. Mathers, D. Maxwell, J. T. K. McKenna, S. Menary, J. M. Michan, T. Momose, J. J. Munich, P. Nolan, K. Olchanski, A. Olin, P. Pusa, C. Ø. Rasmussen, F. Robicheaux, R. L. Sacramento, M. Sameed, E. Sarid, D. M. Silveira, S. Stracka, G. Stutter, C. So, T. D. Tharp, J. E. Thompson, R. I. Thompson, D. P. van der Werf, and J. S. Wurtele. Antihydrogen accumulation for fundamental symmetry tests. *Nature Communications*, 8(1), 2017.

[123] B. M. Latacz, B. P. Arndt, B. B. Bauer, J. A. Devlin, S. R. Erlewein, M. Fleck, J. I. Jäger, M. Schiffelholz, G. Umbrazunas, E. J. Wursten, F. Abbass, P. Micke, D. Popper, M. Wiesinger, C. Will, H. Yildiz, K. Blaum, Y. Matsuda, A. Mooser, C. Ospelkaus, W. Quint, A. Soter, J. Walz, Y. Yamazaki, C. Smorra, and S. Ulmer. Base—high-precision comparisons of the fundamental properties of protons and antiprotons. *The European Physical Journal D*, 77(6), 2023.

[124] M. Knoop, N. Madsen, and R. C. Thompson. *Chapter 1: Physics with Trapped Charged Particles*, page 1–24. IMPERIAL COLLEGE PRESS, 2014.

[125] F. Pedregosa, G. Varoquaux, A. Gramfort, V. Michel, B. Thirion, O. Grisel, M. Blondel, P. Prettenhofer, R. Weiss, V. Dubourg, J. Vanderplas, A. Passos, D. Cournapeau, M. Brucher, M. Perrot, and E. Duchesnay. Scikit-learn: Machine learning in Python. *Journal of Machine Learning Research*, 12:2825–2830, 2011.

[126] S. S. Wilks. The Large-Sample Distribution of the Likelihood Ratio for Testing Composite Hypotheses. *The Annals of Mathematical Statistics*, 9(1):60 – 62, 1938.

[127] D. Hodgkinson. *On the Dynamics of Adiabatically Cooled Antihydrogen in an Octupole-Based Ioffe-Pritchard Magnetic Trap*. PhD thesis, 31 Dec 2022.

[128] C. J. Baker, W. Bertsche, A. Capra, C. L. Cesar, M. Charlton, A. Cridland Mathad, S. Eriksson, A. Evans, N. Evetts, S. Fabbri, J. Fajans, T. Friesen, M. C. Fujiwara, P. Grandemange, P. Granum, J. S. Hangst, M. E. Hayden, D. Hodgkinson, C. A. Isaac, M. A. Johnson, J. M. Jones, S. A. Jones, S. Jonsell, L. Kurchaninov, N. Madsen, D. Maxwell, J. T. K. McKenna, S. Menary, T. Momose, P. Mullan, K. Olchanski, A. Olin, J. Peszka, A. Powell, P. Pusa, C. Ø. Rasmussen, F. Robicheaux, R. L. Sacramento, M. Sameed, E. Sarid, D. M. Silveira, G. Stutter, C. So, T. D. Tharp, R. I. Thompson, D. P. van der Werf, and J. S. Wurtele. Sympathetic cooling of positrons to cryogenic temperatures for antihydrogen production. *Nature Communications*, 12(1), 2021.

[129] P. Hamilton, A. Zhmoginov, F. Robicheaux, J. Fajans, J. S. Wurtele, and H. Müller. Antimatter interferometry for gravity measurements. *Phys. Rev. Lett.*, 112:121102, 2014.

Acknowledgements

Firstly, I would like to thank my supervisor Prof. Germano Bonomi and my co-supervisor Dr. Simone Stracka for the opportunity to do my PhD and for having supervised my work.
Thanks to the ALPHA collaboration and to the ALPHA senior researchers Prof. Jeffrey Hangst and Prof. Niels Madsen for the opportunity to participate in this measurement. Moreover, I would like to thank the ALPHA detector and software team, in particular thanks to Dr. Joseph McKenna, Dr. Andrea Capra and Dr. Ina Carli.
I would also like to thank the referees of this thesis Prof. Roberto Mussa and Dr. Gervasio Gomez.
I thank all the experimental physics group of DIMI at the University of Brescia. Un ringraziamento speciale va a Ramona per tutto ciò che mi ha insegnato e per il supporto che mi ha dato.

Vorrei ringraziare la mia famiglia e in particolare i miei genitori per il loro aiuto e per l'appoggio in tutte le scelte che ho fatto.

Grazie a tutti gli amici che ho trovato a Brescia. Grazie alle mie coinquiline e amiche Lucrezia e Mariateresa che mi sono state vicine. Grazie a Lorenzo per le risate e i momenti di condivisione. Grazie a Stefano per i caffè, i confronti e le riflessioni. Grazie con affetto a Daniela che ha condiviso con me gli ultimi mesi a Brescia.
Grazie mille agli amici con cui ho passato un periodo al CERN, Chiara, Giulia e Giovanni, per la loro compagnia.
Grazie agli amici di Trieste vecchi e nuovi, Alice, Serena, Alessandro, Anna e Samuele.
Infine, un ringraziamento speciale agli amici di una vita, Chiara, Enrico, Matteo e Valentina, che riescono sempre a rendere tutto più leggero.